UNIVERSITÀ
DEGLI STUDI
FIRENZE

INTERNATIONAL DOCTORATE IN
ATOMIC AND MOLECULAR PHOTONICS

CICLO XXIX

COORDINATORE Prof. Roberto Righini

HYBRID QUANTUM STATE AND MODE ENGINEERING OF LIGHT

Settore Scientifico Disciplinare FIS/03

Dottorando
Dott. Costanzo Luca Salvatore

Tutore
Dott. Bellini Marco

Coordinatore
Prof. Righini Roberto

Anni 2013/2016

Contents

List of publications

- Luca S. Costanzo, Antonio S. Coelho, Daniele Pellegrino, Milrian. S. Mendes, Lucio Acioli, Katiuscia N. Cassemiro, Daniel Felinto, Alessandro Zavatta, Marco Bellini, "Zero-Area Single-Photon Pulses", Phys. Rev. Lett 116, 023602 (2016) - highlighted in Physics;

- Antonio S. Coelho, Luca S. Costanzo, Alessandro Zavatta, Catherine Hughes, M. S. Kim, and Marco Bellini, "Universal Continuous Variable State Orthogonalizer and Qubit Generator, Phys. Rev. Lett. 116, 110501 (2016);

- Marco Bellini, Luca S. Costanzo, Alessandro Zavatta,"Gatti di luce ibrida", Le Scienze, Settembre 2015;

- Luca S. Costanzo, Alessandro Zavatta, Samuele Grandi, Marco Bellini, Hyunseok Jeong, Minsu Kang, Seung-Woo Lee, Timothy C. Ralph "Properties of hybrid entanglement between discrete and continuous-variable states of light", Physica Scripta, Vol. 90 (2015);

- Luca S. Costanzo, Alessandro Zavatta, Samuele Grandi, Marco Bellini, Hyunseok Jeong, Minsu Kang, Seung-Woo Lee, Timothy C. Ralph "Experimental hybrid entanglement between quantum and classical states of light", Int. J. Quantum Information, Vol. 12 (2014);

- Hyunseok Jeong, Alessandro Zavatta, Minsu Kang, Seung-Woo Lee, Luca S. Costanzo, Samuele Grandi, Timothy C. Ralph, Marco Bellini Generation of hybrid entanglement of light. Nature Photonics 8, 564-569 (2014)

Introduction

Since its genesis, quantum mechanics has represented a point of discontinuity from the newtonian classical mechanics in our understanding of nature. The word discontinuity in this case refers to a generalization. A generalization about concepts previously considered antithetical, like the corpuscular or ondulatory interpretation of nature, that are now considered complementary and only apparently different. A generalization with respect to the inclusion of the measurement apparatus as an essential part of the system. In this sense, Bell's inequalities, and then Leggett's, Leggett-Garg, Kochen-Specker and so on, have just formalized with mathematical arguments the several aspects of discontinuity between quantum and classical mechanics.

However, together with answers to old questions, quantum mechanics came up with new peculiar problems too. For instance, it was and still is theoretically not clear how the interaction with the measurement apparatus can unitarily evolve just towards the observed outcome. In other words, why is it necessary an ad hoc rule, Born's rule, to provide an apparently arbitrary non-deterministic character to an otherwise deterministic evolution? Looking at their potential in the development of new technology, in some cases quantum features constitute essential tools to exceed the capabilities of classical computation or communication, in some others they represent an impediment to realize operations easily implemented by classical systems, like cloning or negating units of information. The possible application of the so-called quantum revolution in technology is indeed a highly debated point, that's why basic research in the field of quantum mechanics is still necessary today.

One of the most fertile techniques of investigation, in the quantum framework, is constituted by the so-called quantum state and mode engineering.

Following the words of Rainer Blatt, Gerard J Milburn and Alex Lvovsky in the editorial of Journal of Physics B to celebrate the 20th anniversary of quantum state engineering [1], *quantum state engineering* is "a field that studies techniques of preparation, manipulation and characterization of arbitrary quantum states within a Hilbert space associated with a particular physical system".

The definition is so clear that it gives us the general recipe for every quantum state engineering experiment.

First we need to prepare an initial state. It can be the light emitted from a laser, an atomic gas, the physical vacuum or any other system. It's fundamental to select this state very carefully, firstly because it defines the physical domain of the research, secondly because it must be useful and appropriate to enlighten the physics we are interested in.

The second step is the manipulation. Once the initial state has been selected, it can be transformed by means of whatever operation can be useful for the purpose.

The last point is the detection. Indeed, in this experimental approach the interesting physical information is encoded in the manipulated quantum state, that's why an efficient diagnostic tool to retrieve it is necessary . For example, a faithful implementation of a quantum operation can be proven by observing the way it transforms a given input state [2], the experimental realization of a protocol by measuring how much a given quantity, function of the state, is affected by the manipulation [3],[4], and so on ([5]). Even if these experiments look different, they share this three-step approach: the preparation of an initial state, its manipulation and information retrieval by means of detection. In the second part of this thesis two state-engineering-based experiments will be presented. One of them realizes an universal orthogonalizer for arbitrary quantum states of light and might constitute the basis for generalizing the concept of the qubit to the continuous variable regime. The other experiment uses coherent superpositions of basic quantum operations to emulate a strong Kerr nonlinearity at the few-photon level, and could be used to implement new logic gates for quantum computation.

In some sense, complementary to the state engineering is the *mode engineering technique*. Indeed, while in state engineering the purpose is the detection of an unknown state after its manipulation, in mode engineering experiments the perspective is completely reversed: the final state is assumed to be known and what has to be inferred are its spatio-temporal features, that is its mode. Of course, this type of technique requires the use of a mode sensitive detector, and we will see that in this sense homodyne detection represents a perfect candidate. The third part of this thesis will be then dedicated to a mode-engineering-based experiment, where the interaction of broadband single photons with resonant atomic vapours will be proven just by detecting the reshaping of the light temporal mode produced by the radiation-matter coupling. The manipulation of the spatiotemporal mode of a single photon is a promising new way for encoding quantum information by using a large alphabet of possible shapes instead of the usual qubit scheme based on two orthogonal linear polarizations. Moreover, by showing the possibility of strong transient interaction between ultrashort single photons and resonant atomic media, this experiment may open the way to alternative schemes of quantum memories, with applications to quantum communications and computing.

I directly contributed to all the experiments presented in detail in the second and third parts of this thesis. Two different but similar experimental setups were used, based on two pulsed laser sources of different duration. My personal contribution ranged from the modelling and simulation of the experiments to their actual realization and in the final analysis of the measured data.

Part I

Quantum optics: an introduction

In the first part of this thesis, important concepts of quantum optics are presented to familiarize with the notation used.
The first chapter represents an overview of the main quantum states and observables used in the following chapters.
The second chapter is instead dedicated to balanced homodyne detection, the main state characterization technique adopted in the experiments presented in this work of thesis.

Chapter 1

Brief introduction to quantum optics

This chapter represents a very small guide to quantum optics. The aim is mainly to give an introduction to the notation used in the following chapters. The first part is an introduction to the various formalisms used to describe a quantum state.
In the second, we see an overview of the principal quantum pure states of light. Basically, we start by classifying the different states on the basis of the different photon number statistics they show in a measurement. Here we don't consider the spatio-temporal proprieties of states and operators, i.e. their mode.
In the final part we rewrite the previously defined states and operators by taking into account their mode, in a mode-distributed analysis. We finish by demonstrating that all the results shown in the second part, can be recovered by limiting the mode distributed formalism to a single mode, independently of its shape.

1.1 Representation of a quantum state

Quantum formalism is generally developed by making use of vectors [25], indicated as $|\Psi\rangle$ living in an Hilbert space. Without entering into the meaning to assign to these vectors (see [73] for example), we can safely assert that these vectors contain the amount of information necessary for a complete description of a given system.

When we deal with statistical ensembles a density operator based description is instead necessary [62],[63]. The density operator ρ is generally defined as $\sum_i P_i|\Psi_i\rangle\langle\Psi_i|$ and it is then represented by a matrix in a particular basis. Finally, especially to present the experimental results, we make use of a different formalism based on a *quasiprobability distribution* and in particular the so-called *Wigner function*

$$W\left(q,p\right)=\frac{2}{\pi}\int_{-\infty}^{+\infty}\langle q+x|\rho|q-x\rangle e^{i4px}\ dx. \tag{1.1}$$

The Wigner function description is especially useful when we deal with quantum systems, as their nonclassicality is often immediately evident from the negativity of the function itself [62].

1.2 Overview of the main quantum pure states of light

Fock state The Fock states, or number states $|n\rangle$, represent the eigenvectors of the *photon number operator* $\hat{n}$ or, equivalently, the discrete degree of excitation (the number of quanta) of the electromagnetic free-field Hamiltonian [62],[63]

$$\hat{H}_{free}=\hbar\omega\left(\hat{n}+\frac{1}{2}\right). \tag{1.2}$$

at the frequency $\omega/2\pi$, where this frequency defines a monochromatic field mode.
It can be proven that the observable $\hat{n}$ can be written as

$$\hat{n}=\hat{a}^{\dagger}\,\hat{a} \tag{1.3}$$

where $\hat{a}^{\dagger}$ and $\hat{a}$ define respectively the single photon creation and annihilation operators, operating on the number states as

$$\begin{aligned}\hat{a}^{\dagger}\,|n\rangle &= \sqrt{n+1}\,|n+1\rangle\\ \hat{a}\,|n\rangle &= \sqrt{n}\,|n-1\rangle\\ \hat{a}\,|0\rangle &= 0\end{aligned} \tag{1.4}$$

and are subjected to the commutation relation rule

$$\left[\hat{a}, \hat{a}^{\dagger}\right] = 1. \tag{1.5}$$

Number states are an orthonormal set

$$\langle n|m\rangle = \delta_{n,m}. \tag{1.6}$$

During this thesis we will encounter a Fock state in particular: the single photon state $|1\rangle$.
Fock states possess a fully non classical character testified by a negative Wigner function and any attempt to describe them with an effective noise theory leads to negative probabilities.

Coherent state Coherent states of light $|\alpha\rangle$ [62],[63] can be defined as the eigenstates of the single photon annihilation operator $\hat{a}$ [3]

$$\hat{a}\,|\alpha\rangle = \alpha\,|\alpha\rangle. \tag{1.7}$$

Equivalently we can express a coherent state by using its decomposition on the Fock basis as

$$|\alpha\rangle = e^{-\frac{|\alpha|}{2}} \sum_{n} \frac{\alpha}{\sqrt{n!}}\,|n\rangle. \tag{1.8}$$

In general they are not orthogonal to each other, especially when dealing with small amplitudes, as

$$\langle\beta|\alpha\rangle = e^{-\frac{|\alpha-\beta|^2}{2}} \tag{1.9}$$

where $|\alpha\rangle, |\beta\rangle$ are two different coherent states of light.
Sometimes during this thesis, we will make use of the so-called unitary displacement operator $\hat{D}(\alpha)$, which alternatively defines coherent states as displaced vacuum states

$$\begin{aligned} |\alpha\rangle &= \hat{D}(\alpha)\,|0\rangle \\ &= e^{\alpha\,\hat{a}^{\dagger}-\alpha^{*}\,\hat{a}}\,|0\rangle \end{aligned} \tag{1.10}$$

In quantum optics, coherent states are considered the most classical of all pure states as, in many situations, they can be treated semiclassically, that is, as a classical light field with the addition of stochastic noise.

1.3 Brief overview of observables

Electric field quadrature A fundamental observable in quantum optics is the electric field quadrature, defined as

$$\hat{X}(\theta) = \frac{\hat{a}^{\dagger}e^{i\theta} + \hat{a}e^{-i\theta}}{2} \tag{1.11}$$

where θ defines the phase of the measurement. Sometimes the quadrature $\hat{X}(\theta = 0)$ is called $\hat{X}$ quadrature, whereas the quadrature $\hat{X}(\theta = \pi/2)$ is called $\hat{Y}$.
We will see in Chapter 2 that the electric field quadrature can be measured by means of balanced homodyne detection.

On-off single photon detection Number operator $\hat{n}$ has been already introduced as a measure of the number of particles. Actually this kind of measurement requires complicated photon number resolving detectors not easily accessible in the lab. What is more commonly used is a single photon counting module (SPCM) represented for instance by an avalanche photodiode (APD), a device capable to detect with a given quantum efficiency η the presence or the absence of photons but not to discern their exact number. In other words, the detector will produce the same positive response, a *click*, in the occurrence of photons, independently on their exact number, that's why we speak of *on-off detector*.
Mathematically, the *click* of an on-off detector erases the vacuum contribution from the state and can thus be described by

$$\hat{\Pi}_{APD} = \hat{I} - |0\rangle\langle 0|. \tag{1.12}$$

where $\hat{I}$ is the identity operator.

1.4 Distributed mode formalism

The single monochromatic mode operators $\hat{a}, \hat{a}^{\dagger}$ are ideal operations only approximately achievable in experiments. Indeed, in all real scenarios a distributed mode analysis should be considered, with every state and operator being distributed on a finite wavepacket $g(\omega)$[1].

---

[1] We ignore any other dependence, like the spatial one, for sake of simplicity.

For instance we can define the single photon creation operator acting on a wavepacket $g(\omega)$ as

$$\hat{a}_g^\dagger = \int d\omega\, g(\omega)\, \hat{a}^\dagger(\omega), \tag{1.13}$$

and its hermitian, the single photon annihilation operator acting on the same wavepacket $g(\omega)$ as

$$\hat{a}_g = \int d\omega\, g^*(\omega)\, \hat{a}(\omega), \tag{1.14}$$

with the meaning of respectively adding and subtracting a photon in a mode specified by $g(\omega)$. The spectrum is normalized to 1 as

$$\int d\omega\, |g(\omega)|^2 = 1. \tag{1.15}$$

In the same way, we can define also the equivalent of the displacement (1.10) as

$$\hat{D}(\{\alpha\}) = e^{\hat{a}_\alpha^\dagger - \hat{a}_\alpha} \tag{1.16}$$

where the notation $\hat{D}(\{\alpha\})$ is used to differentiate it from the previous case of eq.(1.10). The mode $\alpha(\omega)$ is now normalized to the mean photon number of the displacement, i.e.

$$\int d\omega\, |\alpha(\omega)|^2 = \langle\hat{n}\rangle. \tag{1.17}$$

According to these new definitions, the states produced by applying these operators are distributed on the corresponding modes too, as

$$\begin{aligned} |1_g\rangle &= \hat{a}_g^\dagger\, |0\rangle \\ &= \int d\omega\, g(\omega)\, \hat{a}^\dagger(\omega)\, |0\rangle \\ &= \int d\omega\, g(\omega)\, |1_\omega\rangle \end{aligned} \tag{1.18}$$

To avoid confusion with the notation, we indicate $|1_g\rangle$ a photon distributed on a finite wavepacket $g(\omega)$, and $|1_\omega\rangle$ a monochromatic photon at the frequency

ω, that is a photon produced by the monochromatic or delta shaped mode distributed operator $\hat{a}^\dagger(\omega) = \int d\omega' \delta(\omega' - \omega)\hat{a}^\dagger(\omega')$.

The eigenrelation (1.7) takes now the form

$$\hat{a}(\omega) \, |\{\alpha\}\rangle = \alpha(\omega) \, |\{\alpha\}\rangle, \tag{1.19}$$

where again the notation $|\{\alpha\}\rangle$ is used to differentiate the mode distributed state from the monochromatic one of Eq.(1.7).

This more general formalism has strong consequences when trying to handle operators and states distributed on different modes. Consider for example the projection of a single photon in a mode $g(\omega)$ on another single photon state with a different wavepacket $f(\omega)$

$$\begin{aligned}
\langle 1_f | 1_g \rangle &= \int d\omega \, \langle 0 \, |\hat{a}(\omega) \, f^*(\omega) \int d\omega' \, g(\omega')\hat{a}^\dagger(\omega') \, |0\rangle \\
&= \int d\omega \, \langle 1_\omega \mid f^*(\omega) \int d\omega' \, g(\omega') \, |1_{\omega'}\rangle \\
&= \int d\omega \, f^*(\omega) \int d\omega' \, g(\omega') \, \langle 1_\omega | 1_{\omega'} \rangle \\
&= \int d\omega \, f^*(\omega) \int d\omega' \, g(\omega') \, \delta_{\omega,\omega'} \\
&= \int d\omega \, f^*(\omega) g(\omega). \qquad (1.20)
\end{aligned}$$

The result (1.20) depends strongly on the two mode overlap and contrarily to the delta shaped mode formalism of the previous section (see Eq.(1.4)), it can be also 0 despite the equivalence of the two states. Equation(1.20) also shows that a precise manipulation of a quantum system requires a complete experimental control of its spatio-temporal characteristics. This is not easy at all when dealing with single photons because of the extremely low intensities. For instance, common methods of spectro-temporal characterization, like Frequency-resolved optical gating (FROG), cannot be used in this regime.

To simplify the formalism, we restrict the manipulation of operators and states to a single, non monochromatic mode. Indeed, all the ordinary properties seen in the previous section, like the Fock state orthonormality, can be retrieved when dealing with single distributed-mode objects.

All along this thesis, we will always consider valid the single mode approximation except when explicitly stated differently.

A more complete discussion about non monochromatic modes can be found in the book [63] where the adjective *continuous* is used to indicate what is called *distributed*, in referring to the modes, in this thesis. This choice is done to avoid confusion, as the adjective *continuous* is here mainly used to refer to the *continuous* variable (CV) description presented further.

1.5 Discrete and continuous variables

As in classical information processing with digital or analog encoding, also in quantum systems the discrete or continuous degrees of freedom divide the states, the operators and the detection schemes considered above into two large groups: if an element is mathematically characterized by an observable degree of freedom with discrete spectrum we say that it is a discrete-variable system (DV), otherwise, when it is described by a continuous spectrum, we talk about continuous variable (CV). Examples of discrete-variable elements are Fock states $|n\rangle$ and the single-photon-creation operator $\hat{a}^\dagger$, while for typical continuous variable we can include states with gaussian probability distributions like coherent states $|\alpha\rangle$ [2].

Even if this formal distinction apparently looks redundant, DV and CV worlds do not share generation and manipulation schemes nor quantum-information-processing (QIP) protocols. For instance, while a single-photon detector like an avalanche photodiode (APD) can be used to easily perform a complete tomography of a DV described single photon, it is not sufficient to characterize a CV coherent state. In this case, a more challenging continuous-variable measurement like balanced homodyne detection must be considered. In general, current optical technology enables an on-demand production and a simple manipulation of CV states with the use of lasers, nonlinear crystals, beam splitters and homodyne detectors.

However, CV ingredients alone are not sufficient, because several QIP protocols require the use of non-gaussianities typical of the DV framework as a fundamental ingredient. The implementation of DV operations is generally more challenging and tipically it requires the coupling to a discrete level system. It has recently been proposed to follow another approach, that is, to exploit nonlinearities induced by the measurement [8]. The new approach

---

[2] The distinction between discrete and continuous variable systems doesn't concern the mode. The creation operator $\hat{a}^\dagger_\xi$ has still a discrete-variable description even if the single-photon wavepacket $\xi(t)$ is a continuous function of the time t.

is probabilistic, since measurement itself is intrinsically a probabilistic process, but the use of ancillary single photons together with optical interference can push the success probability of these measurement-based nonlinear gates close to unity [9].
Currently, there is a strong tendency towards combining DV and CV elements in order to build an hybrid QIP technology with protocols and schemes designed to take advantage of both the worlds [6]. Examples are the implementation of a DV operation such as single photon creation on a CV coherent state ([7]), or the characterization of a DV single photon state with a CV tomographical technique such as balanced homodyne detection [10].

Chapter 2

Balanced homodyne detection

In this chapter we give a brief picture of the balanced homodyne detection system used in the characterization of states of light. For the mathematical details see Appendix A.

2.1 Homodyne operator

A balanced homodyne detector is a detection system allowing the observation of the electric field quadrature $\hat{X}(\theta)$ (see Eq.(1.11)) corresponding to any phase component of an optical signal. The measurement is enabled by the interference of an unknown state of light with an intense coherent state called *local oscillator* by means of a balanced beam splitter. Then the intensities from the two output arms of the beam splitter are measured with proportional photodiodes and the two photocurrents amplified and subtracted. The electrical signal produced is then proportional to the quadrature of the electric field of the unknown state (see Fig.2.1).

To calculate the explicit form of the operator it is useful to remind the input/output relations for a 50% beam splitter[1]

$$\begin{pmatrix} \hat{a}'_1 \\ \\ \hat{a}'_2 \end{pmatrix} = \begin{pmatrix} \frac{1}{\sqrt{2}} & i\frac{1}{\sqrt{2}} \\ \\ i\frac{1}{\sqrt{2}} & \frac{1}{\sqrt{2}} \end{pmatrix} \begin{pmatrix} \hat{a}_1 \\ \\ \hat{a}_2 \end{pmatrix} \tag{2.1}$$

---

[1] In writing such a beam splitter matrix, we are implicitly ignoring any effective dispersion within the beam splitter material.

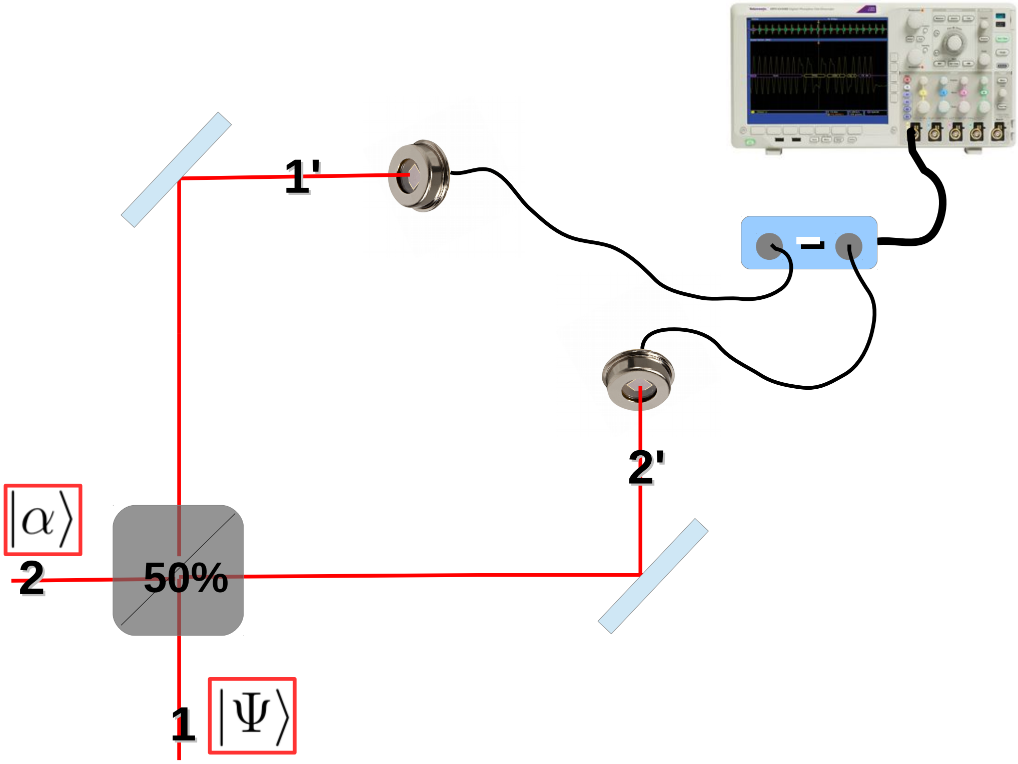

Figure 2.1: In a balanced homodyne detector the electric field quadrature of a target state is proportional to the difference of the two photocurrents produced by detecting the intensities at the two output arms $1', 2'$ of a 50% beam splitter. A strong beam with poissonian photon number distribution, that is a coherent state $|\alpha\rangle$ called *local oscillator (LO)*, and an unknown state are injected into the two input arms $2, 1$.

where $\hat{a}_{1,2}$ and $\hat{a}'_{1,2}$ correspond to the annihilation operators of two input and output modes, respectively. Given the intensities $\hat{I}_{1'}, \hat{I}_{2'}$ measured at the two output modes of the 50% beam splitter, the operator corresponding to the definition of the homodyne measurement is[2]

$$\begin{aligned}\hat{\mathcal{H}} &= \langle \alpha_{LO_2} | \hat{I}_{1'} - \hat{I}_{2'} | \alpha_{LO_2} \rangle \\ &= \hat{a}^\dagger_\alpha + \hat{a}_\alpha \\ &= 2\sqrt{n_{LO}}\,\hat{X}_{\tilde{\alpha}}(0)\,, \end{aligned} \tag{2.2}$$

where it has been used the distributed mode generalization of the quadrature operator (1.11), defined as

$$\begin{aligned}\hat{X}_\alpha &= \frac{\hat{a}^\dagger_\alpha + \hat{a}_\alpha}{2} \\ &= \sqrt{n_{LO}}\,\frac{\hat{a}^\dagger_{\tilde{\alpha}} + \hat{a}_{\tilde{\alpha}}}{2} \\ &= \sqrt{n_{LO}}\,\hat{X}_{\tilde{\alpha}} \end{aligned} \tag{2.3}$$

and with the modes $\alpha(t)$ and $\tilde{\alpha}(t)$ respectively normalized according to the eqs.(1.17) and (1.15), that is $\alpha(t) = \sqrt{n_{LO}}\tilde{\alpha}(t)$ where n_{LO} is the mean photon number of the local oscillator beam.
We can conclude that balanced homodyne detection enables the measurement of the electric field quadrature (1.11) of the state injected in the beam splitter on a mode α defined by the local oscillator.
Eq.(2.2) can be easily generalized to the detection of quadratures corresponding to any value of phase by simply shifting the LO phase as $\alpha_{LO} \rightarrow \alpha_{LO}e^{i\theta}$. Indeed

$$\hat{\mathcal{H}}(\theta, \alpha) = 2\sqrt{n_{LO}}\,\hat{X}_{\tilde{\alpha}}(\theta). \tag{2.4}$$

2.2 Losses

A first important correction can be easily introduced into the ideal observable (2.4) by considering real photodetectors. Indeed, in an ideal photodiode,

---

[2] See eq.(A.1) in Appendix A for the mathematical details.

some current is produced proportionally to the number of photons impinging on it. Since in real scenarios not all photons can interact into the detector, the operational parameter *quantum detection efficiency* η_{ph} is generally introduced in order to take into account only the fraction of absorbed photons. This inefficiency can be modeled by considering the presence of two identical beam splitters with transmittivity η_{ph} in front of each one of the two homodyne photodiodes [63], [65].

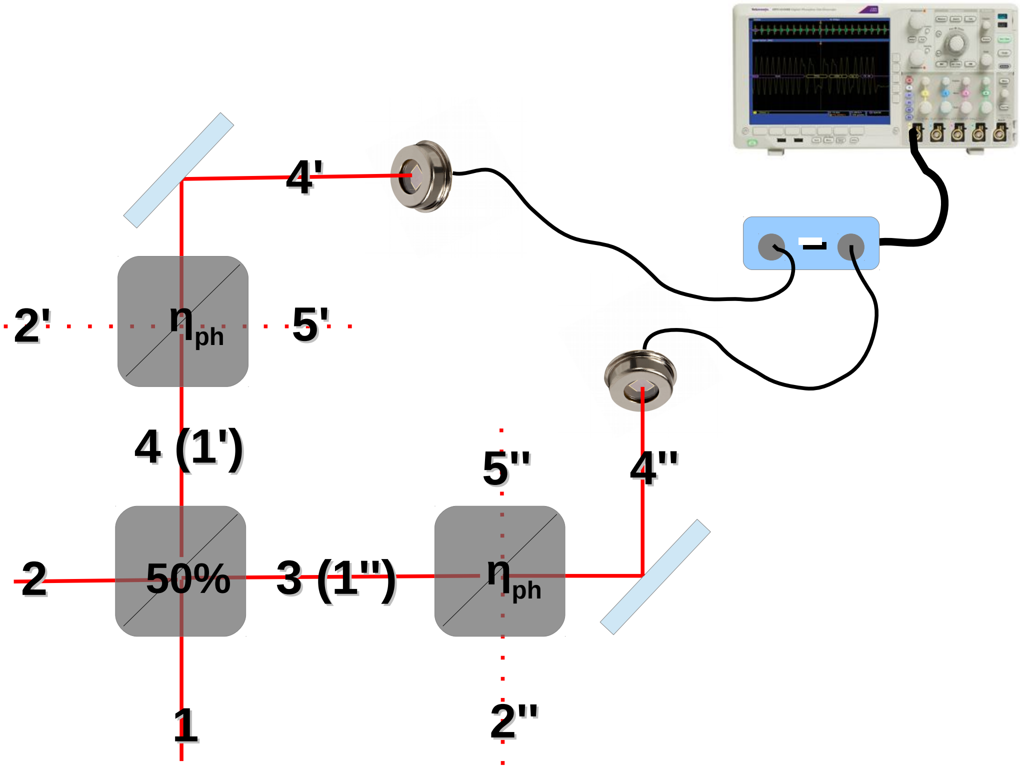

Figure 2.2: Due to the probabilistic nature of the photoelectric interaction, only the fraction η_{ph} of photons is absorbed into the detector. This situation can be represented by introducing a beam splitter with transmittivity η_{ph} along the optical path, before the ideal detection. Then, before impinging into the photodiodes, a fraction of photons is lost with probability $1 - \eta_{ph}$. In the figure the two output modes $3, 4$ of the balanced homodyne 50% beam splitter are the two input mode $1', 1''$ of the loss beam splitters.

The operators $\hat{a}_1', \hat{a}_2'$ $(\hat{a}_1'', \hat{a}_2'')$ are then affected by the loss beam splitters (see Fig.2.2) as

$$\begin{pmatrix} \hat{a}_{4'} \\ \\ \hat{a}_{5'} \end{pmatrix} = \begin{pmatrix} \sqrt{\eta_{ph}} & i\sqrt{1-\eta_{ph}} \\ \\ i\sqrt{1-\eta_{ph}} & \sqrt{\eta_{ph}} \end{pmatrix} \begin{pmatrix} \hat{a}_{1'} \\ \\ \hat{a}_{2'} \end{pmatrix} \tag{2.5}$$

We can now calculate the non ideal homodyne operator as[3]

$$\begin{aligned} \hat{\mathcal{H}}(\theta, \alpha, \eta_{ph}) &= \langle \alpha_{LO_2}, 0_{2'}, 0_{2''} | \hat{I}_{4'} - \hat{I}_{4''} | \alpha_{LO_2}, 0_{2'}, 0_{2''} \rangle \\ &= \eta_{ph} \cdot \hat{\mathcal{H}}(\theta, \alpha) \end{aligned} \tag{2.6}$$

2.3 Effect of non-identical photodiodes

Equation (2.6) can be easily generalized to take into account the effect of photodiodes with different quantum efficiency η_{ph}. Indeed, calling $\eta_{ph4'}$ and $\eta_{ph4''}$ the quantum efficiency of the two photodiodes respectively placed on the arms $4'$ and $4''$ (see Fig.2.2), the expectation value of the homodyne operator takes the form

$$\begin{aligned} \hat{\mathcal{H}}(\theta, \alpha, \eta_{ph4'}, \eta_{ph4''}) &= \langle \alpha_{LO_2}, 0_{2'}, 0_{2''} | \hat{I}_{4'} - \hat{I}_{4''} | \alpha_{LO_2}, 0_{2'}, 0_{2''} \rangle \\ &= \langle \alpha_{LO_2}, 0_{2'}, 0_{2''} | \eta_{ph4'}\, \hat{a}^{\dagger}_{4'}\, \hat{a}_{4'} - \eta_{ph4''}\, \hat{a}^{\dagger}_{4''}\, \hat{a}_{4''} | \alpha_{LO_2}, 0_{2'}, 0_{2''} \rangle \\ &= \left(\frac{\eta_{ph4'} + \eta_{ph4''}}{2} \right) 2\sqrt{n_{LO}}\, \hat{X}_{\tilde{\alpha}}(\theta) + \left(\frac{\eta_{ph4'} - \eta_{ph4''}}{2} \right) (n_{LO} + \hat{n}_1) \\ &\approx \left(\frac{\eta_{ph4'} + \eta_{ph4''}}{2} \right) 2\sqrt{n_{LO}}\, \hat{X}_{\tilde{\alpha}}(\theta) + \left(\frac{\eta_{ph4'} - \eta_{ph4''}}{2} \right) n_{LO} \end{aligned} \tag{2.7}$$

where again n_{LO} is the mean photon number of the local oscillator and $\hat{n}_1$ is the photon number operator of the state injected on the input mode 1. The last approximation is due to the common choice of a local oscillator beam much more intense of the state injected on mode 1, that is $\langle \hat{n}_1 \rangle \ll n_{LO}$. Equation (2.7) tells us that the expectation value of the homodyne measurement is affected by any possible unbalancing in the quantum efficiency of the two photodiodes with a constant offset fixed by the local oscillator intensity. The effect can be anyway compensated by measuring this constant offset as given by the vacuum state mean quandrature.

---

[3] See eq. (A.2) in Appendix A.

2.4 Mode matching

Quantum detection inefficiency doesn't represent the only reason for a non perfect detection. Indeed another cause of degradation in homodyne measurement is given by non perfect mode matching of the local oscillator to the state that we want to measure. To see this, let's calculate the variance of the observable on a generical target state $|\Psi\rangle$[4]

$$\begin{aligned}\left(\Delta\hat{\mathcal{H}}(\eta_{ph})\right)^2 &= \langle\Psi_1,\alpha_{LO_2},0_{2'},0_{2''}|\left[\hat{I}_{4'}-\hat{I}_{4''}\right]^2|\Psi_1,\alpha_{LO_2},0_{2'},0_{2''}\rangle - \\ &- \langle\Psi_1,\alpha_{LO_2},0_{2'},0_{2''}|\hat{I}_{4'}-\hat{I}_{4''}|\Psi_1,\alpha_{LO_2},0_{2'},0_{2''}\rangle^2 \\ &= \eta_{ph}^2\left\{\langle\left[\hat{a}_\alpha^\dagger+\hat{a}_\alpha\right]^2\rangle - \langle\ \left[\hat{a}_\alpha^\dagger+\hat{a}_\alpha\right]\ \rangle^2\right\} \\ &+ \eta_{ph}(1-\eta_{ph})\int_T dt\,\langle\left[\hat{a}_1^\dagger(t)\hat{a}_1(t)+|\alpha(t)|^2\right]\rangle \\ &= 4\eta_{ph}^2\left(\Delta\hat{X}_\alpha(\theta)\right)^2+\eta_{ph}(1-\eta_{ph})\left(\int_T dt\,\langle\,\hat{n}_1(t)\rangle+n_{LO}\right),\end{aligned} \tag{2.8}$$

where the first term comes directly from the variance of the electric field, whereas the second one has its origin in the intensity fluctuations due to the non perfect detection efficiency of the two identical photodiodes. To see how the matching to the local oscillator mode affects the variance (2.8), let's calculate it on a single photon state with a wavepacket $\beta(t)$[5,6]

$$\begin{aligned} &= \eta_{ph}^2\left\{\langle 1_\beta|\left[\hat{a}_\alpha^\dagger+\hat{a}_\alpha\right]^2|1_\beta\rangle - \langle 1_\beta|\left[\hat{a}_\alpha^\dagger+\hat{a}_\alpha\right]|1_\beta\rangle^2\right\} \\ &+ \eta_{ph}(1-\eta_{ph})\left(\int_T dt\,\langle 1_\beta|\,\hat{n}_1(t)\,|1_\beta\rangle+n_{LO}\right) \\ &= 2\eta_{ph}^2\left|\int dt\,\beta^*(t)\,\alpha(t)\right|^2+\eta_{ph}^2\,n_{LO}+\eta_{ph}(1-\eta_{ph})\ (1+n_{LO})\end{aligned} \tag{2.9}$$

---

[4] See eq.(A.3) in Appendix A

[5] See eq.(A.4) in Appendix A.

[6] All along this thesis we will use the same symbol to indicate the shape of a mode in the temporal or in the spectral domain, then for instance we will use indifferently the notation $\beta(\omega)$ and $\beta(t)$. Thus all the calculations done over time could have equivalently been done over the frequencies just by properly changing the variable and the integration domain.

To understand the importance of the mode matching contribution to the variance, in eq.(2.9) it can be helpful to use again a LO mode normalized to 1, i.e. $\alpha(t) = \sqrt{n_{LO}}\tilde{\alpha}(t)$

$$\begin{aligned}
& 2\eta_{ph}^2 \left| \int dt\, \beta^*(t)\, \alpha(t) \right|^2 + \eta_{ph}^2\, n_{LO} + \eta_{ph}(1-\eta_{ph})\ (1+n_{LO}) \\
= \;& 2\eta_{ph}^2\, n_{LO} \left| \int dt\, \beta^*(t)\, \tilde{\alpha}(t) \right|^2 + \eta_{ph}^2\, n_{LO} + \eta_{ph}(1-\eta_{ph})\ (1+n_{LO})\,. \\
\approx \;& 2\eta_{ph}^2\, n_{LO} \left| \int dt\, \beta^*(t)\, \tilde{\alpha}(t) \right|^2 + \eta_{ph}^2\, n_{LO} + \eta_{ph}(1-\eta_{ph})\, n_{LO} \\
= \;& 2\eta_{ph}^2\, n_{LO} \left| \int dt\, \beta^*(t)\, \tilde{\alpha}(t) \right|^2 + \eta_{ph}\, n_{LO} \qquad (2.10)
\end{aligned}$$

where it has been used the fact that the local oscillator beam is generally a very intense beam with a very high mean photon number. Eq.(2.10) presents clearly how the variance depends on the square of the complex modulus of the overlap between the signal and local oscillator modes. We call this important quantity *mode matching efficiency* η_{mm}

$$\eta_{mm} = \left| \int dt\, \beta^*(t)\, \tilde{\alpha}(t) \right|^2 \qquad (2.11)$$

The worst case of single photon completely unmatched to the LO, that is $\eta_{mm} = 0$, provides the variance of the vacuum or the *shot noise* level of the detector

$$\left(\Delta\hat{\mathcal{H}}\right)^2_{shot} \;=\; \eta_{ph}\, n_{LO} \qquad (2.12)$$

i.e. the variance in absence of any signal. Eq.(2.12) shows a fundamental physical significance, that is, the shot noise level can be amplified by the local oscillator intensity. In other words, the response of the detector to the lowest significant signal can be boosted up to overcome the electronic noise by only increasing the optical power of the local oscillator. This feature is at the basis of the extraordinary sensitivity of homodyne detection and enables single-photon-level measurements, hardly achievable with other detectors.

The shot noise level increases linearly with the LO intensity.
The quadrature variance ratio of a single photon in the mode β respect to the vacuum, eq.(2.10), can now be calculated as

$$\begin{aligned}\frac{\left(\Delta\hat{\mathcal{H}}\right)^2_{photon}}{\left(\Delta\hat{\mathcal{H}}\right)^2_{shot}} &= \frac{2\,\eta_{ph}^2\,n_{LO}\,\eta_{mm}+\eta_{ph}\,n_{LO}}{\eta_{ph}\,n_{LO}} \\ &= 2\,\eta_{ph}\,\eta_{mm}+1 \qquad (2.13)\end{aligned}$$

three times above the shot noise level in the ideal case of perfect mode matching ($\eta_{mm}=1$) and ideal photodetectors ($\eta_{ph}=1$).

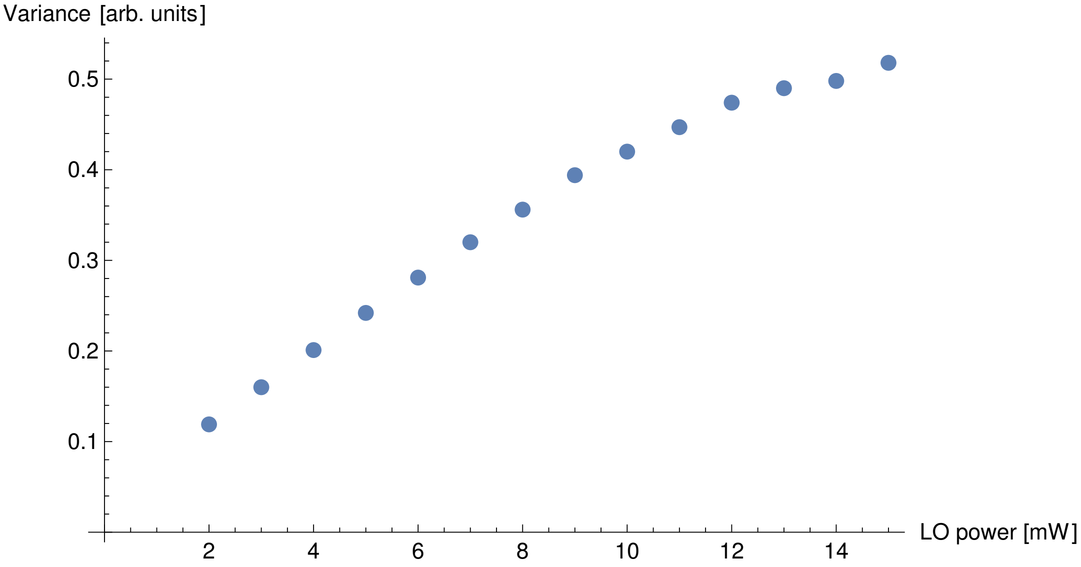

Figure 2.3: Vacuum state variance vs. local oscillator power n_{LO} as measured with the balanced homodyne detector. Saturation and unbalancing of the photodiodes at high LO power is the cause of the distorsion from the linear trend predicted by Eq.(2.10).

2.5 Detection efficiency

The two factors η_{ph} and η_{mm}, even if physically unrelated, have the same effect of degradation on the measurement. We can operatively summarize the joint action of all the detection losses, by introducing the *total detection efficiency* coefficient η_{det} as the product of all the different contributions

$$\eta_{det} = \eta_{ph} \cdot \eta_{mm} \cdot \eta_{el} \cdot \eta_{op}, \tag{2.14}$$

where we considered, in addition to the photodiode quantum efficiency η_{ph} and to the mode matching efficiency η_{mm}, the contribution of the *detector electronic noise* η_{el}, due to non-ideal-electronic signal amplification,subtraction,etc. and the *optical losses* η_{op}, given by the unavoidable optical losses caused by non ideal optical elements (mirrors, lenses, etc.).

Part II

Quantum state manipulation

This part is dedicated to the experimental methods developed in our laboratory to manipulate the statistical properties of quantum states of light at the single photon level.
Firstly, we analyze how fundamental quantum operations like the single particle creation $\hat{a}^\dagger$ and the single particle annihilation $\hat{a}$ can be experimentally implemented in the optical domain.
In the second part two experiments, an *Universal Continuous-Variable State Orthogonalizer and Qubit Generator* and a *Measurement-induced strong Kerr nonlinearity for weak quantum states of light* are presented as applications of the concepts and experimental methods developed.

Chapter 3

Experimental single-photon arithmetics

State manipulation often requires to play with quantum systems at a single particle level. With this perspective, several experimental techniques have been developed to handle and fully control the dynamics of photons, atoms, ions, etc. Among all these operations, the full spirit of quantum mechanics is probably best represented by two in particular, as the most fundamental basic quantum transformations: the single quantum addition $\hat{a}^\dagger$ and the single quantum subtraction $\hat{a}$.
Contrarily to the theoretical conceptual simplicity, the experimental implementation of $\hat{a}^\dagger$ and $\hat{a}$ requires nontrivial efforts. Several techniques have been proposed and tested in this direction, but only two of them have been extensively used to successfully manipulate quantum states of light. These two methods share the same probabilistic approach, based on the detection of a single photon in an ancillary mode 2, to conditionally implement single photon creation and annihilation operators on a mode 1.

We can thus figure this technique like the effect of a machine with two input and two output channels: the first one is the signal channel, designed to hold the target state before and after the manipulation, the second one instead announces when the desired transformation has successfully occurred. Formally, this means that we are looking for two unitary operators with the form

$$\hat{U} = e^{i\theta \hat{J}(\hat{a}_1, \hat{a}_2, \hat{a}_1^\dagger, \hat{a}_2^\dagger)}, \tag{3.1}$$

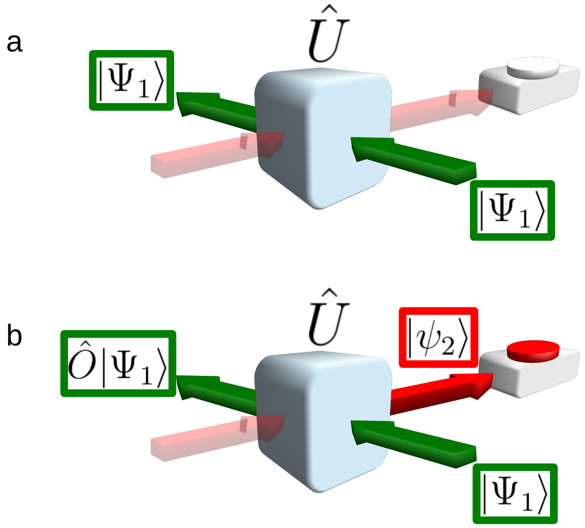

Figure 3.1: In a conditioned manipulation machine $\hat{U}$ with two input and two output channels $1, 2$ a given transformation $\hat{O}$ is experimentally implemented in a probabilistic process on a target state $|\Psi_1\rangle$ by a proper physical system. At the first input/output channel we have the target state $|\Psi_1\rangle$ before/after the probabilistic transformation. Note that this transformation will be operated by the machine nondeterministically with a small success probability on mode 1. In the second channel (ancilla) we inject nothing (vacuum state) as input. a) Often the input state will not be changed by the machine and the first output channel will be identical to the input one. b) In the event of successful transformation operated by the system, a particular state $|\psi_2\rangle$ will be produced at the output 2 and its detection will announce the presence of the desired manipulated state $\hat{O}_1|\Psi_1\rangle$ at the output 1. That's why we speak of conditioned (on the ancillary state $|\psi_2\rangle$ detection) implementation of the operation $\hat{O}$.

with $\hat{J}(\hat{a}_1, \hat{a}_2, \hat{a}_1^\dagger, \hat{a}_2^\dagger)$ hermitian operator generator of the transformation, defined in the addition case as

$$\hat{J}(\hat{a}_1, \hat{a}_2, \hat{a}_1^\dagger, \hat{a}_2^\dagger) = \hat{a}_1^\dagger \hat{a}_2^\dagger + \hat{a}_1 \hat{a}_2 \tag{3.2}$$

and in the subtraction one as

$$\hat{J}(\hat{a}_1, \hat{a}_2, \hat{a}_1^\dagger, \hat{a}_2^\dagger) = \hat{a}_1 \hat{a}_2^\dagger + \hat{a}_1^\dagger \hat{a}_2 \tag{3.3}$$

The label 1 refers to the mode target of the transformation, the label 2 to the ancillary mode. For sake of simplicity we now focus the analysis on the addition case, as nothing changes in the subtraction one. Furthermore, it is important to point out that we limit the formalism to the pure state case.
In the small parameter regime, $\theta \approx 0$, and in the case of small mean photon number states, the creation operator is implemented nondeterministically on the mode 1, with a quasi-zero success probability. Thus we can write the first-order approximation

$$\begin{aligned} \hat{U}|\Psi_1\rangle|0_2\rangle &= \mathcal{N}\left\{\left[\hat{I} + i\theta\left(\hat{a}_1^\dagger \hat{a}_2^\dagger + \hat{a}_1 \hat{a}_2\right) + O(\theta^2)\right]|\Psi_1\rangle|0_2\rangle\right\} \\ &\approx \mathcal{N}\left\{|\Psi_1\rangle|0_2\rangle + i\theta \hat{a}_1^\dagger|\Psi_1\rangle|1_2\rangle\right\}. \end{aligned} \tag{3.4}$$

The detection of a photon in the ancillary mode 2 projects the initial state on the desired single-photon added one

$$\mathcal{N}\left\{|\Psi_1\rangle|0_2\rangle + i\theta \hat{a}_1^\dagger|\Psi_1\rangle|1_2\rangle\right\} \xrightarrow[heralding]{\hat{I}_2 - |0_2\rangle\langle 0_2|} \hat{a}_1^\dagger|\Psi_1\rangle. \tag{3.5}$$

The key of this approach is that now the creation of a photon in the mode 1 is always accompanied by the creation of a second photon in the mode 2. This means that, independently of how small the probability is, the successful implementation is always announced by the detection of the ancillary photon.
Actually, a more complicated superposition of other terms including multiple additions and subtractions should be considered, especially if θ^2 becomes high or there are significant contributions from multiphoton components in the

Fock expansion of the state $|\Psi\rangle = \sum_n c_n|n\rangle$. All the experiments analyzed in this work have been however performed in a mean photon number regime ≈ 1, thus permitting to ignore the multiple operation contributions. The error committed by considering valid this approximation is then of the order of θ^2, like the magnitude of the coefficient of the first ignored term of the collapsed mixture selected by single photon detection[1]

$$\hat{U}|\Psi_1\rangle|0_2\rangle \xrightarrow[heralding]{\hat{I}_2-|0_2\rangle\langle 0_2|} \begin{cases} \hat{a}_1^\dagger|\Psi_1\rangle & \text{with probability } \approx 1-\theta^2 \\ (\hat{a}_1^\dagger)^2|\Psi_1\rangle & \text{with probability } \approx \theta^2 \end{cases} \tag{3.6}$$

The parameter θ must be then chosen as the best compromise between a faithful implementation of the desired conditioned operation, and a good rate of events, since as we can see from eq.(3.5), also the success probability is proportional to θ^2.

3.1 Conditioned single-photon subtraction

The subtraction of exactly one photon from a travelling wave is a basic operation intuitively interpretable as a controlled loss. The analogy goes beyond a simple picture and presents formal analogies with the beam-splitter-based model of losses, as we will see.
Single photon subtraction inspired several experiments during the years, like Schrödinger's cat state realization [**?**],[33], enhanced quantum metrology [32] and fundamental tests [34], making this only apparently trivial operation an indispensable tool in modern quantum optics.

3.1.1 Unitary BS transformation

The unitary transformation of eq.(3.1) with (3.3), can be easily implemented just considering the effect of a beam splitter on a generic bipartite input system

$$\hat{U} = \hat{U}_{BS} = e^{i\theta\left(\hat{a}_1\hat{a}_2^\dagger + \hat{a}_1^\dagger\hat{a}_2\right)}. \tag{3.7}$$

---

[1] With photon number resolving detectors the analysis will be slightly different.

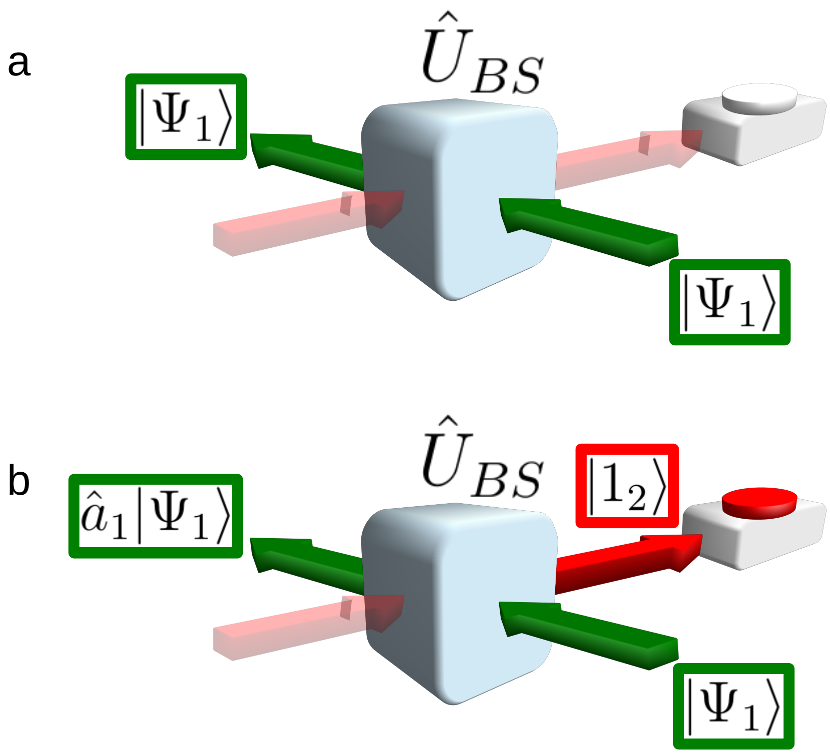

Figure 3.2: When a state $|\Psi_1\rangle$ in injected into the mode 1 and the vacuum $|0_2\rangle$ into the mode 2 of a small-reflectivity beam splitter, a) almost always no modification occurs to the initial state but b) there is still a small probability that one and only one photon of the target beam $|\Psi_1\rangle$, after reflection, will leave the beam splitter from the other output mode. The detection of this particle on mode 2 will announce the presence of the desired single-photon-subtracted target state $\hat{a}_1|\Psi\rangle$ at the output mode 1.

where $\cos^2\theta$ is the transmittivity $\mathcal{T}$ of the beam splitter. Indeed, it is straightforward to check that if one injects a single photon on one input arm, the operator (3.7) delocalizes it between the output modes

$$\begin{aligned}
\hat{U}_{BS}|1,0\rangle &= \hat{U}_{BS}\hat{a}_1^\dagger|0,0\rangle \\
&= \hat{U}_{BS}\hat{a}_1^\dagger\hat{U}_{BS}^\dagger\hat{U}_{BS}|0,0\rangle \\
&= \hat{U}_{BS}\hat{a}_1^\dagger\hat{U}_{BS}^\dagger|0,0\rangle \\
&= \left(\hat{a}_1^\dagger\cos\theta + i\hat{a}_2^\dagger\sin\theta\right)|0,0\rangle \\
&= \cos\theta|1,0\rangle + i\sin\theta|0,1\rangle \qquad (3.8)
\end{aligned}$$

or if instead two photons are injected along the two inputs, at the output one gets

$$\begin{aligned}
\hat{U}_{BS}|1,1\rangle &= \hat{U}_{BS}\hat{a}_1^\dagger\hat{a}_2^\dagger|0,0\rangle \\
&= \hat{U}_{BS}\hat{a}_1^\dagger\hat{U}_{BS}^\dagger\hat{U}_{BS}\hat{a}_2^\dagger\hat{U}_{BS}^\dagger\hat{U}_{BS}|0,0\rangle \\
&= \frac{\sin(2\theta)}{\sqrt{2}}\left(|2,0\rangle - |0,2\rangle\right) + \cos(2\theta)|1,1\rangle, \qquad (3.9)
\end{aligned}$$

that means no coincidences at all at the output modes in case of a balanced beam splitter, that is when $\theta = \pi/4$.

3.1.2 Polarization encoding

For the conditioned implementation of single photon subtraction we have to focus our analysis to the $\theta \approx 0$ case, as shown on eq.(3.4). We will inject our target state $|\Psi_1\rangle$ into mode 1 of a small reflectivity beam splitter, and in case of single photon detection at the second output mode, the desired single photon subtracted target state will come out the beam splitter [2].
Actually, all along this work we will never consider spatial degrees of freedom, as we indeed experimentally preferred to encode the quantum states by making use of polarization modes, defined by the light components horizontally and vertically polarized. In this framework the analogous of a beam splitter for spatial modes, is certainly represented by an half-wave-plate. This optical device is a foil of a birefringent material cut with a proper thickness such to retard of π the *extraordinary* (*ordinary*) polarization component with respect to the *ordinary* (*extraordinary*), for a fixed wavelength. This means

that a linear polarization going through the plate will be rotated of an angle 2γ, with the angle γ defined by the entering polarization direction and the ordinary axis of the birefringent crystal (see Appendix C).
The analogy with the beam splitter can be mathematically demonstrated by considering that the input/output relations

$$\begin{pmatrix} \hat{a}'_H \\ \hat{a}'_V \end{pmatrix} = \begin{pmatrix} c_{HH} & c_{HV} \\ c_{VH} & c_{VV} \end{pmatrix} \begin{pmatrix} \hat{a}_H \\ \hat{a}_V \end{pmatrix} \tag{3.10}$$

with $c_{HH} = c_{VV} = \cos(2\gamma), c_{HV} = c_{VH} = i\sin(2\gamma)$ together with the conservation of the number of particles $\hat{n}_H + \hat{n}_V = \hat{n}'_H + \hat{n}'_V$ are formally identical to the beam splitter ones. The small reflectivity condition of eq.(3.4) can thus be fulfilled by considering a slightly rotated HWP[3], i.e. with $\gamma \ll 1$.
Polarization encoding enables an intrinsic stability hardly achievable by using other degrees of freedom, due to the fact that the two considered modes travel naturally together within the wave, experiencing the same drifts or vibrations of any optical element and thus allowing compensation-free schemes. Birefringence permits anyway to manipulate the two modes independently when necessary.
We have seen that the HWP's subtraction is based on the rotation of one photon, the ancillary, on an a different polarization mode. However the conditioning detection requires now to separate spatially the two copropagating H and V modes and this can be accomplished by making use of a polarizing beam splitter.
Polarization encoding also permits to implement very easily the displacement operator $\hat{D}(\alpha)$, as in the small mean photon number regime it can be realized by mixing a target state with a strong coherent state $|\alpha\rangle$ into a low reflectivity beam splitter (see [23] for further details about the implementation of the displacement).

3.1.3 Choice of parameters

We have already seen that the parameter θ must be chosen as a compromise between a good fidelity and an high implementation rate of the desired single photon operation. If we limit to initial states with small amplitudes, for instance single photons $|1\rangle$ or coherent states $|\alpha\rangle$ with a mean photon number $|\alpha|^2 \approx 1$, by setting the HWP angle to 5 degrees, from the Malus law we find a success probability of $\approx 3\%$. If we consider also that the APD used to

herald the operation has a detection efficiency of $\approx 60\%$ and the single mode fiber used to couple the light to the same detector has a coupling efficiency of $\approx 80\%$, by using a pulsed laser with a $80MHz$ repetition rate, we get a subtraction rate of $\approx 80MHz \cdot 3\% \cdot 60\% \cdot 80\% = 1.1MHz$.
This choice implies an error of $\approx 3\%$ in the $\hat{a}$ implementation fidelity.
From the experimental point of view this choice seemed an acceptable compromise, so all the experiments described in this thesis have been performed in these conditions.

3.1.4 Single-mode subtraction

The single mode approximation previously discussed (see Sec.1.4), requires that the single photon subtraction operation has to be implemented on the same mode of the target state, i.e. that photons with a given mode must be subtracted from states with the same spatio-temporal properties. To achieve this condition, the APD used to herald the single photon annihilation operation has been coupled to the target beam by means of a single mode fiber. The spatial propagation mode of the fiber has thus been matched to the spatial mode of the target state by using a system composed of two lenses, resulting in an efficiency of $\approx 80\%$ of fiber-coupled photons.

3.2 Conditioned single-photon addition

The ability to implement the addition of exactly one photon with well defined spatio-temporal characteristics, is a fundamental task in quantum optics as it enables the realization of high purity single photon sources used for fundamental test of quantum mechanics, cryptography, quantum computation, etc.

3.2.1 Unitary PDC transformation

A very well tested method used to implement the addition of a single photon on a given target light state is by the parametric down conversion process (PDC). PDC is a process in which an incoming photon called *pump* nonlinearly interacts with the atoms of a crystal, with the subsequent simultaneous emission of a couple of low-frequency photons[24], called *signal* and *idler*, according to the energy and momentum conservation laws

$$\omega_p = \omega_s + \omega_i \tag{3.11}$$

$$\boldsymbol{k}_p = \boldsymbol{k}_s + \boldsymbol{k}_i, \tag{3.12}$$

where the subscript p, s, i denote pump, signal and idler. Actually no atomic level corresponds to the pump energy, so the photon annihilation corresponds to a very short-lived virtual atomic state excitation with the atoms playing the passive static role of a light transition catalyst. Classically PDC can be considered a three wave mixing process in which energy is exchanged between pump and signal/idler with an amplification factor dependent on the fields relative phase (OPA). In this context, optical amplifiers can be explained only by admitting the initial presence of the signal (or idler) to *stimulate* the conversion. Conversely in quantum mechanics the process can occur also in spontaneous conditions, i.e. without the low-frequency beam, because the transition is naturally stimulated by the random vacuum fluctuations. In the first case we speak of stimulated parametric down conversion (stimulated PDC), in the second of spontaneous parametric down conversion (spontaneous PDC or SPDC).
Equations (3.11) and (3.12) show that the down-converted photons are correlated in energy and momentum in a nonclassical way as we will see next. To understand the origin of the down conversion process, let's forget for the moment the conservation equations (3.11) and (3.12) and introduce the classical field-matter interaction Hamiltonian [28]

$$H(t) = \int_V \boldsymbol{E}(\boldsymbol{r}, t) \cdot \boldsymbol{P}(\boldsymbol{r}, t) \, d\boldsymbol{r} \tag{3.13}$$

where $\boldsymbol{E}(\boldsymbol{r}, t)$ is the electric field vector, $\boldsymbol{P}(\boldsymbol{r}, t)$ is the macroscopic polarization, i.e. the dipole moment naturally present or induced by $\boldsymbol{E}$ into the material and V is the interaction region, i.e. the crystal volume. The common way to proceed is writing $\boldsymbol{P}(\boldsymbol{r}, t)$ as series of $\boldsymbol{E}(\boldsymbol{r}, t)$

$$P_l(\boldsymbol{r}, t) = \chi^{(1)}_{lm}(\boldsymbol{r}) E_m(\boldsymbol{r}, t) + \chi^{(2)}_{lmn}(\boldsymbol{r}) E_m(\boldsymbol{r}, t) E_n(\boldsymbol{r}, t) + \ldots \qquad \forall l, m, n = 1, 2 \tag{3.14}$$

where the summation over repeated indices is assumed and the zero order term of the series has been taken as 0 since we are considering a material with a vanishing permanent dipole moment. The subscripts l, m, n run over the two components of polarization and $\chi^{(1)}_{lm}$ and $\chi^{(2)}_{lmn}$ are second and third order susceptivity tensors. Since we are interested only up to the second order element of the series, we can ignore the higher terms. By putting eq.(3.14) into (3.13) we obtain

$$
\begin{aligned}
H(t) &= \int_V \chi^{(1)}_{lm}(\boldsymbol{r})\, E_l(\boldsymbol{r},t)\, E_m(\boldsymbol{r},t)\ d\boldsymbol{r} + \\
&+ \int_V \chi^{(2)}_{lmn}(\boldsymbol{r})\, E_l(\boldsymbol{r},t)\, E_m(\boldsymbol{r},t)\, E_n(\boldsymbol{r},t)\ d\boldsymbol{r} \qquad (3.15) \\
&= H_0(t) + H_{int}(t). \qquad (3.16)
\end{aligned}
$$

$\hat{H}_0(t)$ represents the electromagnetic free field energy but we are interested in the interaction dynamics, so let's only only focus on the second term $\hat{H}_{int}(t)$. Let's substitute in it the vector fields with their quantum operatorial counterparts

$$
\hat{H}_{int}(t) = \int_V \chi^{(2)}_{lmn}(\boldsymbol{r})\, \hat{E}_l(\boldsymbol{r},t)\, \hat{E}_m(\boldsymbol{r},t)\, \hat{E}_n(\boldsymbol{r},t)\ d\boldsymbol{r} \qquad (3.17)
$$

with the electric field operator

$$
\hat{E}_l(\boldsymbol{r},t) = \int \hat{a}_l(\boldsymbol{k},\omega)\, e^{-i(\boldsymbol{k}\cdot\boldsymbol{r}-\omega t)} + \hat{a}^\dagger_l(\boldsymbol{k},\omega)\, e^{i(\boldsymbol{k}\cdot\boldsymbol{r}-\omega t)}\ d\boldsymbol{k}\, d\omega \qquad (3.18)
$$

defined using its plane-wave decomposition. The resulting Hamiltonian is quite complicated, but basically we are interested in the sole term

$$
\begin{aligned}
\hat{H}_{PDC}(t) &= \int \chi^{(2)}_{lmn}(\boldsymbol{r}) \hat{a}_l(\boldsymbol{k}_p,\omega_p)\, \hat{a}^\dagger_m(\boldsymbol{k}_s,\omega_s)\, \hat{a}^\dagger_n(\boldsymbol{k}_i,\omega_i) \cdot \\
&\cdot e^{-i[(\boldsymbol{k}_p-\boldsymbol{k}_s-\boldsymbol{k}_i)\cdot\boldsymbol{r}-(\omega_p-\omega_s-\omega_i)t]}\ d\boldsymbol{k}_p\, d\omega_p\, d\boldsymbol{k}_s\, d\omega_s\, d\boldsymbol{k}_i\, d\omega_i\, d\boldsymbol{r}
\end{aligned}
\qquad (3.19)
$$

where the subscripts p, s, i have been introduced to distinguish the integration variables. In the interaction representation the operator (3.19) governs the temporal evolution of the state according to the Schrödinger's equation

$$i\hbar\frac{d}{dt}|\Psi(t)\rangle = \hat{H}_{PDC}(t)|\Psi(t)\rangle. \tag{3.20}$$

We can then define the corresponding unitary time evolution operator $\hat{U}_{int}(t)$

$$|\Psi(t)\rangle = \hat{U}_{int}(t)|\Psi(0)\rangle \tag{3.21}$$

and by putting it into eq.(3.20) we obtain the differential equation

$$i\hbar\frac{d}{dt}\hat{U}_{int}(t) = \hat{H}_{PDC}(t)\hat{U}_{int}(t) \tag{3.22}$$

with solution

$$\hat{U}_{PDC}(t) = \hat{I} - \frac{i}{\hbar}\int_{-\infty}^{t} \hat{H}_{int}(t')\,\hat{U}_{int}(t')\ dt' \tag{3.23}$$

where the initial condition has been taken as

$$\lim_{t\to-\infty}\hat{U}_{int}(t) = \hat{I}.$$

By making use of the Dyson series[25], the solution (3.23) can be rewritten as

$$\hat{U}_{PDC}(t) \quad = \quad e^{-i\int_{-\infty}^{t}\hat{H}_{PDC}(t')\ dt'} \tag{3.24}$$

and by considering that the coefficients $\chi^{(2)}_{lmn}$ are of the order $10^{-11}\div10^{-8}$, we can write the first order approximation

$$\hat{U}_{PDC}(t) \approx \hat{I} - i\int_{-\infty}^{t}\hat{H}_{PDC}(t')\ dt'. \tag{3.25}$$

The transformation (3.24) and its approximated version (3.25), apart from the integrals necessary to define the mode, has the desired form of the conditioned single photon addition of eq.(3.1).

3.2.2 Phase-matching conditions

Suppose now that the wavefunction is at the initial time a coherent state of amplitude Π

$$|\Psi(0)\rangle = |\Pi\rangle \tag{3.26}$$

The injection of this initial state onto the crystal produces an evolution of the state governed by the propagator of eq.(3.25) as

$$\begin{aligned}
|\Psi(t)\rangle &= \hat{U}_{PDC}(t)|\Psi(0)\rangle \\
&= |\Pi\rangle - i\int_{-\infty}^{t} \hat{H}_{PDC}(t')\ dt'|\Pi\rangle \\
&= |\Pi\rangle - i\iint_{-\infty}^{t} \chi^{(2)}_{lmn}(\boldsymbol{r})\, e^{-i(\Delta\boldsymbol{k}\cdot\boldsymbol{r}-\Delta\omega t')}\ \cdot \\
&\cdot\ \ \hat{a}_l(\boldsymbol{k}_p,\omega_p)\, \hat{a}^\dagger_m(\boldsymbol{k}_s,\omega_s)\, \hat{a}^\dagger_n(\boldsymbol{k}_i,\omega_i)|\Pi\rangle\, d\boldsymbol{k}_p\, d\omega_p\, d\boldsymbol{k}_s\, d\omega_s\, d\boldsymbol{k}_i\, d\omega_i\, dt'\, d\boldsymbol{r} \\
&= |\Pi\rangle - i\iint_{-\infty}^{t} \chi^{(2)}_{lmn}(\boldsymbol{r})\, e^{-i(\Delta\boldsymbol{k}\cdot\boldsymbol{r}-\Delta\omega t')}\ \cdot \\
&\cdot\ \ \Pi_l(\boldsymbol{k}_p,\omega_p)\, \hat{a}^\dagger_m(\boldsymbol{k}_s,\omega_s)\, \hat{a}^\dagger_n(\boldsymbol{k}_i,\omega_i)|\Pi\rangle\, d\boldsymbol{k}_p\, d\omega_p\, d\boldsymbol{k}_s\, d\omega_s\, d\boldsymbol{k}_i\, d\omega_i\, dt'\, d\boldsymbol{r}
\end{aligned} \tag{3.27}$$

where we exploited the eigenrelation[2]

$$\hat{a}_l(\boldsymbol{k}_p,\omega_p)|\Pi\rangle = \Pi_l(\boldsymbol{k}_p,\omega_p)|\Pi\rangle \tag{3.28}$$

and Π_l refers to the lth component of polarization of the coherent state $|\Pi\rangle$.

Since we are interested in a final state far from the crystal, the time integration in eq.(3.27) can be safely extended to $t \to +\infty$ being the interaction Hamiltonian zero immediately before and after the interaction within the crystal. The integral can then be easily performed as

$$\int_{-\infty}^{+\infty} e^{i\Delta\omega t'}\ dt' = \delta(\omega_p - \omega_s - \omega_i) \tag{3.29}$$

---

[2] In eq.(3.27) we implicitly exploited the fact that $\hat{a}_l(\boldsymbol{k}_p,\omega_p)$ commutes with $\hat{a}^\dagger_m(\boldsymbol{k}_s,\omega_s)$ and $\hat{a}^\dagger_n(\boldsymbol{k}_i,\omega_i)$ as we will see from eqs.(3.35),(3.29).

and if $\chi^{(2)}_{lmn}(\boldsymbol{r})$ can be considered constant over the integration volume[3], eq.(3.27) simplifies further as

$$\begin{aligned}|\Psi(t)\rangle &= |\Pi\rangle - \\ &+ \int \phi_{lmn}(\boldsymbol{k}_s,\omega_s,\boldsymbol{k}_i,\omega_i)\hat{a}^{\dagger}_m(\boldsymbol{k}_s,\omega_s)\,\hat{a}^{\dagger}_n(\boldsymbol{k}_i,\omega_i)\,|\Pi\rangle\,d\boldsymbol{k}_s\,d\omega_s\,d\boldsymbol{k}_i\,d\omega_i.\end{aligned} \tag{3.30}$$

The distribution

$$\phi(\boldsymbol{k}_s,\omega_s,\boldsymbol{k}_i,\omega_i) = i\chi^{(2)}_{lmn}\int \Pi_l(\boldsymbol{k}_p,\omega_s+\omega_i)\,K(\Delta\boldsymbol{k})\;d\boldsymbol{k}_p\,d\boldsymbol{r} \tag{3.31}$$

with

$$K(\Delta\boldsymbol{k}) = \int_V e^{-i\Delta\boldsymbol{k}\cdot\boldsymbol{r}}\,d\boldsymbol{r} \tag{3.32}$$

defines the mode of *signal* and *idler* on which the double addition will take place. Let's notice that this mode can be interpreted as the convolution of two contributions, the first one fixed by the absorbed *pump* photon and the second one by the volume of the crystal. The state (3.30) can be reexpressed by explicitly indicating the creation of two *entangled* photons in the *signal* and *idler* modes, the so-called *biphoton state* $|1,1_\phi\rangle$

$$\begin{aligned}|\Psi(t)\rangle &= |\Pi\rangle - c|\Pi\rangle|1,1_\phi\rangle \\ &= |\Pi\rangle - \int \phi_{lmn}(\boldsymbol{k}_s,\omega_s,\boldsymbol{k}_i,\omega_i)\,d\boldsymbol{k}_s\,d\omega_s\,d\boldsymbol{k}_i\,d\omega_i\,|\Pi\rangle|1^m_{\boldsymbol{k}_s,\omega_s}\rangle|1^n_{\boldsymbol{k}_i,\omega_i}\rangle\end{aligned} \tag{3.33}$$

Pay attention that, because of the *entanglement*, *signal* and *idler* modes can't be properly defined until their measurement.
Integration over the crystal volume (3.32) can be easily performed as

---

[3] We also ignored any dispersive dependence of the susceptivity from the frequency.

$$\begin{aligned} K(\Delta\boldsymbol{k}) &= \int_{-\frac{L_x}{2}}^{+\frac{L_x}{2}} e^{-i\Delta k_x x}\, dx \int_{-\frac{L_y}{2}}^{+\frac{L_y}{2}} e^{-i\Delta k_y y}\, dy \int_{-\frac{L_z}{2}}^{+\frac{L_z}{2}} e^{-i\Delta k_z z}\, dz \\ &= 8\frac{\sin\left(\Delta k_x L_x/2\right)}{\Delta k_x}\frac{\sin\left(\Delta k_y L_y/2\right)}{\Delta k_y}\frac{\sin\left(\Delta k_z L_z/2\right)}{\Delta k_z} \end{aligned} \tag{3.34}$$

which has a maximum in

$$\boldsymbol{k}_p = \boldsymbol{k}_s + \boldsymbol{k}_i. \tag{3.35}$$

Equations (3.29) and (3.35) are called *phase matching conditions* and guarantee that the maximum conversion efficiency occurs according to the energy and momentum conservation.
Let's focus now on the polarization. Three cases only are possible: if $l = m = n$, *pump*, *signal* and *idler* posses the same polarization and we speak of *type 0 parametric down conversion*, if $l \neq m = n$, *signal* and *idler* are differently polarized respect to the *pump* and we speak of *type I parametric down conversion*, if $l = m \neq n$ or $l = n \neq m$, *pump* and *signal* or *pump* and *idler* have the same polarization and we speak of *type II parametric down conversion*.
By using both the phase matching conditions we obtain in the type 0 PDC

$$n(\omega_s + \omega_i)\,(\omega_s + \omega_i)\,\frac{\boldsymbol{k}_p}{|\boldsymbol{k}_p|} = n(\omega_s)\omega_s\frac{\boldsymbol{k}_s}{|\boldsymbol{k}_s|} + n(\omega_i)\omega_i\frac{\boldsymbol{k}_i}{|\boldsymbol{k}_i|} \tag{3.36}$$

which has no solution in common crystals as the refractive index is tipically an increasing function of ω[4].
By considering a crystal with nonvanishing birefringence and indicating with e, o the extraordinary and ordinary polarization components (see Appendix C) we obtain for the type I

$$n_{e,o}(\omega_s + \omega_i)\,(\omega_s + \omega_i)\,\frac{\boldsymbol{k}_p}{|\boldsymbol{k}_p|} = n_{o,e}(\omega_s)\omega_s\frac{\boldsymbol{k}_s}{|\boldsymbol{k}_s|} + n_{o,e}(\omega_i)\omega_i\frac{\boldsymbol{k}_i}{|\boldsymbol{k}_i|} \tag{3.37}$$

and similarly for type II.
We are interested in the type I in the degenerate case of $\omega_s = \omega_i$, so

$$2\, n_{e,o}(2\omega_s)\frac{\boldsymbol{k}_p}{|\boldsymbol{k}_p|} = n_{o,e}(\omega_s)\left(\frac{\boldsymbol{k}_s}{|\boldsymbol{k}_s|} + \frac{\boldsymbol{k}_i}{|\boldsymbol{k}_i|}\right) \tag{3.38}$$

---

[4] Indeed type 0 PDC can be realized only in periodically poled engineered crystals.

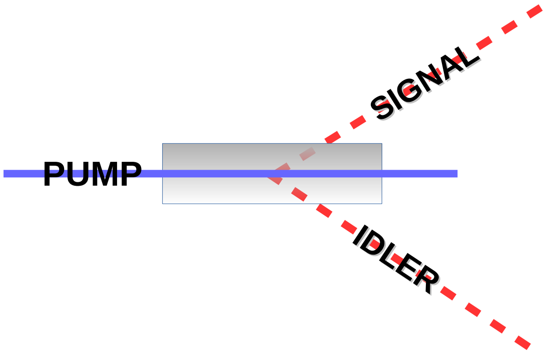

Figure 3.3: Schematic representation of the degenerate spontaneous parametric down conversion (SPDC). A photon in the *pump* mode is absorbed, and a couple of photons are emitted in the *signal* and *idler* modes. In the degenerate case *signal* and *idler* possess the same frequency.

Without loss of generality we can choose $\boldsymbol{k}_p$ parallel to the z axis. Eq.(3.38) then becomes

$$\frac{k_s^{x,y}}{|\boldsymbol{k}_s|} + \frac{k_i^{x,y}}{|\boldsymbol{k}_i|} = 0 \tag{3.39}$$

$$2\, n_{e,o}(2\omega_s) = \quad n_{o,e}(\omega_s)\left(\frac{k_s^z}{|\boldsymbol{k}_s|} + \frac{k_i^z}{|\boldsymbol{k}_i|}\right) \tag{3.40}$$

In all the experiments presented in this thesis, the *pump* is horizontal while *signal* and *idler* vertically polarized.
Equation (3.39) asserts that the type I degenerate parametric down conversion emission occurs along cones of different colors.

3.2.3 Single-mode addition

The generation of the biphoton state $|1, 1_\phi\rangle$ of eq.(3.33), allows one to use parametric downconverter crystals as sources of temporally well localized single photons, via herald detection of the other photon of the pair [24]. Indeed, the simple measure of one of the two particles, let's say just for convention the *idler* one, causes the collapse of the initial state onto a one-photon state distributed on a statistical mixture of several *signal* modes[5]

---

[5] For sake of simplicity, we still consider of injecting vacuum in the signal and idler modes.

$$
\begin{aligned}
\hat{\rho}_s &= Tr_i \left\{ \int |1_{\boldsymbol{k}_i,\omega_i}\rangle\langle 1_{\boldsymbol{k}_i,\omega_i}| \; d\boldsymbol{k}_i \, d\omega_i |\Psi(t)\rangle\langle\Psi(t)| \right\} \\
&= \sum_n \int \langle n_{\boldsymbol{k}'_i,\omega'_i}|1_{\boldsymbol{k}_i,\omega_i}\rangle\langle 1_{\boldsymbol{k}_i,\omega_i}|\Psi(t)\rangle\langle\Psi(t)|n_{\boldsymbol{k}'_i,\omega'_i}\rangle \; d\boldsymbol{k}_i \, d\omega_i \, d\boldsymbol{k}'_i \, d\omega'_i \\
&= \int \langle 1_{\boldsymbol{k}_i,\omega_i}|\Psi(t)\rangle\langle\Psi(t)|1_{\boldsymbol{k}_i,\omega_i}\rangle \; d\boldsymbol{k}_i \, d\omega_i \\
&= \int \phi(\boldsymbol{k}'_s,\omega'_s,\boldsymbol{k}'_i,\omega'_i)\phi^*(\boldsymbol{k}''_s,\omega''_s,\boldsymbol{k}''_i,\omega''_i) \, |1_{\boldsymbol{k}'_s,\omega'_s}\rangle\langle 1_{\boldsymbol{k}'_s,\omega'_s}| \cdot \langle 1_{\boldsymbol{k}_i,\omega_i}|1_{\boldsymbol{k}'_i,\omega'_i}\rangle\langle 1_{\boldsymbol{k}''_i,\omega''_i}|1_{\boldsymbol{k}_i,\omega_i}\rangle \cdot \\
&\cdot \; d\boldsymbol{k}_i \, d\omega_i \, d\boldsymbol{k}'_s \, d\omega'_s \, d\boldsymbol{k}''_s \, d\omega''_s \, d\boldsymbol{k}'_i \, d\omega'_i \, d\boldsymbol{k}''_i \, d\omega''_i \\
&= \int \phi(\boldsymbol{k}_s,\omega_s,\boldsymbol{k}_i,\omega_i)\phi^*(\boldsymbol{k}_s,\omega_s,\boldsymbol{k}_i,\omega_i) \, |1_{\boldsymbol{k}_s,\omega_s}\rangle\langle 1_{\boldsymbol{k}_s,\omega_s}| \cdot \\
&\cdot \; d\boldsymbol{k}_i \, d\omega_i \, d\boldsymbol{k}_s \, d\omega_s \\
&= \int \Phi(\boldsymbol{k}_s,\omega_s) \, |1_{\boldsymbol{k}_s,\omega_s}\rangle\langle 1_{\boldsymbol{k}_s,\omega_s}| \, d\boldsymbol{k}_s \, d\omega_s \\
&= \int \Phi(\boldsymbol{k}_s,\omega_s) \, \hat{a}^\dagger(\boldsymbol{k}_s,\omega_s) \, |0\rangle\langle 0| \, \hat{a}(\boldsymbol{k}_s,\omega_s) \; d\boldsymbol{k}_s \, d\omega_s
\end{aligned}
\tag{3.41}
$$

where Tr_i indicates the trace over the *idler* degrees of freedom. The result (3.41) has been obtained by exploiting the phase matching conditions (3.29) and (3.35).
The function

$$
\Phi(\boldsymbol{k}_s,\omega_s) = \int |\phi(\boldsymbol{k}_s,\omega_s,\boldsymbol{k}_i,\omega_i)|^2 \; d\boldsymbol{k}_i \, d\omega_i \tag{3.42}
$$

is the marginal probability distribution relative to only the *signal* beam. From eq.(3.41) we see that in PDC process the simple detection of one photon is necessary to implement $\hat{a}^\dagger$, but not sufficient to aim it to a single mode.
A theoretical recipe to implement single mode addition from PDC sources has been developed by Ou in 1997 [26] and later deepened by Aichele and al. [27]. The two analyses agree in affirming that a narrowband spatio-spectral filter should be used in the heralding *idler* channel to produce high purity transform-limited single photons in the *signal* one. Without entering into the formal details, we can get an intuitive picture of what this means by considering an ideal delta-shaped filtered *idler* detection described by the density matrix

$$\hat{\rho}_d = \int \delta(\boldsymbol{k}_i - \boldsymbol{k}_f)\delta(\omega_i - \omega_f)\, |1_{\boldsymbol{k}_i,\omega_i}\rangle\langle 1_{\boldsymbol{k}_i,\omega_i}|\; d\boldsymbol{k}_i\, d\omega_i \tag{3.43}$$

where $\boldsymbol{k}_f$ and $\omega_f = \omega_p/2$ are respectively the central wave vector and frequency of the ideal *idler* filter. By substituting into eq.(3.41) the projector $|1_{\boldsymbol{k}_i,\omega_i}\rangle\langle 1_{\boldsymbol{k}_i,\omega_i}|$ with the delta filter (3.43) we obtain the highly pure signal density matrix

$$\begin{aligned} \hat{\rho}_s &= Tr_i \left\{ \int \delta(\boldsymbol{k}_i - \boldsymbol{k}_f)\delta(\omega_i - \omega_f)\, |1_{\boldsymbol{k}_i,\omega_i}\rangle\langle 1_{\boldsymbol{k}_i,\omega_i}|\; d\boldsymbol{k}_i\, d\omega_i |\Psi(t)\rangle\langle\Psi(t)| \right\} \\ &= |1_{\boldsymbol{k}_s,\omega_s}\rangle\langle 1_{\boldsymbol{k}_s,\omega_s}| \end{aligned} \tag{3.44}$$

with $\omega_s = \omega_i = \omega_p/2$ and $\boldsymbol{k}_s$ conjugate of $\boldsymbol{k}_i = \boldsymbol{k}_f$ according to the phase matching conditions.

Actually, Aichele and al. showed that under reasonable hypotheses, like ignoring diffraction, spatial or temporal walkoff (by using a sufficiently short crystal) and considering gaussian collimated beams, in real scenarios it is sufficient to filter the idler detection much narrower than the pump spatial and spectral width to achieve high purity $\mathcal{P}$. Indeed the single photon spectrotemporal purity depends on the ratio $\mu_t = \sigma_t/\sigma_p$ between the spectral width σ_t of the filter used for the detection of the *idler* and the *pump* spectral width σ_p as

$$\mathcal{P}_{temp}(\mu_t) = \frac{1}{\sqrt{1 + 2\mu_t^2}}. \tag{3.45}$$

Considering also the spatial dependence brings to the same requisite of narrowband spatial filter

$$\mathcal{P}_{sp}(\mu_s) = \frac{1}{1 + 2\mu_s^2}. \tag{3.46}$$

where $\mu_s = \sigma_t'/\sigma_p'$ is the ratio of the width σ_t' of the wave-vector distribution selected by the filter used for the detection of the *idler*, and the width σ_p of the wave-vector distribution of the *pump*.

It has been shown that in some special conditions pure single photons can be produced in parametric down conversion without the necessity of filtering, permitting much higher production rate [29], [30].

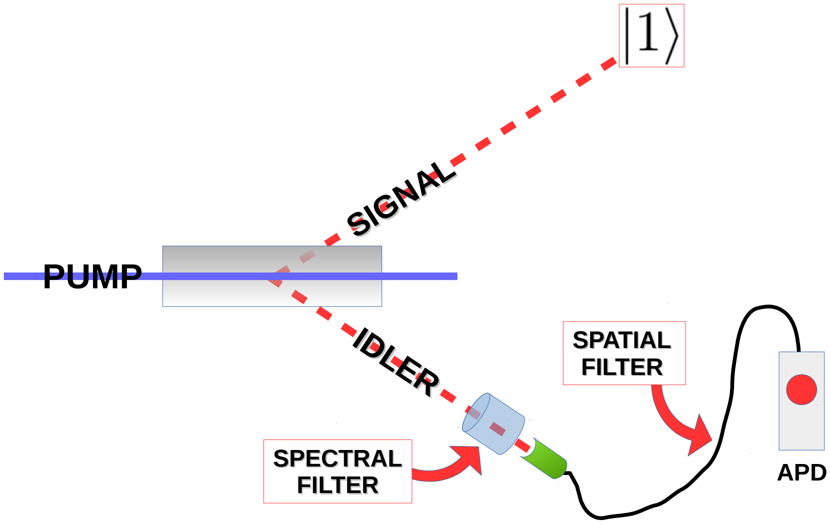

Figure 3.4: A single photon with high purity can be produced in the *signal* mode of a parametric down conversion process, by strongly filtering spectrally and spatially the heralding detection in the *idler* mode.

3.2.4 Single addition approximation

The single photon approximation discussed in the general context of one photon operations, can be considered quite well justified for PDC in our case. Indeed, we can easily demonstrate that in our conditions the multiple additions per pulse is a very unlikely event. Unlike the subtraction's case, as we don't want to complicate too much the analysis because of the phase matching conditions, it is convenient to directly give a look at the experimental parameters. Starting from a 80MHz repetition rate mode-locked laser, we inject the BBO nonlinear crystal with a power $P \approx 100\text{mW}$ at $\lambda = 393\text{nm}$ or $\nu = 7.5 \cdot 10^{14}\text{Hz}$. That corresponds to

$$\begin{aligned} \frac{P}{h\nu} &= \frac{0.1}{6.6 \cdot 10^{-34} \cdot 7.5 \cdot 10^{14}} \text{s}^{-1} \\ &\approx 2 \cdot 10^{17} \text{s}^{-1} \end{aligned} \tag{3.47}$$

injected pump photons per second or

$$\frac{2 \cdot 10^{17}}{8 \cdot 10^{7}} \approx 2 \cdot 10^{9} \tag{3.48}$$

pump photons per pulse. By measuring a stimulated PDC detection rate in the idler mode of ≈ 2000cps, we can infer a downconversion event every

$$\frac{2 \cdot 10^{17}}{2000} \approx 10^{14} \tag{3.49}$$

pump photons or every

$$\frac{2 \cdot 10^{14}}{2 \cdot 10^{9}} \approx 10^{5} \tag{3.50}$$

pump pulses. That means a downconversion probability of about 10^{-5} per pump pulse and a negligible 10^{-10} for double additions within the same pulse. Taking into account a finite-detection efficiency of the used APD ($\approx 60\%$) and a non-ideal air-fiber optic coupling ($\approx 80\%$) does not change the conclusion.

Today great efforts are directed towards the development of novel methods enabling higher single and multiple photon production rates. As previously mentioned, particular engineered crystals permit special phase matching conditions without the need for tight spectral filtering in the idler mode, allowing the direct generation of pure Fock states up to $n = 3$ [36]. Another approach is based on exploiting periodically poled crystals (PPC), where the orientation of a birefringent material is periodically inverted thus allowing photons to never interfere destructively, even if generated at different longitudinal positions. Walkoff is also compensated enabling stronger beam focusing. Periodically poled potassium-titanyl phosphate crystal for instance has been used as an high rate single photon source allowing an on-the-fly tomography based alignment of the setup [35]. Finally, multiphoton generation has been also demonstrated possible with the use of pump enhancement cavities, permitting stronger light-matter nonlinear interactions due to the higher pump intensity [37], [38].

3.2.5 Preparation efficiency

Like the parameter η_{det} for the detection stage, for the generation too an *efficiency* η_{gen} can be introduced to quantify the quality of the single photon source. Since we have seen that the simultaneous generation of more than one couple of photons is an extremely rare event, we can identify in the heralding process the main cause of degradation in the single photon generation, and define η_{gen} as the *purity* $\mathcal{P}$

$$\eta_{gen} = \mathcal{P}_{sp} \cdot \mathcal{P}_{temp} \cdot \eta_{dark} \tag{3.51}$$

where the additional contribution η_{dark} due to the dark counts in the APD heralding detector has been considered.
A total efficiency η_{tot} can be then defined as the product of the two terms of preparation and detection

$$\eta_{tot} = \eta_{gen} \cdot \eta_{det}, \tag{3.52}$$

therefore taking into account both the sources of experimental errors. The preparation contribution should be defined according to the particular expected state[6].
To give some numbers, in our Ti:sapphire (Ti:Al_2O_3) picosecond-laser setup,

---

[6] The preparation efficiency has to depend indeed on the protocol and physical system exploited in the preparation stage.

an ultraviolet pump at $\lambda = 393$ nm with a spectral width of $\Delta\lambda \approx 0.9$nm and a beam waist $w_0 \approx 200$ μm, is used. The conditions (3.45) and (3.46) respectively on the spectrum and on the wave-vector distribution are fulfilled by filtering the idler detection with an ethalon cavity with a width $\Delta\lambda = 0.1$ and with a single mode fiber capable to select a propagation mode with a beam waist $w_0 \approx 530$ μm. By considering also the dark count contribution, the resulting observed single-photon purity is estimated in $\approx 92\%$.

3.2.6 Experimental considerations

Visibility and mode matching efficiency When dealing with single photon beams, it is basically impossible to directly have the control on the alignment and then on the mode matching efficiency (see Eq.(2.11)). Unfortunately, a good η_{mm} represents for the experimenter a necessary requisite to perform an effective homodyne measurement.

An additional bright beam, matched to the selected downconverted signal mode of the single photon, should then be used to check the alignment instead of it. To produce a bright beam with these characteristics we exploited a three wave mixing process, where a difference frequency wave is generated by the injection of the ultraviolet *pump* with a *seed* infrared *idler* spectrally matched to the ancillary detection filter. In other words, an additional coherent bright beam aligned to the *idler* mode is seeded into the crystal in order to stimulate the generation of a classical beam in the same *signal* mode of the single photon, in a three wave mixing nonlinear process. In the spatial domain a precise coupling with the *pump* is not necessary and a wider *idler seed* beam can be used. A formal demonstration can be found in [27] but we can intuitively understand it by imaging that the nonlinear interaction takes place only within the spatial overlap region, i.e. with the narrower pump acting as filter, so a broader size is a sufficient condition to produce a bright *signal* wave well matched to the selected single photon mode.

Since the generated macroscopic classical *signal* beam is well described by a coherent state of amplitude γ, it is possible to evaluate the mode matching efficiency of the single photon by measuring the visibility of the interference fringes produced by this strong signal beam with the local oscillator. So, by mixing the γ and α coherent states by means of a 50% beam splitter and supposing the two beams in phase, we get[7]

---

[7] See eq.(A.5) in Appendix A.

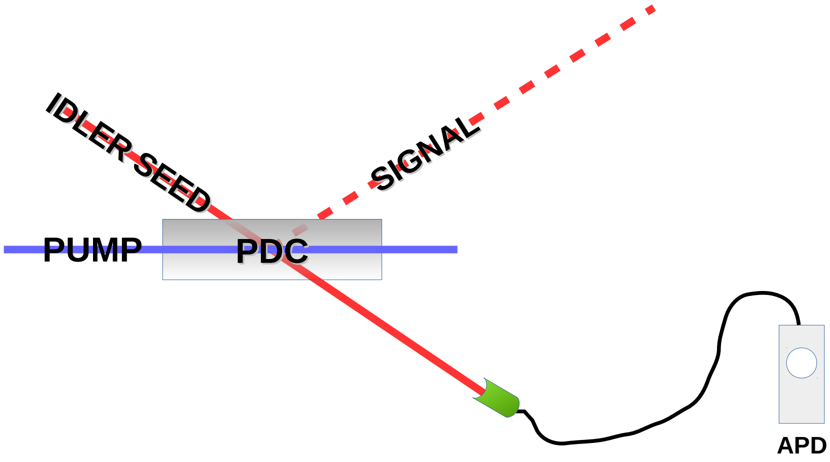

Figure 3.5: An alignment *signal* beam with the same spatio-temporal mode of the single photon can be generated in a three-wave-mixing process.

$$
\begin{aligned}
V(\gamma,\alpha) &= \frac{\int dt\, \langle M|\hat{a}^{\dagger}_{1'}(t)\hat{a}_{1'}(t)\,|M\rangle - \langle m|\int dt\, \hat{a}^{\dagger}_{1'}(t)\hat{a}_{1'}(t)\,|m\rangle}{\int dt\, \langle M|\hat{a}^{\dagger}_{1'}(t)\hat{a}_{1'}(t)\,|M\rangle + \langle m|\int dt\, \hat{a}^{\dagger}_{1'}(t)\hat{a}_{1'}(t)\,|m\rangle} \\
&= \mathcal{R}\left\{\frac{2\int dt\, \gamma^*(t)\alpha(t)}{\left[\int dt\, |\gamma(t)|^2 + \int dt\, |\alpha(t)|^2\right]}\right\} \qquad (3.53)
\end{aligned}
$$

where $|M\rangle = |\gamma_1, \alpha_2\rangle$ and $|m\rangle = |\gamma_1 e^{i\pi}, \alpha_2\rangle$ represent the states injected into the balanced beam splitter when the maximum and the minimum intensities are observed at the output mode $1'$ of the beam splitter. A phase factor $e^{i\pi/2}$ has been absorbed into the definition of $\alpha(t)$ in the calculation. Once again it can be helpful introducing modes normalized to 1, that is $\alpha(t) = \sqrt{n_{LO}}\tilde{\alpha}(t), \gamma(t) = \sqrt{n_1}\tilde{\gamma}(t)$, so eq.(3.53) becomes

$$
V(\gamma,\alpha) = \mathcal{R}\left\{\frac{2\sqrt{n_1}\sqrt{n_{LO}}\int dt\, \tilde{\gamma}^*(t)\tilde{\alpha}(t)}{n_1 + n_{LO}}\right\} \qquad (3.54)
$$

with $\mathcal{R}$ representing the real part. For beams with the same intensities, i.e. $n_1 = n_{LO}$ it provides an indication for the quality of the single-photon-mode-matching efficiency of Eq.(2.11), as

$$
V(\gamma,\alpha) = \mathcal{R}\left\{\int dt\, \tilde{\gamma}^*(t)\tilde{\alpha}(t)\right\}. \qquad (3.55)
$$

Adding of a single photon to an input beam Addition of single photons to a target beam can be easily realized provided that the injected *signal seed* is spectrally and spatially broader than the addition mode and we are not anyway interested in the part of the mode unaffected by the addition. The reason is that, as we have seen in Sec.2, the use of homodyne detection enables the measurement of a state only in that portion of the mode coupled to a *local oscillator* (LO) beam. This fact makes the detector blind to the unmatched spectral and spatial parts and then, by selecting with the LO only the portion affected by the addition, we can forget the remaining unchanged portion.

3.3 Quantum operator superpositions

The next step is the implementation of superpositions of single photon operations. Superpositions represent one of most critical, crucial and debated points of the whole quantum theory, as their existence constitutes one of the crucial points that apparently makes the microscopic and macroscopic worlds so different (see for instance [39] or [40]).

In the following of this section we analyze more in detail two particular conditioned operator superpositions at the basis of the experiments explained in the next chapters. The basic idea is just that two heralded quantum operations can be superposed whenever it is impossible the discrimination of the two corresponding ancillas.

3.3.1 Subtraction+addition/addition+subtraction

Based on this idea, we can build our superposition device by experimentally erasing any discriminating information in the heralding events we want to superimpose, always paying attention to avoid any decoherence effect due to strong interactions with the environment [43]. For instance quantum commutations rules have been tested following this approach [41], [2], [72], in a sequential scheme of addition and delocalized subtraction. Two low reflectivity beam splitters are used to implement probabilistic heralded photon subtraction before and after the downconverter. The reflected modes of the two beam splitters are then fiber coupled and properly delayed to synchronize the two ancillary path lengths at the entrance modes of a beam splitter. The beam splitter makes the two paths indistinguishable since the detection of one photon at the BS output cannot be directly related to one particular input mode. Then, the following superposition must be considered

$$c_1\hat{a}^\dagger\hat{a} + c_2 e^{i\phi}\hat{a}\hat{a}^\dagger \tag{3.56}$$

where c_1^2/c_2^2 and the relative phase ϕ can be experimentally selected by adjusting the relative intensities and phases of the ancillary announcing the two events of the superposition (see Sec.4.4.2 for an explicit analysis of the experimental parameter setting to adjust phase and weights of the superposition).

Actually, as previously seen in this thesis work, we made use of polarization degrees of freedom to implement one photon subtraction. In this case, the

two low reflectivity beam splitters have been replaced by the joint action of a couple of HWPs together with a polarizer beam splitter to spatially separate the horizontally polarized subtraction mode from the travelling vertical signal wave.
More formally in this analysis we should have considered the sequential application of an unitary low reflectivity beam splitter transformation (3.7), followed by the downconverter unitary transformation (3.24) and then another unitary low reflectivity beam splitter transformation in the usual low probability regime

$$\begin{aligned} \hat{U}_{BS}(\theta_3)\ \hat{U}_{PDC}(\theta_2)\ \hat{U}_{BS}(\theta_1) &= e^{i\theta_3\left(\hat{a}_1\hat{a}_4^\dagger+\hat{a}_1^\dagger\hat{a}_4\right)}\ e^{i\theta_2\left(\hat{a}_1^\dagger\hat{a}_3^\dagger+\hat{a}_1\hat{a}_3\right)}\ e^{i\theta_1\left(\hat{a}_1\hat{a}_2^\dagger+\hat{a}_1^\dagger\hat{a}_2\right)} \\ &\approx \left[\hat{I}+i\theta_3\left(\hat{a}_1\hat{a}_4^\dagger+\hat{a}_1^\dagger\hat{a}_4\right)\right]\cdot \\ &\cdot \left[\hat{I}+i\theta_2\left(\hat{a}_1^\dagger\hat{a}_3^\dagger+\hat{a}_1\hat{a}_3\right)\right]\cdot \\ &\cdot \left[\hat{I}+i\theta_1\left(\hat{a}_1\hat{a}_2^\dagger+\hat{a}_1^\dagger\hat{a}_2\right)\right] \end{aligned} \tag{3.57}$$

where the subscript 1 refers to the signal mode target of the manipulation, and the ancillas $2, 4$ and 3 respectively to the two subtractions and to the addition. If we consider that all the three heralding modes are initially occupied by the vacuum, we can neglect the terms containing $\hat{a}_2, \hat{a}_3, \hat{a}_4$ and (3.57) becomes

$$\begin{aligned} \hat{U}_{BS}(\theta_3)\ \hat{U}_{PDC}(\theta_2)\ \hat{U}_{BS}(\theta_1) &\approx \left[\hat{I}+i\theta_3\ \hat{a}_1\hat{a}_4^\dagger\right]\cdot \\ &\cdot \left[\hat{I}+i\theta_2\ \hat{a}_1^\dagger\hat{a}_3^\dagger\right]\left[\hat{I}+i\theta_1\ \hat{a}_1\hat{a}_2^\dagger\right] \\ &\approx \hat{I}+i\theta_1\ \hat{a}_1\hat{a}_2^\dagger+i\theta_2\ \hat{a}_1^\dagger\hat{a}_3^\dagger+i\theta_3\ \hat{a}_1\hat{a}_4^\dagger- \\ &- \theta_1\,\theta_2\ \hat{a}_1\hat{a}_1^\dagger\hat{a}_2^\dagger\hat{a}_3^\dagger-\theta_1\,\theta_3\ \hat{a}_1\hat{a}_1\hat{a}_2^\dagger\hat{a}_4^\dagger- \\ &- \theta_2\,\theta_3\ \hat{a}_1^\dagger\hat{a}_1\hat{a}_3^\dagger\hat{a}_4^\dagger, \end{aligned} \tag{3.58}$$

where we neglected the third order term. The desired superposition of $\hat{a}_1^\dagger\hat{a}_1$ and $\hat{a}_1\hat{a}_1^\dagger$ can thus be obtained by making the two heralding subtraction arms 2 and 4 interfere in 50 : 50 beam splitter to erase information about their paths. The desired superposition is then heralded by an event of double photon detection, the first at one output arm of this 50 : 50 beam splitter, the second one on mode 3 announcing the single photon creation[72]

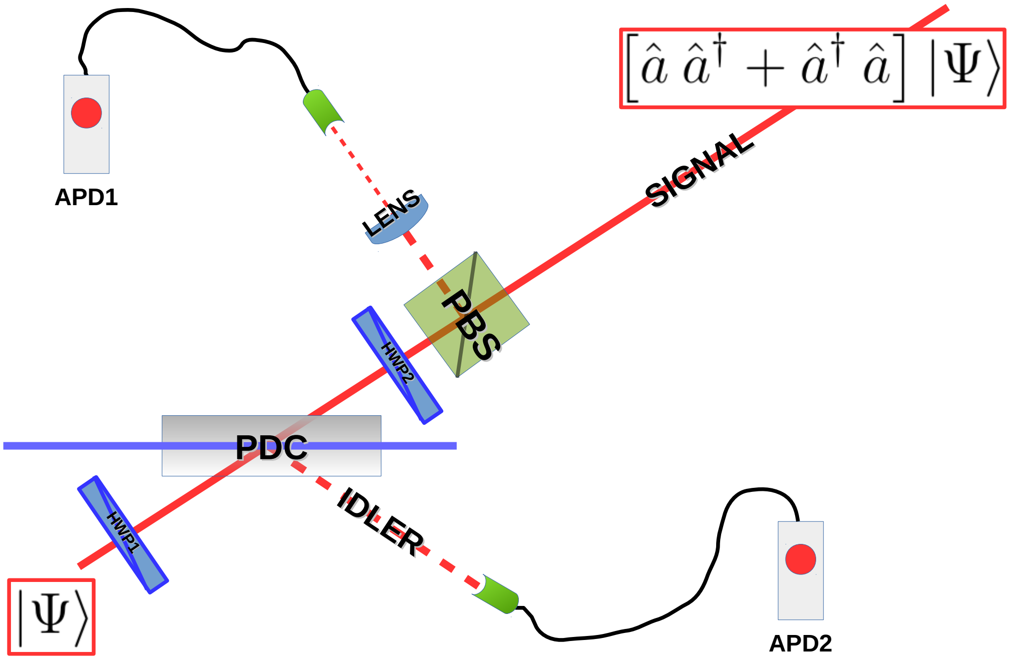

Figure 3.6: Experimental scheme for the commutator-type superposition. HWP1 and HWP2 are half wave plates. PBS is a polarizing beam splitter. APD1 heralds the delocalized subtraction by means of detection on mode 5, APD 2 instead heralds the addition of a photon in the input mode by detecting a click in mode 3 (see eq.(3.58)). The desired superposition is then produced just in case of coincident detection events.

3.3.2 Superposition of addition/identity

Interesting operations can be obtained when considering superpositions of the identity operator $\hat{I}$ and single photon creation operator $\hat{a}^{\dagger}$.

$$c_1\hat{I} + c_2 e^{i\phi}\hat{a}^{\dagger}. \tag{3.59}$$

To implement the necessary conditioned identity operator $\hat{I}$, we can imagine to inject a coherent state of light $|\beta\rangle$ aligned along the *idler* mode directly into the heralding APD, forcing it to announce the successful event even in case of no interactions, i.e. with the *signal* input state unchanged [17],[44]. In this case a perfect superposition is obtained when the mode (frequency, direction of propagation, waist, etc.) of this second beam is made identical to that of the heralding ancilla. As it is clear from Eq.(3.43), single mode addition requires strong filtering conditions on the ancilla's detection, so by using the same filtering chain, the indistinguishability can be achieved. We use an $\hat{I}$-heralding beam horizontally polarized to avoid any contribution to the type I downconversion interaction inside the BBO [8]. A polarizer (POL2 in Fig.3.7) must be inserted after the crystal in order to filter an unique polarization for the two beams (and make the ancillary photons indistinguishable in this degree of freedom). Again the relative weights c_1^2/c_2^2 and the relative phase ϕ can be experimentally selected by adjusting the relative intensities and phase of the ancillary photons announcing the two events of the superposition (see Sec.4.4.1 for an explicit analysis of the experimental parameter setting to adjust phase and weights of the superposition).

To threat mathematically this kind of superposition it should be considered the application of a coherent displacement of amplitude β on the heralding channel, i.e.

$$\begin{aligned} \hat{D}_2(\beta)\ \hat{U}_{PDC}(\theta) &\approx \hat{D}_2(\beta)\left[\hat{I}_1 - i\theta\,\hat{a}_1^{\dagger}\hat{a}_2^{\dagger}\right] \\ &= \hat{D}_2(\beta)\ \hat{I}_1 - i\theta\,\hat{a}_1^{\dagger}\,\hat{D}_2(\beta)\,\hat{a}_2^{\dagger}. \end{aligned} \tag{3.60}$$

where again we considered that initially the mode 2 is in the vacuum state.

---

[8] *Signal* and *idler* are vertically polarized while the beam heralding the identity beam is horizontally polarized when crossing the BBO crystal.

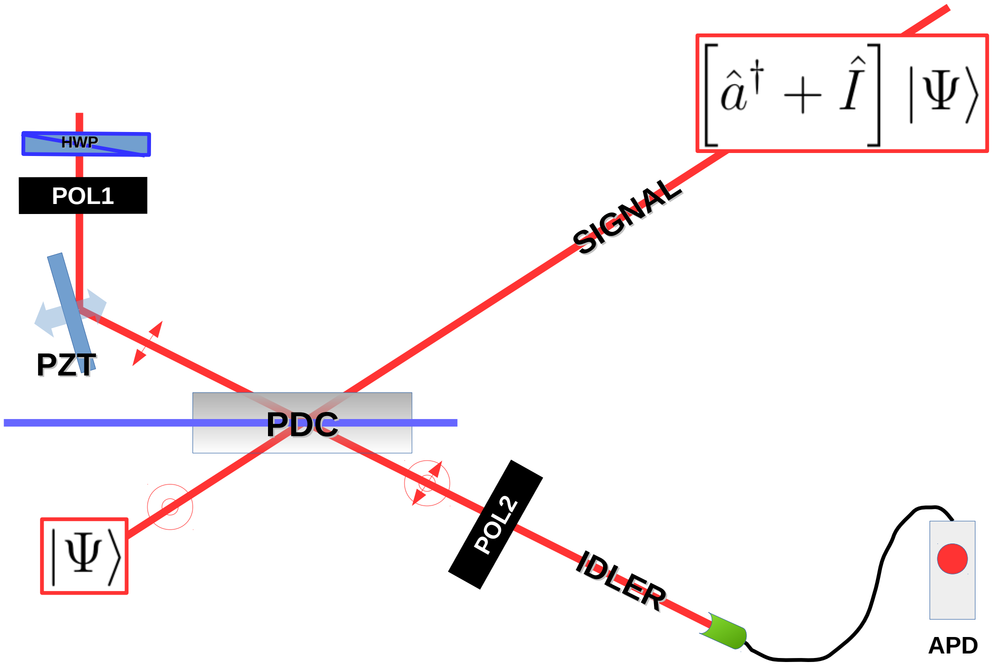

Figure 3.7: The joint action of the half wave plate HWP and the polarizer POL2 permits to select the intensity of the $\hat{I}$ ancilla and fix the weights of the superposition. PZT is a piezoelectric transducer mounted mirror used to actively lock the relative phase. The idler injected onto the crystal is horizontally polarized, the parametric down conversion emission has instead vertical polarization.

It is clear that now a click in the heralding channel 2 can also take place in case of no downconversion as well. Indeed, the detection of a photon originated in the coherent state used to displace the initial vacuum state, $\hat{D}_2\left(\beta\right)\left|0_2\right\rangle$, heralds the identity $\hat{I}_1$ on mode 1.

Chapter 4

Universal continuous-variable state orthogonalizer and qubit generator

In this chapter we will see the experimental realization of a simple universal method [11] for producing a quantum state that is orthogonal to an arbitrary, infinite-dimensional, pure input one, i.e. to generate a state $|\Psi_\perp\rangle$ from $|\Psi\rangle$, where $\langle\Psi_\perp|\Psi\rangle = 0$. The adjective universal indicates that the protocol works for all possible pure input states and, moreover, that the quality of the output state, that is the fidelity to ideal expected one, $|\Psi_\perp\rangle$ is the same for any $|\Psi\rangle$, at least in principle [19].

This simple NOT operation is commonly realized in classical binary systems, where it allows one to switch between perfectly distinct and orthogonal states denoted by 0 and 1 defining the computational basis. On the contrary, because of the superposition principle, this operation is forbidden in quantum mechanics, where a simple switch operation $\hat{S}$ acting on a qubit space as $\hat{S}|0\rangle = |1\rangle$ and $\hat{S}|1\rangle = |0\rangle$, leaves their superposition unchanged, indeed $\hat{S}(|0\rangle + |1\rangle) = |1\rangle + |0\rangle$. We will see that the formal reason for this fact is that the universal orthogonalization operation is antiunitary, i.e. it is norm-conserving but antilinear, then impossible to be deterministically realized. To overcome this problem, several alternative approaches have been developed: for instance Buzek et al. and De Martini et al. considered a NOT-gate for completely unknown polarization states of light at the price of having a non optimal output state fidelity to the ideal orthogonal one ([12], [13]), T. C. Ralph et al. and J. L. OBrien et al. designed and built a non-deterministic-measurement-based quantum controlled NOT machine in the coincidence detection basis [14],[9], etc.

Here, following the idea of Vanner et al.[11], we released the hypothesis of linearity and built a continuous variable universal orthogonalizer only dependent on a minimal information about the input state. In principle, the method can produce perfect orthogonal state at the price of non-deterministic operation. Moreover, the required preliminary information is very limited compared to a complete tomography of the input state, the approach is advantageous compared to a direct orthogonal state engineering. A similar orthogonalizer relying on minimal information about the input state required was already demonstrated for states living in a limited two-dimensional DV Hilbert space [15].

The experiment presented here shows the typical structure of quantum state engineering: an initial CV coherent state is manipulated with proper DV tools and then a quantum CV tomography is performed to characterize the output. A comparison with the ideal orthogonal state provides the definitive demonstration of the orthogonalization procedure. Again, like all along this thesis, DV and CV tools are used indifferently in a completely hybrid framework.

4.1 Quantum state orthogonalizer

An intuitive way to picture the action of the orthogonalizer can be obtained by looking at the Block sphere (or Poincaré sphere). The Block sphere is a common way to represent a 2-level quantum pure state (a qubit) on the surface of a sphere of unitary radius. The north and south poles of the sphere correspond to the two basis vectors $|1\rangle$ and $|0\rangle$ while all the other points on the surface correspond to all possible superpositions. The internal points represent mixed states. Let's indicate a point on the surface by using a coordinate system given by the two angles θ and ϕ defined as the complementary angle of the latitude with respect to the z-axis (also called colatitude) and the longitude with respect to the y-axis. In this way we can write the generic vector as

$$|\Psi\rangle = \cos\left(\frac{\theta}{2}\right)|0\rangle + e^{i\phi}\sin\left(\frac{\theta}{2}\right)|1\rangle \tag{4.1}$$

As orthogonal state vectors $|\Psi\rangle$ and $|\Psi_{\perp}\rangle$ are represented by diametrically opposite surface points[1], the desired operation should be able to map every point onto its antipodal.

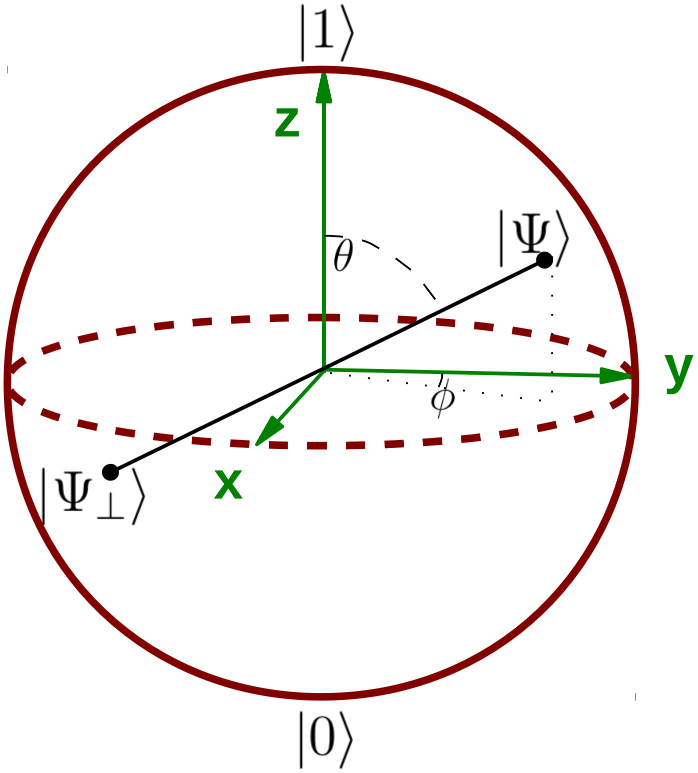

Figure 4.1: Block sphere. The north and south poles corresponds to two qubit basis vectors.

it is immediate to verify that this transformation is achieved by using the new coordinates

$$\begin{aligned} \theta &\rightarrow \pi - \theta \\ \phi &\rightarrow \pi + \phi. \end{aligned} \tag{4.2}$$

Transformation (4.2) conserves the scalar product, that is the probabil-

---

[1] That's why the orthogonalization of a single qubit is sometimes called SPIN-flip

ity[2,3], and from the Wigner theorem [16] we can assert that it must be unitary (and linear[4]) or antiunitary (and antilinear[5]). Unitary transformations are represented by the rotations of the Block sphere and it is obvious that the desired sphere inversion can't be achieved by using only rotations. Therefore the universal orthogonalization is a nonunitary operation and can't be deterministically realized.
In the same way, given an initial state $\alpha|0\rangle + \beta|1\rangle$, the antiunitary nature of the orthogonalizer operator $\hat{O}$ can be easily inferred by observing its antilinear (and then antiunitary) character

$$\hat{O}\alpha|0\rangle + \beta|1\rangle = \beta^*|0\rangle - \alpha^*|1\rangle. \tag{4.3}$$

In an infinite dimensional space, a CV orthogonalization can be easily implemented by coherently displacing the state by an arbitrary amount α'. The overlap between the displaced state and the initial state $\langle\alpha'|\hat{D}(\alpha')|\alpha\rangle$ can be indeed made arbitrary small, provided that the displacement amplitude α' is sufficiently large. Then, the operation can be considered non trivial only on

---

[2] The transition probability from the state $|\Psi\rangle = \cos\left(\frac{\theta}{2}\right)|0\rangle + e^{i\phi}\sin\left(\frac{\theta}{2}\right)|1\rangle$ to the state $|\Phi\rangle = \cos\left(\frac{\gamma}{2}\right)|0\rangle + e^{i\alpha}\sin\left(\frac{\gamma}{2}\right)|1\rangle$

$$\begin{aligned} |\langle\Phi|\Psi\rangle|^2 &= |\cos\left(\tfrac{\theta}{2}\right)\cos\left(\tfrac{\gamma}{2}\right) + e^{i(\phi-\alpha)}\sin\left(\tfrac{\theta}{2}\right)\sin\left(\tfrac{\gamma}{2}\right)|^2 \\ &= \cos^2\left(\tfrac{\theta}{2}\right)\cos^2\left(\tfrac{\gamma}{2}\right) + \sin^2\left(\tfrac{\theta}{2}\right)\sin^2\left(\tfrac{\gamma}{2}\right) + \\ &+ 2\cos\left(\tfrac{\theta}{2}\right)\cos\left(\tfrac{\gamma}{2}\right)\sin\left(\tfrac{\theta}{2}\right)\sin\left(\tfrac{\gamma}{2}\right)\cos\left(\alpha-\phi\right) \end{aligned}$$

doesn't change after the orthogonalization. Indeed, given $|\Psi'\rangle$ and $|\Phi'\rangle$ as the states $|\Psi\rangle$ and $|\Phi\rangle$ transformed by means of operation (4.2), their transition probability doesn't change because of the orthogonalization as

$$\begin{aligned} |\langle\Phi'|\Psi'\rangle|^2 &= |\cos\left(\tfrac{\pi-\theta}{2}\right)\cos\left(\tfrac{\pi-\gamma}{2}\right) + e^{i(\phi+\pi-\alpha-\pi)}\sin\left(\tfrac{\pi-\theta}{2}\right)\sin\left(\tfrac{\pi-\gamma}{2}\right)|^2 \\ &= \sin^2\left(\tfrac{\theta}{2}\right)\sin^2\left(\tfrac{\gamma}{2}\right) + \cos^2\left(\tfrac{\theta}{2}\right)\cos^2\left(\tfrac{\gamma}{2}\right) + \\ &+ 2\cos\left(\tfrac{\theta}{2}\right)\cos\left(\tfrac{\gamma}{2}\right)\sin\left(\tfrac{\theta}{2}\right)\sin\left(\tfrac{\gamma}{2}\right)\cos\left(\alpha-\phi\right) \\ &= |\langle\Phi|\Psi\rangle|^2. \end{aligned}$$

[3] In a bidimensional DV space, the scalar product-conserving feature of the orthogonalization operation is obvious.

[4] An unitary operator is always linear.

[5] An antiunitary operator is always antilinear.

case of a limited Hilbert space.
That's the reason for an alternative strategy.

4.2 Universal continuous-variable state orthogonalization strategy

Despite these fundamental limitations, as mentioned before, Vanner et al. [11] recently proposed that a perfect orthogonalizer can be in principle realized even if only some very limited preliminary information about the input state is available. They considered that, knowing the phase γ of the expectation value of the annihilation operator $\hat{a}$ on the input state $|\alpha\rangle$, i.e. $\langle\alpha|\hat{a}|\alpha\rangle = |\alpha|e^{i\gamma}$, an universal orthogonalizer can be implemented by considering the application of a superposition of single quanta creation and subtraction $\hat{X}(\theta) = \hat{a}^\dagger e^{i\theta} + \hat{a}e^{-i\theta}$, with the phase θ fixed by the condition $\theta - \gamma = \pi/2$. Indeed , i.e. $\langle\alpha|\hat{X}(\theta)|\alpha\rangle = 0$.
The proposal can be generalized as follow: given any arbitrary operator $\hat{C}$, let's assume to know its mean value $\langle\hat{C}\rangle$ for an input state $|\Psi\rangle$. Then we can define an universal CV pure state orthogonalizer $\hat{O_C}$ as

$$\hat{O_C} \equiv \hat{C} - \langle\hat{C}\rangle\hat{I} \tag{4.4}$$

where $\hat{I}$ is the identity operator. When $\hat{O_C}$ is applied onto a pure state $|\Psi\rangle$, the resulting state $|\Psi_\perp\rangle$ is orthogonal to the input one

$$\begin{aligned}\langle\Psi|\Psi_\perp\rangle &= \langle\Psi|\hat{O_C}|\Psi\rangle \\ &= \langle\Psi|\hat{C}|\Psi\rangle - \langle\hat{C}\rangle\langle\Psi|\Psi\rangle \\ &= 0. \end{aligned} \tag{4.5}$$

Eq.(4.5) is equally valid both for CV and DV pure states, independently of the dimension of the Hilbert space. Here, we propose and demonstrate the generalized orthogonalization procedure $\hat{O_C}$ to infinite dimensional, pure CV coherent states of light[6].
For mixed states, theoretical simulations show that the procedure can't be

---

[6] As already mentioned, the experimental demonstration of a DV two-dimensional state orthogonalizer requiring minimal information required can be found in [15].

anymore considered universal and the quality of the orthogonalization protocol is heavily dependent on the particular states and operator $\hat{C}$ employed (see further). In this chapter we only focused on ideally pure states of light. Moreover, although the operator $\hat{C}$ can be in principle arbitrary, the above procedure can't be applied if the input states are among its eigenstates, i.e. when $\hat{C}|\Psi\rangle = c|\Psi\rangle$. Indeed, when trying to orthogonalize an eigenstate $|\Psi\rangle$ of $\hat{C}$ one gets

$$\begin{aligned} \hat{O_C}|\Psi\rangle &= \left(\hat{C} - \langle\hat{C}\rangle\right)|\Psi\rangle \\ &= c|\Psi\rangle - c|\Psi\rangle \\ &= 0|\Psi\rangle, \end{aligned} \tag{4.6}$$

and in this case the success probability drops to zero being such a state impossible to occur. Therefore using an operator to orthogonalize one of its eigenstates is not feasible.

4.3 Universal orthogonalizer vs. complete tomography with state engineering

In principle, a full tomographic reconstruction of a given input state would allow one to design a specific setup to generate the orthogonal one. However, such a strategy would be very inefficient and far from universal. State tomography involves the measurement of observable probabilities for a large number of experimental settings, thereby requiring many identical copies of the input state for an accurate estimation after a numerical processing of the measured data sets. Furthermore, once each state is reconstructed, one should design an ad hoc experimental scheme to generate the orthogonal one, and this might in general be far from trivial.

On the contrary, even if the measurement of the mean value of operator $\hat{C}$ in our scheme ideally requires a large number of identical copies of the input state, a measure of accuracy may be found. Specifically, when there are only N copies, the estimation of the mean value is accurate by $\Delta C/\sqrt{N}$, where ΔC is the standard deviation of the measurement outcomes for the expectation value of the operator $\hat{C}$. Thus, even though we do not claim that this approach requires the least amount of resources, it is certainly much more resource efficient than those based on a full reconstruction of the state. More

importantly, a single universal experimental apparatus, only depending on a single parameter (the mean value $\langle \hat{C} \rangle$), is necessary for our scheme to orthogonalize arbitrary states. In the particular case of a set of input states for which $\langle \hat{C} \rangle$ is the same, no change at all is needed in the apparatus to process all the elements of the set.
The orthogonalizer is general enough to work based on any operator $\langle \hat{C} \rangle$ and with any pure input state $|\Psi\rangle$. Choosing a particular operator implies designing the experimental setup accordingly, but a specific apparatus would then work for arbitrary input states, with the proper adjustment of its parameters.

4.4 Experimental implementations

To demonstrate the functioning of the above method and its generality, in the following the experimental analysis of specific examples based on two different $\hat{C}$ operators (therefore implying two completely different experimental setups) is presented. The first tested version is based on the DV single photon creation operator $\hat{a}^\dagger$, the second on the DV photon number $\hat{n}$. In both cases, a CV coherent state $|\alpha\rangle$ has been used as the input state to orthogonalize.

4.4.1 Single-photon creation version

The operator

A particularly versatile version of (4.5) is obtained when $\hat{C} = \hat{a}^\dagger$, which has no eigenstates and can thus succeed in orthogonalizing any pure input state. In this case the operator takes the particular form

$$\hat{O_{a^\dagger}} = \hat{a}^\dagger - \langle \hat{a}^\dagger \rangle \hat{I}. \tag{4.7}$$

with $\hat{I}$ identity operator. It is then easy to see that, when applied to a coherent state $|\alpha\rangle$, Eq.(4.7) becomes

$$\hat{O_{a^\dagger}} = \hat{a}^\dagger - \alpha^* \hat{I}. \tag{4.8}$$

Keeping in mind that a coherent state can be written as a displaced vacuum state ($\hat{D}(\alpha)|0\rangle$), one finds that the output state is a displaced single photon:

$$\begin{aligned}\left(\hat{a}^\dagger - \alpha^* \hat{I}\right) \hat{D}(\alpha)|0\rangle &= \hat{a}^\dagger \hat{D}(\alpha)|0\rangle - \alpha^* \hat{D}(\alpha)|0\rangle \\ &= \left(\hat{D}(\alpha)\hat{a}^\dagger + \alpha^* \hat{D}(\alpha)\right)|0\rangle - \alpha^* \hat{D}(\alpha)|0\rangle \\ &= \hat{D}(\alpha)\hat{a}^\dagger|0\rangle \\ &= \hat{D}(\alpha)|1\rangle, \end{aligned} \tag{4.9}$$

which is clearly orthogonal to $|\alpha\rangle$.
Note that we do not assume any knowledge about the initial state except its amplitude. Thus, simply choosing another coherent state $|\alpha'\rangle$ as the orthogonal one is not a valid alternative. In any case, the overlap of two coherent states

$$|\langle\alpha'|\alpha\rangle|^2 = e^{-|\alpha'-\alpha|^2} \tag{4.10}$$

is never zero, especially in a regime of low intensities.

Experimental implementation

Preparation of the initial state In this experiment the mode-locked Ti:sapphire laser emitting a train of 786 nm picosecond pulses at a repetition rate of 80 MHz has been used for producing the input coherent states $|\alpha\rangle$, the ancillary beam $|\beta\rangle$ (see further) and, after frequency doubling to 393 nm in a lithium triborate (LBO) crystal, as the pump for degenerate, non-collinear, parametric down-conversion in a 3-mm long β-barium borate (BBO) crystal.

Manipulation In Fig.4.2 it is shown a simplified scheme of the experimental setup designed to manipulate the initial state and realize the operation (4.8). The scheme is basically a conditioned implementation of the two operators $\hat{a}^\dagger$ and $\hat{I}$ where the photons heralding both the operations are made indistinguishable (see section 3.3). In such a way, the information about the origin of a click in the heralding detector is erased and it is fundamentally indeterminable (by the SPCM click) which of the two events has occurred. Only in this case a superposition of $\hat{a}^\dagger$ and $\hat{I}$ can be obtained.
In particular, the photon creation operator can be conditionally realized by means of stimulated type-I parametric down-conversion (PDC) in a nonlinear crystal synchronously seeded by the vertically polarized (ideally) pure

coherent state $|\alpha\rangle$ along the signal mode [7],[18]. Heralded photon addition in such a mode is conditioned on a single photon detection by the avalanche photodiode (SPCM) placed in the idler mode after narrow spectral and spatial filters (F) (see Sec.3.2).
For the conditioned implementation of the identity operator $\hat{I}$, we have to make sure that no PDC interaction takes place into the crystal when the cor responding heralding photon is detected[7]. Considering that we are working in a very low gain regime where PDC is an extremely rare process, identity can be faithfully implemented by just injecting an ancillary coherent state $|\beta\rangle$ along the PDC idler mode and detecting one of these photons.
The coherent superposition of photon addition and the identity can be then realized by mixing the vertically polarized (heralding) idler PDC mode with the horizontally polarized coherent light field $|\beta\rangle$ injected along the same direction. Indeed, if an unique polarization is selected by means of a polarizer and the optical modes of the two beams are matched spatially and temporally by using the same filtering chain, every difference in the beams is erased and the beams can be thus considered indistinguishable. As a result, the origin of the heralding photons detected by the SPCM is fundamentally indeterminable and a superposition of $\hat{a}^{\dagger}$ and $\hat{I}$ must be considered (see Sec.3.3.2).

Similar techniques, involving phase-space displacement on the heralding mode of conditional state generation, have been recently used for quantum state engineering up to two photons [17],[44].

Weights and phase adjustment To implement the desired superposition of eq.(4.8) we need to experimentally control both the relative phase and the weights of the photon addition and identity. Before seeing how this can be achieved, it can be helpful to choose a reference system where the complex amplitude α is real.
Let's take a look at the desired state

$$\begin{aligned} |\alpha_{\perp}\rangle &= \left(\hat{a}^{\dagger} - \alpha\hat{I}\right)|\alpha\rangle \\ &= \left(\tfrac{\sqrt{1+\alpha^2}}{\sqrt{1+\alpha^2}}\hat{a}^{\dagger} - \alpha\hat{I}\right)|\alpha\rangle \\ &= \sqrt{1+\alpha^2}|\alpha,1\rangle - \alpha|\alpha\rangle, \end{aligned} \tag{4.11}$$

---

[7] And the injected signal beam $|\alpha\rangle$ then will pass through the crystal unaffected.

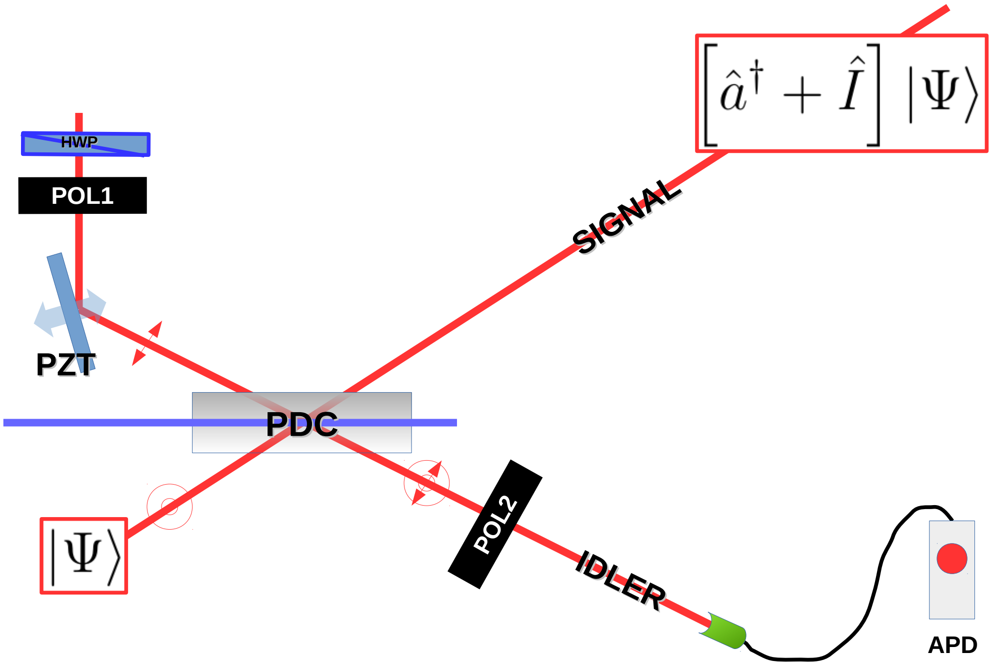

Figure 4.2: Conceptual experimental scheme of the orthogonalizer based on photon addition by heralded stimulated PDC. The photon addition is implemented by heralded type-I parametric down conversion (PDC), stimulated by the vertically polarized coherent state $|\alpha\rangle$ injected along the signal mode. The horizontally-polarized beam injected along the idler mode doesn't contribute to stimulated emission, nor it interferes with the vertically-polarized seed $|\alpha\rangle$ coherent pulses injected along the signal mode, because of the type-I interaction. A click in the single-photon-counting module (SPCM) normally heralds a single photon addition to the generic input state $|\Psi\rangle$. However, if the PDC vertically polarized idler mode is mixed with a synchronized horizontally polarized coherent state $|\beta\rangle$ with the use of the polarizator P prior the detection, a superposition of $\hat{a}^\dagger$ and $\hat{I}$ can be obtained. Slightly rotating the polarizer and using a piezoelectric transducer phase shifter (θ) enables the adjustment of weights and phase of the superposition (see further). The scheme is basically identical to the one shown in Sec.3.3.2.

where we have introduced the normalized state $|\alpha, 1\rangle = \frac{\hat{a}\dagger}{\sqrt{1+\alpha^2}}|\alpha\rangle$ called SPACS, acronym for single photon added coherent state[8]. The coefficients $\sqrt{1+\alpha^2}$ and $-\alpha$ must be interpreted as the probability amplitudes for $\hat{a}^\dagger$ and $\hat{I}$ to occur and their squared modulus represents the corresponding probabilities $Pr_{a^\dagger}$ and Pr_I

$$\frac{Pr_{a^\dagger}}{Pr_I} = \frac{1+\alpha^2}{\alpha^2} \tag{4.12}$$

The normalization factor $\sqrt{1+\alpha^2}$ represents the enhancement ratio of the downconversion probability for the stimulated signal with respect to the spontaneous case (i.e. when $\alpha = 0$), see [18].
From the experimental point of view, these probabilities are proportional to the SPCM clicks count rate due respectively to photons originated from the PDC process (CR_{PDC}), and those injected as ancillary beam $|\beta\rangle$ (CR_{anc}). We must pay attention to take into account the unavoidable contribution of clicks from spontaneous emission (CR_{SPDC}), because it does not contribute to Pr_I and thus must be subtracted from the ancillary counts (CR_{anc})

$$\begin{aligned} Pr_{a^\dagger} &\propto CR_{PDC} = CR_{SPDC}(1+\alpha^2) \\ Pr_I &\propto CR_{anc} - CR_{SPDC}. \end{aligned} \tag{4.13}$$

By putting together eq. (4.12) and (4.13) we find

$$\frac{1+\alpha^2}{\alpha^2} = \frac{CR_{SPDC}(1+\alpha^2)}{CR_{anc} - CR_{SPDC}} \tag{4.14}$$

and so

$$\begin{aligned} CR_{anc} &= CR_{SPDC}(1+\alpha^2)\frac{\alpha^2}{1+\alpha^2} + CR_{SPDC} \\ &= CR_{SPDC}\left(\alpha^2 + 1\right) \\ &= CR_{PDC} \end{aligned} \tag{4.15}$$

---

[8] See [7] and [20] for more details about SPACS

Eq. (4.15) states that for perfect orthogonalization we have to balance exactly the count rates of SPCM clicks due to the PDC to the ones due to the ancillary photons injected. To meet this condition we measured the number of clicks due to the $|\alpha\rangle$-stimulated emission without the injection of the ancilla $|\beta\rangle$, and compared it to the value observed in the opposite condition of ancilla $|\beta\rangle$ with no seeding $|\alpha\rangle$. By selecting properly the polarization component transmitted by the polarizer P, the condition (4.15) has been experimentally fulfilled.
A second condition requires to fix the relative phase ϕ to π. This has been done by using the count rate of the heralding SPCM to measure the interference between the PDC idler and the synchronized coherent state $|\beta\rangle$. By using the observed value as a feedback signal, it has been possible to actively lock the interference fringe to its minimum value (corresponding to a relative phase of π) with a mirror mounted on a piezoelectric transducer (PZT) in the path of the ancilla.
By simply controlling both the relative phase and the probabilities of the two operations, different superpositions of $\hat{a}^\dagger$ and $\hat{I}$ can be obtained, in particular those corresponding to the orthogonalizer.

Detection The conditionally generated output state is finally analyzed by means of a high-frequency, time-domain homodyne detector (BHD) [21] triggered by the coincidences between the idler SPCM clicks and the electronic signal from the mode-locking driver to reduce the dark counts of the avalanche photodiode.
A full quantum tomographic reconstruction of the density matrix of the states is finally performed, based on an iterative, maximum-likelihood algorithm (see Appendix B).

The results

Figure 4.3 illustrates the result (with no detection inefficiency correction) of the application of the orthogonalizer to coherent states of different initial amplitudes. The x quadrature distributions show that the Wigner functions of the orthogonal states are differently displaced versions of a single-photon Wigner function [10]. A full tomography of the input and output states for the case with $\alpha = 1.0$ results in a mutual fidelity of 0.4. The discrepancy from an ideal value of zero comes from different sources of experimental imperfections that limit the purity of the prepared and measured states and,

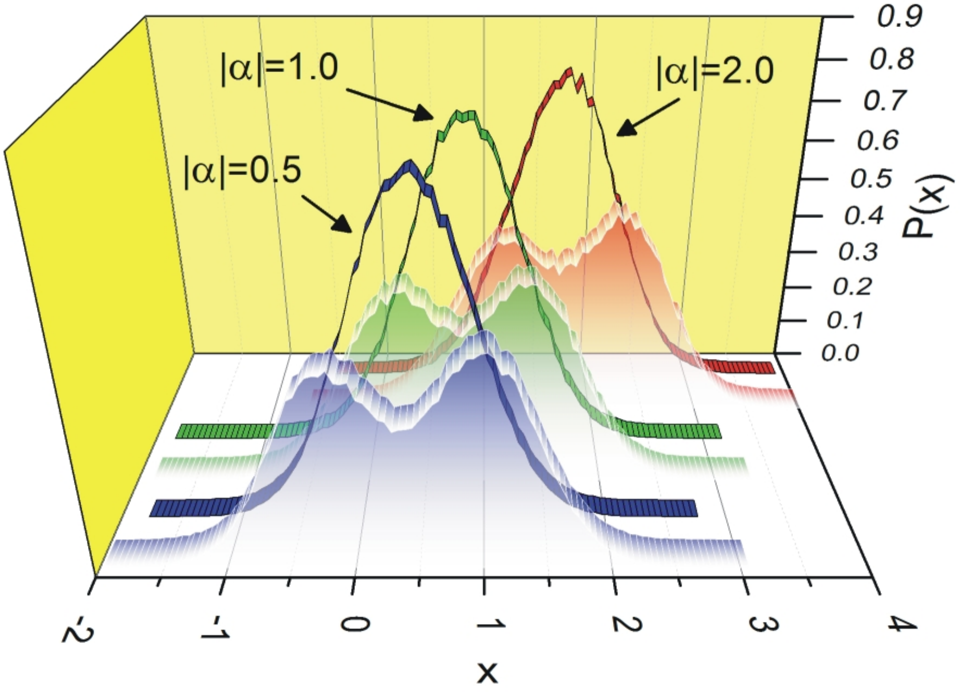

Figure 4.3: Raw measured x quadrature distributions (marginals of the Wigner function) for the input coherent states (ribbon-style curves) and for the corresponding results of the orthogonalization procedure (shaded areas) with $\alpha = 0.5, 1.0, 2.0$.

as a consequence, their orthogonality (see further).

4.4.2 Photon number version

The operator In order to demonstrate the effectiveness and generality of the proposed approach, we now consider another scheme to realize the orthogonalizer. Since the mean number of photons in a state is a parameter often easy to determine experimentally, one may insert such a mean photon number $\langle \hat{n} \rangle$, with $\hat{n} = \hat{a}^\dagger \hat{a}$, into the definition of the orthogonalizer

$$\begin{aligned} \hat{O}_n &\equiv \hat{n} - \langle \hat{n} \rangle \hat{I} \\ &= \hat{a}^\dagger \hat{a} - \langle \hat{a}^\dagger \hat{a} \rangle \hat{I} \end{aligned} \tag{4.16}$$

Eq.(4.16) can be rewritten in a more convenient form by exploiting the bosonic commutation rule. Indeed, from $\left[\hat{a}, \hat{a}^\dagger\right] = \hat{I}$ it follows that the general superposition $c_1 \hat{a}^\dagger \hat{a} + c_2 \hat{I}$ can be transformed as

$$\begin{aligned} A\hat{a}^\dagger \hat{a} + B\hat{a}\hat{a}^\dagger &= A\hat{a}^\dagger \hat{a} + B\left(\hat{I} + \hat{a}^\dagger \hat{a}\right) \\ &= (A + B)\,\hat{a}^\dagger \hat{a} + B\hat{I} \end{aligned} \tag{4.17}$$

experimentally testable with a setup similar to the one first developed for testing the bosonic commutation relation [2] (see Sec.3.3.1).
Therefore, a state orthogonal to a generic one of mean photon number $\langle \hat{n} \rangle$ can be straightforwardly obtained by adjusting the free parameters so that

$$\frac{B}{A+B} = -\langle \hat{n} \rangle. \tag{4.18}$$

that is

$$\frac{B}{A} = -\frac{\langle \hat{n} \rangle}{\langle \hat{n} \rangle + 1}. \tag{4.19}$$

It is seen that, when used in combination to an input coherent state $|\alpha\rangle$, this scheme results in the same orthogonal state as for the previous example, since

$$\begin{aligned} \left[\hat{n} - \langle \hat{n} \rangle \hat{I}\right] |\alpha\rangle &= \left[\hat{a}^\dagger \hat{a} - \langle \hat{n} \rangle \hat{I}\right] |\alpha\rangle \\ &= \left[\alpha \hat{a}^\dagger - \langle \hat{n} \rangle \hat{I}\right] |\alpha\rangle. \end{aligned} \tag{4.20}$$

Note that again we do not assume any knowledge about the initial state except its mean photon number.

Experimental implementation

Preparation of the initial state In this second version of the orthogonalizer we considered the same ideally pure coherent state $|\alpha\rangle$ as input. Consequently, the preparation part is identical to the one described for the photon creation version: same mode-locked Ti:sapphire laser, same frequency doubling lithium triborate (LBO) crystal, ecc.

Manipulation The operation (4.17) can be implemented with a scheme basically similar to the one used for bosonic commutation relation. It relies on the coherent superposition of two inverted sequences of photon creation and annihilation operators by means of two 5 deg rotated half wave plates, each ensuring a photon subtraction probability of $\approx 3\%$ (see 3.3 and 3.1).
A double-click coincidence pattern from two single-photon detectors, one at the output of the polarizing beam-splitter used to collect the horizontally polarized subtraction mode, and the other on the herald mode of the photon addition stage placed between the two subtraction ones, certifies that a sequence of photon addition and subtraction has certainly taken place, but leaves their order unknown. By adjusting the two half wave plates rotation angle and the relative phase between the two subtraction heralding modes, a generic superposition of the two sequences like eq.(4.17) can thus be realized.

Weights and phase adjustment The relative weights between the two inverted sequences of operations is then properly adjusted according to the mean photon number of the input states, according to the condition (4.18). Like in the photon addition version, in order to connect the superposition weights to the APD clicks, it is helpful to rewrite eq.(4.16) considering normalized states in the superposition. Let's start calculating the two norms

$$\begin{aligned}\mathcal{N}_1 &= \left[\langle\alpha|\hat{a}^\dagger\hat{a}\hat{a}^\dagger\hat{a}\,|\alpha\rangle\right]^{1/2}\\ &= \left[|\alpha|^2\,\langle\alpha|\hat{a}\hat{a}^\dagger\,|\alpha\rangle\right]^{1/2}\\ &= \left[|\alpha|^2+|\alpha|^4\right]^{1/2} \qquad (4.21)\end{aligned}$$

$$\begin{aligned}\mathcal{N}_2 &= \left[\langle\alpha|\hat{a}\hat{a}^\dagger\hat{a}\hat{a}^\dagger\,|\alpha\rangle\right]^{1/2} \\ &= \left[\langle\alpha|\left(\hat{I}+\hat{a}^\dagger\hat{a}\right)\left(\hat{I}+\hat{a}^\dagger\hat{a}\right)\,|\alpha\rangle\right]^{1/2} \\ &= \left[\langle\alpha|\left(\hat{I}+\alpha^*\hat{a}\right)\left(\hat{I}+\hat{a}^\dagger\alpha\right)\,|\alpha\rangle\right]^{1/2} \\ &= \left[1+3|\alpha|^2+|\alpha|^4\right]^{1/2} \qquad (4.22)\end{aligned}$$

We can now rewrite the superposition of Eq.(4.17) for an input coherent state $|\alpha\rangle$ as

$$\left[A\hat{a}^\dagger\hat{a}+B\hat{a}\hat{a}^\dagger\right]|\alpha\rangle \;=\; A\mathcal{N}_1\frac{\hat{a}^\dagger\hat{a}}{\mathcal{N}_1}|\alpha\rangle + B\mathcal{N}_2\frac{\hat{a}\hat{a}^\dagger}{\mathcal{N}_2}|\alpha\rangle \qquad (4.23)$$

and connect the coefficients to the APD clicks

$$\left|\frac{A\,\mathcal{N}_1}{B\,\mathcal{N}_2}\right|^2 = \frac{CR_{aa^\dagger}}{CR_{a^\dagger a}}. \qquad (4.24)$$

where again $CR_{aa^\dagger}$ represents the count rate observed for the successful event of single photon subtraction and addition, with $CR_{a^\dagger a}$ for the successful event of single photon addition and subtraction.
By using the orthogonalization condition (4.19) and substituting the values found in Eqs.(4.21),(4.22) we obtain the condition for the counts

$$\frac{CR_{aa^\dagger}}{CR_{a^\dagger a}}(\alpha) = \frac{1+3|\alpha|^2+|\alpha|^4}{|\alpha|^2+|\alpha|^4}\;\left(\frac{|\alpha|^2+1}{|\alpha|^2}\right)^2. \qquad (4.25)$$

So, we see that the orthogonalization condition depends on the amplitude α.
Experimentally the parameter α is accessible by a simple measure of the factor $1+|\alpha|^2$, as the enhancement factor of the downconversion rate in the stimulated with respect to the spontaneous cases. The right ratio of Eq.(4.25) can be then adjusted for each input $|\alpha\rangle$ by adjusting the two half wave plates. The relative phase in the superposition has been fixed to π by inserting an additional birefringent crystal (see Appendix C) between the two subtraction HWPs. A slight tilt of the crystal permitted to change the optical length of the horizontally polarization component between the two half wave plates until a minimum of interference was observed in the subtraction detector.

Detection See 4.4.1.

Results

Figure 4.4 shows the reconstructed Wigner functions for input and orthogonal output states, whose measured mutual fidelity (B.19) is $\mathcal{F} = 0.34$, while the fidelities $\mathcal{F}_c$ to an ideal coherent state $|\alpha = 0.78\rangle$ are 0.96 and 0.18, respectively.

4.5 Universal CV qubit generator

In addition to the CV orthogonalizer, this technique also naturally leads to a method for producing arbitrary coherent superpositions of orthogonal quantum states out of any input pure one. For any complex number c, the (unnormalized) superposition

$$\begin{aligned} c|\Psi\rangle + |\Psi_\perp\rangle &= \left(c\hat{I} + \mathcal{N}\hat{O}_C\right)|\Psi\rangle \\ &= \left[\mathcal{N}\hat{C} + \left(c - \mathcal{N}\langle\hat{C}\rangle\right)\hat{I}\right]|\Psi\rangle \end{aligned} \tag{4.26}$$

is realized by applying the same operation of Eq.(4.5) to the input state, but with an appropriate change in the weight of the identity operator. Therefore, once the orthogonalizer is in operation, any quantum superposition of $|\Psi\rangle$ and $|\Psi_\perp\rangle$, which constitutes a general arbitrary CV qubit, can also be straightforwardly realized.

4.6 Experimental implementation

We demonstrated the feasibility of the Universal CV Qubit Generator of Eq.(4.26) by using the same $\hat{a}^\dagger$-based experimental scheme used for the Universal CV orthogonalizer. Indeed, a simple adjustment of the coherent state $|\beta\rangle$ intensity and phase allows one to produce various CV qubit states.
We want to test the procedure by producing balanced superpositions, i.e. equal-weight superposition states, of a coherent state $|\alpha\rangle$ and its orthogonal counterpart, that is

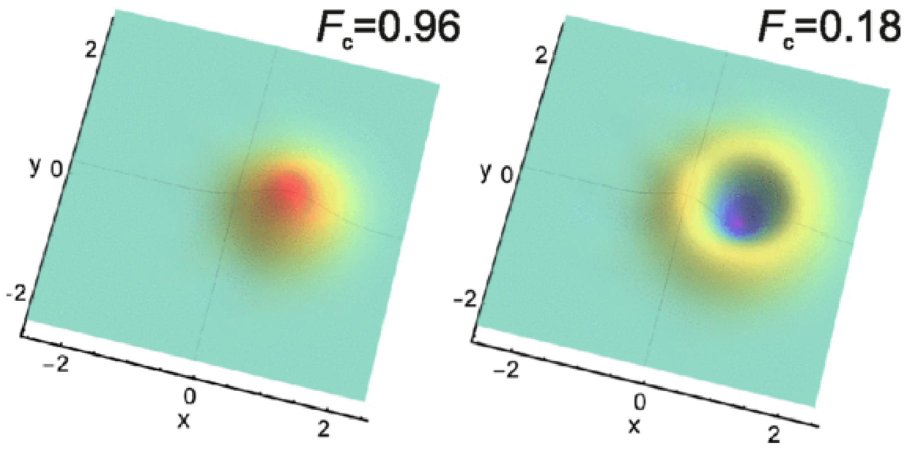

Figure 4.4: Wigner functions of the input coherent state and of its orthogonal (a displaced single-photon Fock state) as reconstructed from the homodyne data after correcting for the limited (70%) detection efficiency.

$$
\begin{aligned}
\frac{1}{\sqrt{2}}\left[e^{i\phi}|\alpha\rangle+|\alpha_{\perp}\rangle\right] &= \frac{1}{\sqrt{2}}\left[e^{i\phi}\hat{I}+\left(\hat{a}^{\dagger}-\langle\hat{a}^{\dagger}\rangle\hat{I}\right)\right]|\alpha\rangle \\
&= \frac{1}{\sqrt{2}}\left[\hat{a}^{\dagger}+\left(e^{i\phi}-\alpha\right)\hat{I}\right]|\alpha\rangle \\
&= \frac{1}{\sqrt{2}}\left[\sqrt{1+|\alpha|^2}|\alpha,1\rangle+\left(e^{i\phi}-\alpha\right)\hat{I}|\alpha\rangle\right]
\end{aligned} \tag{4.27}
$$

for the phases $\phi = 0, \pi/2, \pi, -\pi/2$
Let's now see how to set the experimental parameters to get the balanced superposition for the $\phi = 0$ case, that is $1/\sqrt{2}\left[\sqrt{1+|\alpha|^2}|\alpha,1\rangle+(1-\alpha)\,\hat{I}|\alpha\rangle\right]$. Let's consider the same notation of the Eq.(4.12). Then we get

$$
\frac{Pr_{a^{\dagger}}}{Pr_{I}}=\frac{1+\alpha^2}{|1-\alpha|^2} \tag{4.28}
$$

and from Eq.(4.13)

$$
\begin{aligned}
CR_{anc}-CR_{SPDC} &= CR_{a^{\dagger}}\,\frac{|1-\alpha|^2}{1+\alpha^2} \\
&= CR_{SPDC}\,\left(1+\alpha^2\right)\frac{|1-\alpha|^2}{1+\alpha^2}.
\end{aligned} \tag{4.29}
$$

Since we are interested in implementing the superposition for the particular case $\alpha = 1$, we see that it must be $CR_{anc} - CR_{SPDC} = 0$. This means that we don't need to inject any ancillary coherent state $|\beta\rangle$.
Of course in this particular case there's no need to actively lock any phase. From Eq.(4.27) in the particular case $\phi = 0$ and $\alpha = 1$ we indeed see that the desired superposition is just a photon added coherent state (SPACS) [7],[20]. In Fig. 4.5 we show the measured Wigner functions for different equal-weight superposition states of an input coherent state with $|\alpha| = 1.0$ and its orthogonal state. In the different plots, the phase of the resulting CV qubit is simply varied by properly controlling the relative phase between the two ancillary modes. The fidelities of the reconstructed states to the ideal superpositions of $|\alpha\rangle$ and $|\alpha_{\perp}\rangle$ are all quite large, of the order of 90%.

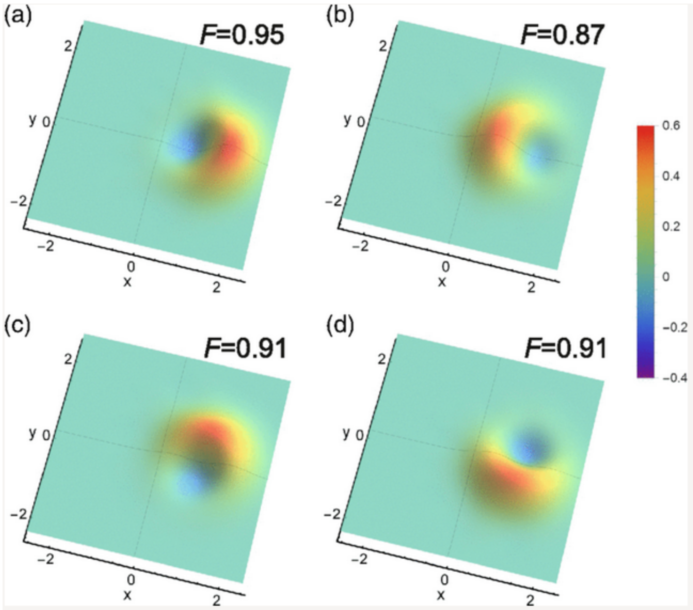

Figure 4.5: Wigner functions for different balanced superpositions of states $|\alpha\rangle$ and $|\alpha_\perp\rangle$ with $|\alpha| = 1.0$, as reconstructed by correcting for a detection efficiency of 70%. Panels (a) and (b) correspond to states $\sqrt{1/2}(|\alpha\rangle \pm |\alpha_\perp\rangle)$ and panels (c) and (d) correspond to states $\sqrt{1/2}(|\alpha\rangle \pm i|\alpha_\perp\rangle)$, respectively. The experimental fidelities $\mathcal{F}$ of the generated states to the ideal CV superpositions are also shown. Different values of $\mathcal{F}$ are mainly connected to the different levels of stability in the experimental superposition phase for the different states.

4.7 Extension of the formalism to mixed states and lack of universality

The quantum state orthogonalizer of Eq.(4.5) relies on the condition $\langle\Psi|\hat{O}_C|\Psi\rangle = 0$, which is valid for pure states only. However, this can be formally extended to the case of mixed input $\hat{\rho}$, so that the orthogonal states would be given by:

$$\hat{\rho}_{\perp} = \hat{O}_C^{\dagger}\hat{\rho}\hat{O}_C \tag{4.30}$$

where the orthogonalizer operator is defined as:

$$\hat{O}_C = \hat{C} - Tr[\hat{C}\hat{\rho}]\hat{I} \tag{4.31}$$

Following this approach, it is possible to verify how the fidelity between initial and orthogonal states $F(\hat{\rho}, \hat{\rho}_{\perp})$ is affected by an impure input one. For instance, we have simulated a mixed coherent state with $\alpha = 1.0$ and a purity of 0.85, obtained by applying some phase noise. In this case, the fidelity between the phase-diffused input coherent state and the orthogonal output resulting from Eq.(4.30) is 0.08 and 0.25 for $\hat{C} = \hat{a}^{\dagger}$ and $\hat{C} = \hat{n}$, respectively, and the protocol can't be anymore considered as universal.
The result of the orthogonalization protocol is heavily dependent on the particular states and operators employed. Although it does not generally work for mixed states, it is easy to see that some particular forms of mixed states can be perfectly orthogonalized with the right choice of the $\hat{C}$ operator. For example, the orthogonalizer relying on the creation operator $\hat{a}^{\dagger}$ realizes a perfect orthogonalization of mixtures of squeezed vacuum states obtained by adding arbitrary amounts of phase noise.
A general orthogonalizer form for mixed states would require one to find, if it exists, and for any given input state $\hat{\rho}$, an operator $\hat{O}_C$ that, depending on some preliminary information on $\hat{\rho}$, satisfies the condition $F(\hat{\rho}, \hat{\rho}_{\perp}) = 0$. It is beyond the scope of this work to extend the discussion to such a general situation.

4.8 Effects of experimental imperfections on state orthogonalization and detection

Several experimental factors limit the generation and detection of perfectly orthogonal states to a given input one. Since our experimental realization relies on weak input coherent states generated by our pulsed laser source, it is reasonable to assume them as pure ones. On the contrary, in the following we will model all the experimental imperfections as deriving from both the orthogonal state preparation, via the imperfect implementation of the operator $\hat{O}_C$ and from the measurement processes.
First of all, we consider the effect of the limited accuracy in the estimation of the mean value of the operator $\hat{C}$, by introducing an error ϵ in the realization of the orthogonalization operator:

$$\hat{O}_{C_\epsilon} = \mathcal{N}\left(\hat{C} - (1 \pm \epsilon)\,\langle\hat{C}\rangle\right), \tag{4.32}$$

where $\mathcal{N}$ is a normalization factor. The effect of the error ϵ for input coherent states $|\alpha\rangle$ can be found analytically and results in the fidelity:

$$F(|\alpha\rangle\langle\alpha|, \hat{O}_{C_\epsilon}|\alpha\rangle\langle\alpha|\hat{O}^\dagger_{C_\epsilon}) = \frac{\epsilon^2\alpha}{1+\epsilon^2\alpha^2} \tag{4.33}$$

where the same expression is valid for both operators $\hat{a}^\dagger$ and $\hat{n}$. A 10% error in the estimation of the operator mean value has a very small effect on the final fidelity between the input and output states. From an ideal zero fidelity, this relatively large error only results in a very slight overlap ($F = 0.01$) for an input coherent state of amplitude $\alpha = 1$.

A more important source of non-ideal experimental results comes from imperfections in the protocol for the conditional preparation of the states, which limit their purity. This factor alone puts an upper limit to the minimum overlap achievable between experimental orthogonal states, even if the contribution of the limited detection efficiency of the homodyne setup (estimated about 70% in the present measurements) is taken into account in the tomographic reconstructions. For example, we can refer to the specific case of the state generated in the experiment when feeding coherent states into the $\hat{O}_n$ orthogonalizer and presented in Fig.4.4. While the theoretical fidelity between a coherent state $|\alpha\rangle$ and its orthogonal is indeed 0, the impurities connected to imperfect photon addition and subtraction are sufficient to produce a mixture of the desired orthogonal state with about 10% of the input coherent one, thus causing a corresponding increase in their mutual fidelity. Other sources of experimental imperfections further degrade the final states: unavoidable drifts in the input coherent state amplitude α and instabilities in the phase lock during long acquisition runs may move the experimental setup away from the strict phase and amplitude relationships necessary for the implementation of the correct operator superpositions in the expression for $\hat{O}_n$.

Moreover, residual fluctuations of the relative phase between the produced states and the homodyne local oscillator around the nominal set values are also seen to contribute to the degradation of both the experimentally reconstructed input coherent state and output orthogonal one.

To be more specific, the model we used is based on the density operator of the prepared state, which can be written as:

$$\rho_p(\alpha, \phi) = \eta_p \rho_\perp(\alpha, \phi) + (1 - \eta_p)|\alpha\rangle\langle\alpha| \tag{4.34}$$

where $\rho_\perp(\alpha, \phi) = \hat{O}|\alpha\rangle\langle\alpha|\hat{O}$ is the orthogonal state obtained by applying the orthogonalization operator $\hat{n} - e^{i\phi}\langle\alpha_0|\hat{n}|\alpha_0\rangle\hat{I}$ to the coherent state $|\alpha\rangle$. The orthogonalizer setup is prepared for the nominal value of $\alpha_0 = 0.78$, and the superposition phase ϕ is introduced in order to account for the setup phase instability. The preparation efficiency η_p (Eq.(3.51)), keeping into account both the limited spatial-temporal filtering along the trigger channel and the dark counts of the SPCM detectors, is estimated to be $\eta_p = 0.9$. In order to model the effect of the local oscillator phase instability we also allow rotations of the state $\rho_\perp(\alpha, \phi)$ by a phase θ.

The full model state is finally given by:

$$\rho_{model} = \int d\theta\, d\phi\, d\alpha\; g(\alpha - \alpha_0, \sigma_\alpha)\; g(\phi, \sigma_\phi)\; g(\theta, \sigma_\theta)\; \hat{U}(\theta)\rho_p(\alpha, \phi)\hat{U}^\dagger(\theta) \tag{4.35}$$

where $g(x, \sigma) = e^{-x^2/2\sigma^2}/\sqrt{2\pi}\sigma$ and $\hat{U}(\theta) = e^{i\theta\hat{n}}$ is the phase shifting operator. The values for the parameter standard deviations used in the simulations were $\sigma_\alpha = 0.15, \sigma_\phi = 0.19, \sigma_\theta = 0.15$.

By theoretically modelling the effect of both the preparation-related mixedness and of the above phase/amplitude instabilities, we were able to effectively simulate the observed experimental states with fidelities of 0.998 (between measured and simulated coherent states) and 0.97 (between measured and simulated orthogonal states). For the coherent states, the simulated and measured state purities are identical at 0.92. For the orthogonal states they differ only slightly, with the simulated state having a purity of 0.62 compared to 0.65 for the measured state.

The low purity of the experimental states following orthogonalization explains the measured residual fidelity of 0.18 observed between the experimental orthogonal state of Fig.4.4 (right panel) and the ideal coherent state $|\alpha_0 = 0.78\rangle$, as well as the similar overlap of 0.17 for the simulated orthogonal state. The amplitude drifts and phase fluctuations during the long acquisitions are also responsible for the less-than-perfect fidelity of 0.96 between such an ideal coherent state and the experimentally-reconstructed one (left panel of Fig.4.4). The reduced purities also explain the lower fidelity of 0.76 for both of the simulated and measured orthogonal states relative to the ideal orthogonal one. Finally, the combined effect of impurities in both the experimental coherent state and its orthogonalized version results in a mutual fidelity between the nominally orthogonal experimental states of 0.34, in agreement with the one expected from the model.

Chapter 5

Measurement-induced strong Kerr nonlinearity for weak quantum states of light

Nonlinear optical interactions represent a major tool for generation and manipulation of optical fields in both classical and quantum domains, and they form a basis of countless photonics devices. However, the envisioned applications of nonlinear interactions in quantum optics and optical quantum information processing often require strong nonlinear coupling between single photons which is not readily available, because the typical nonlinearities of common non-resonant optical media are many orders of magnitude weaker than what is required to achieve an appreciable nonlinearity at the single-photon level. Despite years of intensive experimental and theoretical efforts, and using specially tailored media with enhanced nonlinearities such as clouds of ultracold atoms, achieving strong optical nonlinearities at the single-photon level remains a formidable task [93, 94, 95]. Moreover, several works pointed out that the very nature of light-matter interaction may prevent achievement of a sufficiently strong Kerr nonlinearity for weak quantum optical fields.

In 2001, Knill, Laflamme, and Milburn in their landmark paper [8] showed that effective nonlinear interactions at the single-photon level can be implemented with the use of optical interference, single photon detection and auxiliary single photons. In this approach, the single photon detection provides the desired nonlinearity. The resulting linear optical quantum gates are generally probabilistic, as implied by the fact that they are driven by quantum measurements, but their success probability can be boosted arbitrarily close to 1 by using more ancilla photons and more complex interferometric schemes. This concept has triggered an immense amount of theoretical and experimental work, which lead to demonstration of various two-qubit and three-qubit quantum gates for single-photon qubits. This concept has also been extended to Gaussian operations on continuous-variable states of light, where it was demonstrated that a squeezing operation can be implemented using an auxiliary source of squeezed states, interference, homodyne detection, and feedforward.

A fundamental nonlinear interaction is represented by a Kerr nonlinearity, which leads to dependence of the refractive index on the intensity of light that propagates through the nonlinear medium. At the quantum level, this nonlinearity is described by a Hamiltonian which is a quadratic function of the photon number operator $\hat{n}$,

$$\hat{H} = \hbar\kappa\hat{a}^{\dagger 2}\hat{a}^2 = \hbar\kappa\hat{n}(\hat{n}-1). \tag{5.1}$$

The resulting unitary transformation of the quantum state of the optical mode is diagonal in Fock basis, which means that each Fock state $|n\rangle$ acquires a phase shift which is a non-linear function of n,

$$|n\rangle \rightarrow e^{i\Phi\hat{n}(\hat{n}-1)}|n\rangle, \tag{5.2}$$

where $\Phi = \kappa t$. Strong Kerr nonlinearity with $\Phi \approx 1$ would enable e.g. generation of macroscopic superpositions of coherent states [96], implementation of entangling quantum gates for universal quantum computing [97], and complete Bell state measurement in quantum teleportation [98, 99].

In this chapter we present an experiment in which a fundamental (but very challenging) Kerr-type nonlinear interaction is emulated by means of superposition of single photon addition and subtraction. In particular we demonstrate how the effect of third order nonlinearity on weak states of light can be reproduced by using just a second order nonlinearity (PDC) in a measurement based approach.

5.1 Emulation of Kerr nonlinearity on weak states of light

In this section we report on the experimental implementation of a strong Kerr nonlinearity by measurement-induced quantum operations on weak quantum states of light. Specifically, we emulate this interaction on the smallest non-trivial subspace spanned by the vacuum, single-photon and two-photon states, $|0\rangle$, $|1\rangle$ and $|2\rangle$. In this subspace, the Kerr interaction transforms a generic input state according to

$$e^{-i\hat{H}t/\hbar}(c_0|0\rangle + c_1|1\rangle + c_2|2\rangle) = c_0|0\rangle + c_1|1\rangle + e^{-2i\Phi}c_2|2\rangle. \tag{5.3}$$

We target a Kerr nonlinearity with $\Phi = \pi/2$, which induces a π-phase shift of the two-photon Fock state with respect to states $|0\rangle$ and $|1\rangle$. Up to a linear π-phase shift which flips the sign of odd Fock states, and an unimportant overall phase factor -1, this is equivalent to a π-phase shift in the amplitude of the vacuum state on the three-dimensional subspace considered, i.e.,

$$c_0|0\rangle + c_1|1\rangle + c_2|2\rangle \rightarrow -c_0|0\rangle + c_1|1\rangle + c_2|2\rangle. \tag{5.4}$$

The change of sign in the amplitude of the vacuum component is thus the signature of the strong Kerr nonlinearity that we wish to demonstrate in our experiment. We do this by using weak coherent states as the input of an approximate Kerr Hamiltonian implemented with coherent superpositions of sequences of photon additions and subtractions, in the same scheme used for the implementation of the orthogonalizer operator (Sec.4.4.2).
Taking into account that $\hat{a}^\dagger\hat{a} = \hat{n}$ and $\hat{a}\hat{a}^\dagger = \hat{n} + 1$, we can thus design an arbitrary operation which is a linear function of the photon number operator

$$V(n) = (A + B)\hat{n} + A. \tag{5.5}$$

Here, we want to conditionally implement the gate of Eq.5.4 by means of the transformation $V(n)$, therefore we need to set

$$\begin{aligned} \frac{V(1)}{V(0)} &= -g \\ \frac{V(2)}{V(1)} &= g, \end{aligned} \tag{5.6}$$

where besides the desired operation, we allowed a simultaneous noiseless amplification of gain g, to make our task feasible

$$c_0|0\rangle + c_1|1\rangle + c_2|2\rangle \rightarrow -c_0|0\rangle + gc_1|1\rangle + g^2c_2|2\rangle. \tag{5.7}$$

The equations (5.6) now possess two solutions, only one of which admits a positive gain, that is

$$\begin{aligned} \frac{B}{A} &= -3-\sqrt{2} \\ \text{with} \quad & g=\sqrt{2}+1. \end{aligned} \tag{5.8}$$

Note, however, that this additional noiseless amplification does not spoil the signatures of nonlinearity. On the contrary, it is actually beneficial, because we intend to probe the quantum operation with weak coherent states and the amplification makes the observed nonlinear effect even more visible.

5.2 The experiment

Scheme The experimental scheme designed to implement the desired Kerr emulation is the same used for the implementation of the orthogonalization procedure in the photon number version illustrated in Sec.4.4.2.

Parameter setting The desired Kerr emulation requires an experimental parameter setting given by the general condition (4.24) with the particular condition (5.8)

$$\frac{CR_{aa^\dagger}}{CR_{a^\dagger a}}(\alpha) = \frac{1+3|\alpha|^2+|\alpha|^4}{|\alpha|^2+|\alpha|^4}\left(\frac{1}{-3-\sqrt{2}}\right)^2 \tag{5.9}$$

where $CR_{aa^\dagger}$ represents the count rate observed for the successful event of single photon subtraction and addition, instead $CR_{a^\dagger a}$ represents the successful event of single photon subtraction and addition.

5.3 Results

A full tomographic reconstruction is performed on the input and output states for three different values of the input coherent state amplitude, $\alpha=$ 0.23, 0.53 and 0.79. We use an iterative maximum likelihood procedure (see Appendix B) incorporating the effect of a finite ($\eta_{det}=0.66$) detector efficiency to reconstruct the density matrices in a 8x8 space in the Fock basis.

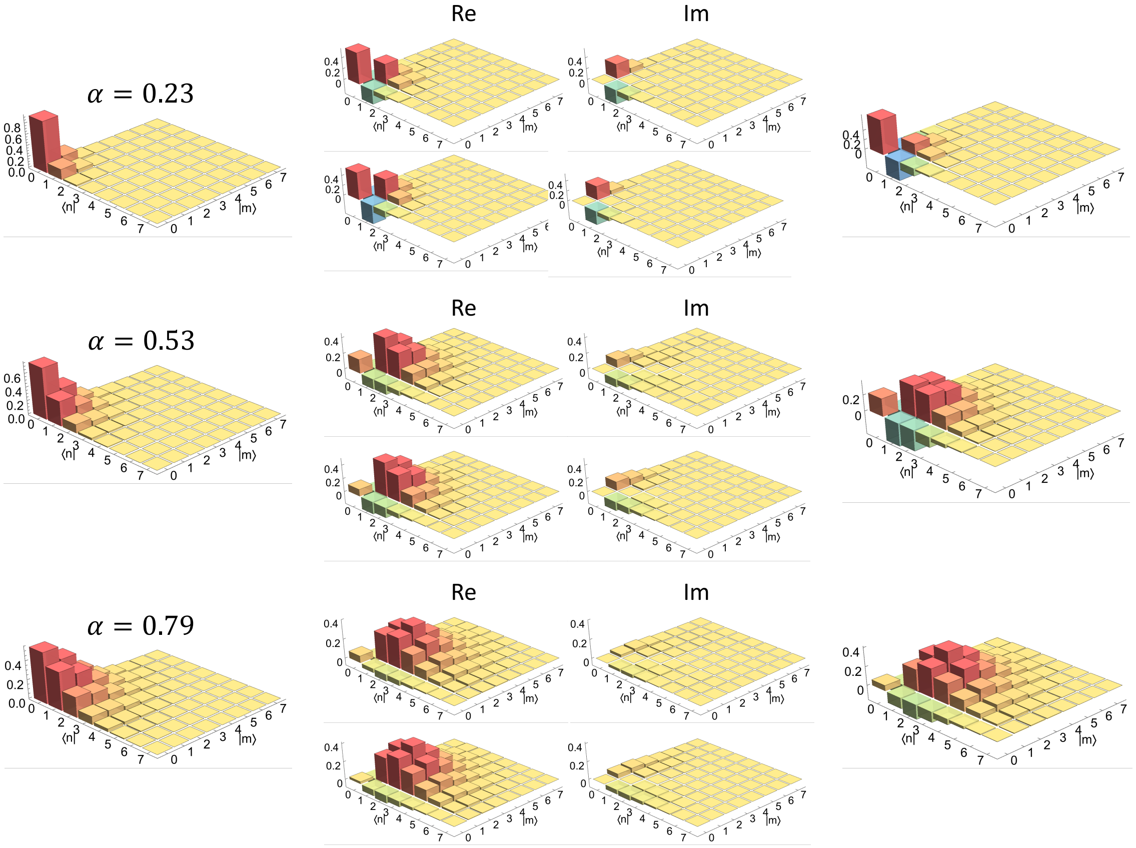

Figure 5.1: Reconstructed density matrices of input coherent states and output states after the emulated Kerr nonlinear interaction. The left column shows the real part of the reconstructed density matrices of the input coherent states (the imaginary part is negligible here). For each input state, the two central columns show the real and imaginary parts for the reconstructed output states (upper plots), together with those calculated from a best fit of the parameters in the applied $V(n)$ transformation (lower plots). Finally, the right column shows the expected output states (containing no imaginary parts) that one would obtain from the ideal $V(n)$ transformation with $B/A = -3 - \sqrt{2}$.

The reconstructed density matrices are shown in Fig.5.1 together with those calculated by applying the $V(n)$ operator on the input coherent states.

The desired Kerr nonlinearity signature is evident in all the experimental data. All the off-diagonal terms containing a vacuum contribution are clearly negative, witnessing the expected sign change in the amplitude of the vacuum component. However, when comparing the experimental density matrices to those expected according to the $V(n)$ transformation with ideal parameters $B/A = -3-\sqrt{2}$ (rightmost column in Fig.5.1), some discrepancy is apparent. The most notable is the appearance of a small (note the different vertical scales) imaginary component. We find that all the experimental results can be reproduced very well (with fidelities around 90 %) by using a single set of modified parameters in the $V(n)$ transformation, corresponding to a B/A ratio of -5.97 and to an additional phase of about $-\pi/7$ between the two terms in the operator superposition. Such small deviations from the ideal configuration, which only marginally affect the signatures of the sought nonlinearity, are fully compatible with the delicate alignment and setting of the proper small rotation angles in the waveplates responsible for the operator superposition.

In contrast to linear-optical quantum gates for single-photon qubits, our scheme is not restricted to single-photon inputs, but we have shown it to work for arbitrary superpositions of Fock states while preserving the quantum coherence. Moreover, the scheme is not based on post-processing, but the successful implementation of the operation (5.7) is heralded solely by measurements on auxiliary modes, thus making the output state available for further processing and applications.

Part III

(Quantum) mode manipulation

The last part of this thesis is dedicated to the mode manipulation technique, that is to the engineering of the spatiotemporal properties of a light pulse in a specific quantum state.
The first introductory chapter is dedicated to the general concept of mode manipulation, pointing out the main difference in respect to the state manipulation.
In the second chapter the interaction of ultrashort single photons with a resonant atomic gas is experimentally investigated as an application of the technique.

Chapter 6

Mode manipulation

This chapter represents a brief introduction to the *mode engineering*, an experimental technique in some sense complementary to the *state engineering* seen in Part II.

In Part II it has been observed that in state engineering based experiments, important physics is inferred by means of manipulation and consequent detection of quantum states. Anyway, it has been pointed out that a faithful characterization can be performed by means of a balanced homodyne detector only in case of a good spatio-temporal mode matching (characterized by the mode matching efficiency η_{mm}) of the the local oscillator to the manipulated state (see Sec.2.11).

In this Part III however we will see that interesting physical features can be observed by manipulating not the state but rather the mode of a system, that is by *engineering its spatio-temporal features*. In this case, a mode sensitive detector should be necessarily used to infer the important physics, and homodyne would be a perfect candidate in this sense (see Sec.2). However, since now the mode is the objective of the manipulation, the requirement of an high mode- matching is initially no more fulfilled. Homodyning is anyway still possible, provided that the target state is known and the local oscillator mode can be properly manipulated in the same way. Indeed, in a reversed perspective to the state engineering approach, once the state is known, one can tune the homodyne detection mode to that of the state, in order to observe what is expected for such a state. At that point, the local oscillator possesses the same spatio-temporal features of the manipulated system. This procedure enables for instance the observation of important physics at the single photon level, since the local oscillator mode can be more easily measured than that of the single photon by exploiting for instance a common technique like the Frequency-resolved optical gating (FROG), based on non-linear effects hardly exploitable at low intensity regimes.

Thanks to the extraordinary sensitivity of homodyne detection, this configuration allowed for instance the mentioned single photon level metrology [56],[57],[58], quantum enhanced measurements in a so-called *adaptive configuration* [59] as well as promising multimode information encoding by means of addressable frequency combs [61],[60].

Chapter 7

Zero-Area Single-Photon Pulses

7.1 Quantum memories

One of the most basic elements of the emerging quantum technologies is constituted by the so-called quantum memory [46], the quantum analog to common electronic memories. Quantum memories should permit to deterministicly store and keep safe quantum information for a sufficient amount of time and subsequently release it on demand for its processing.

Photons are ideally considered as the most privileged information carriers due to their robustness against environmental interactions, but for the system to use as a quantum memory the point is still debated and several systems have been indicated as appropriate. The development of such a device could have a remarkable importance for future technologies, since a physical system allowing one to trap and release photons could be exploited to convert heralded photons to on-demand ones, or used as a quantum repeater, permitting efficient long distance quantum communications. Several mechanisms have been then proposed and tested with this aim. For instance, optical delay lines and cavities have been used to store and release single photons by means of a deterministic manipulation of their polarization [47] or by controlling the transmittivity of optical cavities [48].

Completely different approaches have been instead based on some type of atom-field interactions, for instance exploiting electromagnetically induced transparent (EIT) media to optically handle the transmission/absorption of the light passing through. Anyway, since atomic systems, either made of cold and ultracold atoms or of hot vapours, have absorption linewidths in the Hz to GHz range, the main road to enhancing the atom-photon interaction has always been that of using sufficiently narrow-band quantum photonic states, either produced in cavity-enhanced parametric down-conversion sources [76],[77],[78],[79], or directly from cold [80][81],[86],[83] or hot [84, 85] atomic samples. In general, ultrashort single photons with bandwidths much broader than the atomic bandwidth are therefore not considered useful for this task because they are thought to interact only very weakly with the atoms.

Considering that one of the most popular (and efficient) single-photon sources, the parametric down-conversion in a pulsed pumping regime is broadband, an effective mechanism to collect and conserve quantum information despite the huge bandwidth mismatch with the narrowline atomic media could be very useful.

Then, in this chapter we introduce and discuss the experimental evidence of an alternative matter-light interaction concerning broadband single photons propagating in a much narrower linewitdh atomic vapour, referred to as 0π dynamics. The interaction can be considered in some sense unexpected, since the huge spectral mismatch of the two involved systems clearly leads to a very small probability for the absorption. To prove the interaction we consider the traces left on the single photon temporal shape by its encounter with the atoms, in a *mode engineering* based experiment.

7.2 0π dynamics

The resonant interaction between ultrashort classical pulses and atomic media has long been investigated, together with some of its most peculiar effects. In this section we examine the problem of broadband light propagating within a medium that can be described as a simple two-level system, that is a medium with a single absorption line centered at the optical frequency, so that only one resonant transition can be considered.

Firstly we show that just by propagating through the atoms, broadband low intensity pulses necessarily experience a reshaping of their temporal profile. In the following section the problem is analyzed more formally by means of the Maxwell-Bloch equations, and an important and very general result, the *area theorem* is presented. As a particular case of this result, the formation of zero-area single photon pulses will be analyzed and the sense of the name "0π" will be more clear.

7.2.1 0π dynamics: an intuitive picture

Let's imagine a light pulse at the optical frequency ω_f travelling through a gaseous atomic medium. Suppose the frequency ω_f resonant with one and only one atomic transition, as all the other atomic excitations occur at completely different frequencies, and consider the inhomogeneously broadened[1] absorption line thousand of times narrower than the radiation spectrum. In this condition it can be demonstrated that the effect of tha propagation over a distance l within the medium affects the electric field shape $E(\omega, z)$ as the function [74]

$$\begin{aligned} E(\omega, l) &= E(\omega, 0)\, e^{\frac{-\gamma\, l}{1-i(\omega-\omega_f)\, T}} \\ &= E(\omega, 0)\, e^{\frac{-\gamma\, l}{1+(\omega-\omega_f)^2\, T^2} - i\frac{\gamma\, l\, (\omega-\omega_f)\, T}{1+(\omega-\omega_f)^2\, T^2}} \end{aligned} \tag{7.1}$$

where $E(\omega, 0)$ is the electric field before having entered the atomic medium, $T \approx 1/2\sigma_a$ is the inhomogeneous level lifetime and γ is the optical density of the material. This approximate expression, which considers two-level atoms and an effective single Lorentzian profile for the resonance line of the sample is enough to convey all the main features of the phenomenon.The real part of the exponent in Eq.(7.1) explains the exponential decrease of energy due to the loss within the material at the atomic resonance as depicted by the Beer-Lambert's law. The imaginary term describes instead the dispersion experienced by the field through the medium.

It is evident from Fig.7.1 that because of the huge mismatch in the spectral widths, the more the light pulse propagates, the deeper the infinitesimally thin hole dug in the center of the spectrum by the atoms. Indeed, due to the atomic transition being so narrow, the absorbed pulse energy is almost negligible even in the case of high optical depths, but (combined with the dispersion) it may still cause a dramatic reshaping of the temporal pulse envelope. So, we can get an intuitive picture of the dynamics by thinking that after a sufficiently long distance of propagation, two separated lobes emerge in the spectrum at opposite frequencies around ω_f, inducing the appearance of temporal beat notes in the pulse profile.

---

[1] For instance due to the Doppler effect.

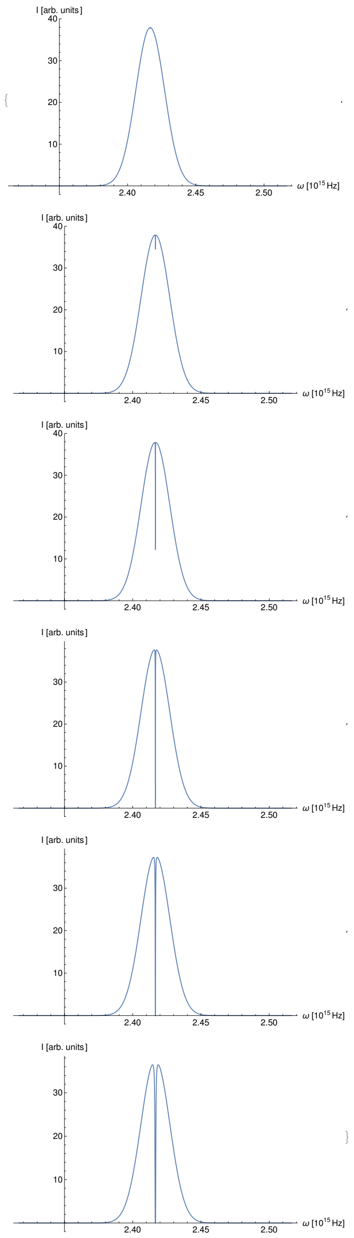

Figure 7.1: Simulation of the effect on a broadband resonant light spectrum due to propagation within a narrowwidth material, calculated according to Eq.(7.1) respectively with $\gamma \approx 0.07, 1.1, 12, 96, 580, 2825$ and a Doppler lifetime $T \approx 323, 307, 293, 280, 270, 260$ ps. A 8 nm spectral FWHM at 780 nm has been considerated for the propagating light pulse.

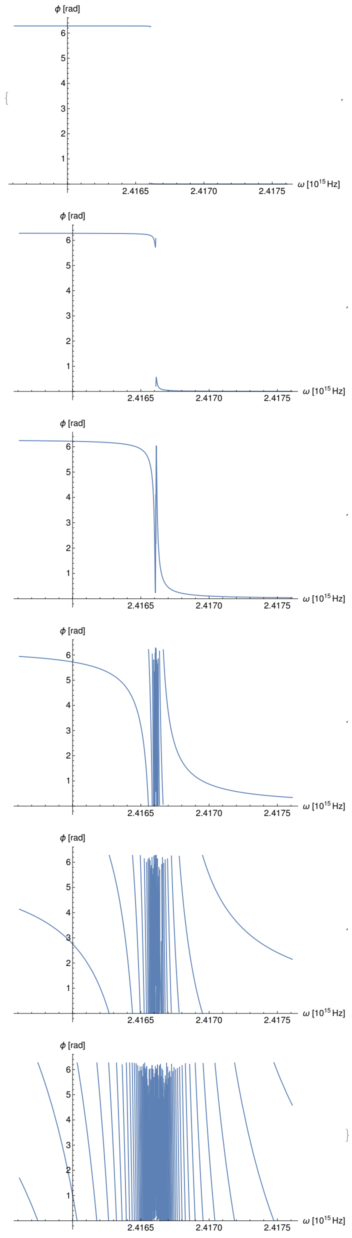

Figure 7.2: Simulation of phase shift experienced by a broadband resonant light spectrum induced by the dispersion due to the propagation within a narrowwidth material, calculated according to Eq.(7.1) with the same values of Fig.7.1.

7.2.2 Semiclassical description of the light-matter coherent interaction

The 0π dynamics qualitatively justified in the previous section simply by means of the losses into the material, can be theoretically framed in the more general context concerning the interaction of resonant ultrashort pulses with two-level systems. As we will see, this general analysis leads to the *area theorem*, a particular case of which is just the 0π pulse formation [50], [51]. Basically the *area theorem* describes the temporal reshaping experienced by short light pulses when interacting with resonant absorption narrow-line materials. The name *area* refers to the integral of the electric field envelope $\mathcal{E}\left(x,t\right)$ over time, i.e.

$$\theta(x) = \frac{\mu}{\hbar}\int_{-\infty}^{+\infty} \mathcal{E}\left(x,t\right)\ dt. \tag{7.2}$$

where μ is the transition electric dipole moment. The theorem asserts that $\theta(x)$ is a solution of the equation

$$\frac{d}{dx}\theta\left(x\right) \quad = \quad \alpha\sin\theta\left(x\right). \tag{7.3}$$

with the constant α depending on the atomic medium. An immediate consequence is that in stationary conditions the *area* tends always to assume fixed values multiples of π, that is $\theta\left(x\right) = m\pi$. In particular, for extremely weak fields, like in the single-photon case, the envelope $\mathcal{E}\left(x,t\right)$ necessarily has to oscillate between positive and negative values to make the *area* null ($m = 0$ solution).

By considering that we are dealing with radiation so short to be spectrally much broader than the resonant atomic linewidth ($\approx 10^3 \div 10^4$ times), a first intuitive picture could bring to wrongly expect no light-matter interaction at all. Indeed because of the huge mismatch in the frequencies, absorption is expected to barely take place. But counter-intuitively, interaction doesn't mean necessarily only absorption.

For sufficiently high intensities to excite atomic nonlinearities, the area theorem has strong consequences as it can predict not only the absence of absorption in spite of Beer-Lambert's law, but also the existence of exotic states of light like solitons, i.e. light pulses that propagate through matter with an unperturbed shape.

To explain the process more formally, we consider the interaction of a short electromagnetic pulse with a collection of N atoms. We suppose the radiation pulse sufficiently short to ignore any dephasing effect (because acting on longer timescales) and we treat the process semiclassically, i.e. with the field described by a classical vector and the atoms described by a state living in a two-level Hilbert space. We will demonstrate a set of general equations focused on describing the interaction of the radiation with a two-level system. This approach is equivalent to the one developed by Arecchi and Bonifacio [53], the starting point for the original demonstration of 1970 by M. D. Crisp [54]. We do not provide the mathematical proof of the result, but enounce the *area theorem* directly. The point here is indeed not a discussion about the formal details, but only to give a general view of the physical conditions necessary for the phenomenon to take place. In the final stage, the 0π pulse formation is discussed as the result of the application of the theorem in the low-intensity regime.

Maxwell equations in presence of matter To start, let's consider the joint action of the four Maxwell's equations for the total electric field E_{tot} within an ensemble of N active atoms embedded in a passive medium. Suppose to decompose the induced polarization into a passive and an active atomic contribution, $P_{eff} = P_{pass} + P_{act}$. We will see that the passive term is necessary just to define the environment where the interaction takes place. For the sake of simplicity consider the passive contribution as linearly induced by the electric field $P_{pass} = \epsilon_0 \chi_{pass} E_{tot}$

$$\begin{aligned}\left(\frac{\partial^2}{\partial x^2} - \frac{1}{c^2}\frac{\partial^2}{\partial t^2}\right) E_{tot} &= \frac{1}{\epsilon_0 c^2}\frac{\partial^2}{\partial t^2} P_{eff} \\ &= \frac{1}{\epsilon_0 c^2}\frac{\partial^2}{\partial t^2}\left(P_{pass} + P_{act}\right) \\ &= \frac{1}{\epsilon_0 c^2}\frac{\partial^2}{\partial t^2}\left(\epsilon_0 \chi_{pass} E_{tot} + P_{act}\right). \qquad (7.4)\end{aligned}$$

where c is the light speed and ϵ_0 the absolute permittivity in vacuum. Then we get

$$\left(v_{pass}^2 \frac{\partial^2}{\partial x^2} - \frac{\partial^2}{\partial t^2}\right) E_{tot} = \frac{1}{\epsilon_{pass}}\frac{\partial^2}{\partial t^2} P_{act} \qquad (7.5)$$

where we made use of the usual relations

$$n_{pass} = \frac{c}{v_{pass}} = \sqrt{1+\chi_{pass}} = \sqrt{\frac{\epsilon_{pass}\mu_{pass}}{\epsilon_0\mu_0}} \approx \sqrt{\frac{\epsilon_{pass}}{\epsilon_0}}. \tag{7.6}$$

with v_{pass} the speed of light within the passive medium. To simplify, let's factorize optical frequency ω_f and wavenumber k_f

$$E_{tot} = E\left(e^{i(k_f x - \omega_f t)} + c.c.\right) \qquad P_{act} = P\left(e^{i(k_f x - \omega_f t)} + c.c\right) \tag{7.7}$$

and by introducing the *slow varying envelope approximation (SVEA)*

$$\omega_f|E| \gg \frac{\partial E}{\partial t} \qquad k_f|E| \gg \frac{\partial E}{\partial x} \qquad \omega_f|P| \gg \frac{\partial P}{\partial t} \tag{7.8}$$

eq.(7.5) becomes

$$\left(v\frac{\partial}{\partial x} + \frac{\partial}{\partial t}\right)E \;=\; \frac{i\omega_f}{\epsilon_0'}P. \tag{7.9}$$

with $\epsilon_0' = n_{pass}^2\,\epsilon_0$.

Atomic equations To close eq.(7.9) we need a microscopic model to connect the atomic polarization with the macroscopic electric field. Our hypothesis will be to consider the total polarization as composed of N independent atomic dipoles

$$P = Np. \tag{7.10}$$

Supposing a near resonance radiation field, the atomic system can be then described by using a simple two-level system

$$|\Psi\rangle = a_1|\Psi_1\rangle + a_2|\Psi_2\rangle, \tag{7.11}$$

where $|\Psi_1\rangle$ and $|\Psi_2\rangle$ are orthonormal eigenvectors corresponding to the ground and excited levels of an Hamiltonian $\hat{H}_0$. The effect of an external electric field results in an additional interaction term in the Hamiltonian, as

$$\begin{aligned}\hat{H}_{tot} &= \hat{H}_0 + \hat{H}_{int} \\ &= \hat{H}_0 - e\hat{X}E_{tot} \end{aligned} \tag{7.12}$$

where $\hat{H}_{int} = -e\hat{X}E_{tot}$ represents the dipole interaction Hamiltonian. By projecting the Schrdinger equation on $\langle\Psi_1|$ and $\langle\Psi_2|$ we obtain the probability amplitudes

$$\begin{aligned} i\hbar\frac{\partial}{\partial t}a_1 &= \langle\Psi_1|\hat{H}_{tot}|\Psi\rangle \\ &= \hbar\omega_1 - ex_{12}E_{tot}a_2 \end{aligned} \tag{7.13}$$

and

$$\begin{aligned} i\hbar\frac{\partial}{\partial t}a_2 &= \langle\Psi_2|\hat{H}_{tot}|\Psi\rangle \\ &= \hbar\omega_2 - ex_{21}E_{tot}a_1. \end{aligned} \tag{7.14}$$

Eqs.(7.13) and (7.14) have been derived by supposing the E_{tot} constant over the integration volume and considering a vanishing permanent atomic dipole moment on both the levels ($\langle\Psi_1|\hat{X}|\Psi_1\rangle = \langle\Psi_2|\hat{X}|\Psi_2\rangle = 0$).
Multiplicating each equation by the other, we obtain for the density matrix elements

$$\begin{aligned} \frac{\partial}{\partial t}\rho_{21} &= \frac{\partial}{\partial t}a_2a_1^* \\ &= -i\left(\omega_2 - \omega_1\right)a_2a_1^* + i\frac{\mu}{\hbar}E_{tot}\left(a_1a_1^* - a_2a_2^*\right) \\ &= -i\left(\omega_2 - \omega_1\right)\rho_{21} + i\frac{\mu}{\hbar}E_{tot}\left(\rho_{11} - \rho_{22}\right) \qquad (7.15) \\ \frac{\partial}{\partial t}\rho_{11} &= -\frac{\partial}{\partial t}\rho_{22} = \frac{\partial}{\partial t}a_1a_1^* = -\frac{\partial}{\partial t}a_2a_2^* \\ &= i\frac{\mu}{\hbar}E_{tot}\left(a_2a_1^* - a_1a_2^*\right) \\ &= i\frac{\mu}{\hbar}E_{tot}\left(\rho_{21} - \rho_{12}\right) \qquad (7.16) \end{aligned}$$

where the dipole matrix element $ex_{21} = ex_{21} = \mu$ has been taken as real. If we now decompose eqs.(7.15),(7.16) as (7.7) and neglect fast oscillating terms by introducing the *rotating wave approximation*, in the hypothesis (7.10) of N independent oscillating dipoles we obtain the final set of equations

$$\begin{aligned}
\left(v\frac{\partial}{\partial x}+\frac{\partial}{\partial t}\right)E &= \frac{i\omega_f N\sigma}{\epsilon_0'}\sigma && (7.17)\\
\frac{\partial}{\partial t}\sigma &= -i\left(\omega_a-\omega_f\right)\sigma+i\frac{\mu}{2\hbar}En && (7.18)\\
\frac{\partial}{\partial t}n &= i\frac{\mu}{\hbar}\left(E^*\sigma-E\sigma^*\right). && (7.19)
\end{aligned}$$

where we introduced the population difference $n=\rho_{11}-\rho_{22}$ and $\rho_{21}=\sigma e^{i\left(\omega_f t-k_f x\right)}$ and $\omega_a=\omega_2-\omega_1$.
To generalize a bit more eqs.(7.17),(7.18),(7.19), we can take into account the inhomogeneous dispersion of the atomic frequency for example due to Doppler spread, by making the substitution $\sigma\rightarrow\int g(\omega)\sigma(\omega)\,d\omega$ and $n\rightarrow\int g(\omega)n(\omega)\,d\omega$ where the resonance condition implies $g(\omega)$ maximum at the optical frequency

$$\begin{aligned}
\left(v\frac{\partial}{\partial x}+\frac{\partial}{\partial t}\right)E &= \frac{i\omega_f N\sigma}{\epsilon_0'}\int g(\omega)\sigma(\omega)\,d\omega && (7.20)\\
\frac{\partial}{\partial t}\sigma &= -i\left(\omega_a-\omega_f\right)\sigma+i\frac{\mu}{2\hbar}En && (7.21)\\
\frac{\partial}{\partial t}n &= i\frac{\mu}{\hbar}\left(E^*\sigma-E\sigma^*\right). && (7.22)
\end{aligned}$$

Area theorem By means of a proper manipulation of the equations (7.20),(7.21),(7.22), the *area theorem* can be at this point obtained without necessity of any further hypothesis. Defining the so-called *area* as the integral over time of the electric field envelope $\mathcal{E}\left(x,t\right)$

$$\theta(x,t)=\frac{\mu}{\hbar}\int_{-\infty}^{t}\mathcal{E}\left(x,t'\right)\ dt' \qquad (7.23)$$

where the envelope is defined as $E=\mathcal{E}\left(x,t\right)e^{i\phi(x,t)}$, the area theorem states that in stationary conditions

$$\frac{d}{dx}\theta\left(x\right) = \alpha\sin\theta\left(x\right), \qquad (7.24)$$

with the material constant given by

$$\alpha = -\frac{N\pi\mu^2\omega_f n}{2\hbar\epsilon_{pass}v_{pass}} g\left(\omega_f\right) \tag{7.25}$$

and

$$\lim_{t\to+\infty}\theta\left(x,t\right) = \theta\left(x\right). \tag{7.26}$$

A complete mathematical proof is beyond the purpose of this work and can be found in [55], [54],[71] or [22].
We notice that the theorem implies the existence of a class of stationary solutions, for which $\theta\left(x\right) = m\pi$, that propagates through atoms without further alteration of the area. In any case, depending on the initial value, $\theta\left(x\right)$ will always tend to an integer multiple of π.
We notice that the *area theorem* finds an interesting interpretation in the oscillation of atomic population in the Rabi's theory of interaction. Indeed, an *area* value of $m\pi$ can be simply viewed as a flipping of an $m\pi$ angle of the atomic dipole induced by the passage of the light pulse.

Range of validity It is important to observe now that the eqs.(7.20),(7.21),(7.22) have been obtained by ignoring any possible cause of dephasing. This can be considered the consequence of an implicit hypothesis of having considered the loss of coherence taking place on a much longer temporal scale compared to the duration of the interaction.
Actually, in the interaction between the radiation and a two-level system the dynamics can be basically described by making use of two fundamental time scales: the longitudinal relaxation time representing the lifetime of the excited atoms (or molecules) staying in the high energy level and defined as $T_1 = 1/\delta\nu_{hom}$, where $\delta\nu_{hom}$ is the natural linewidth of the transition, and the inhomogeneous relaxation time governing the time scale on which the loss of coherence takes place, defined as $T_2 = 1/\delta\nu_{inhom}$, where $\delta\nu_{inhom}$ is the inhomogeneous broadening linewidth of the same resonant transition. For solid-state media at very low temperature, it usually holds that $T_2 < T_1$ whereas for gaseous media at normal temperature (and not extremely high pressure) the inequality is stronger since $T_2 \ll T_1$.
A regime of coherent propagation is thus considered valid whenever

$$\Delta t \ll T_2, T1 \tag{7.27}$$

with Δt given by the pulse duration[71]. For instance, the resonant interaction of broadband light within a gas with a much narrower linewidth gas can be considered to occur in a coherent regime.

The area of a single photon Here we are interested in the consequences of the *area theorem* in the extreme case of a single photon pulse. In this low intensity regime the dynamics takes the particular name of 0π propagation, since the small initial *area* will tend always to 0.
We can easily verify that the value of $\theta\,(x)$ is really small in the case of single photons. Let's consider for instance the conditions for the experiment described in this chapter: 50 μm for the beam waist w_0, 100 fs for the pulse duration Δt and a 800 nm wavelength λ. We can estimate an electromagnetic energy density for the single photon as

$$\begin{aligned}
\frac{\epsilon_0 |\mathcal{E}|^2}{2} &= \frac{h\nu}{V} \\
&= \frac{h\,c}{\lambda\,\pi w_0^2\,\Delta t\,c} \\
&= \frac{6.6\cdot 10^{-34}}{8\cdot 10^{-7}\,\pi\ \cdot (50\cdot 10^{-6})^2\,10^{-13}} J \\
&= 10^{-4} J/m^3,
\end{aligned}$$

that implies an electric field amplitude

$$\begin{aligned}
|\mathcal{E}| &= \sqrt{\frac{2\cdot 10^{-4}}{\epsilon_0}} \\
&\approx 500 V/m.
\end{aligned} \tag{7.28}$$

At this point we can verify from eq.(7.23) that the single-photon *area* $\theta\,(x)$

$$\begin{aligned}
\theta(x,t) &= \frac{\mu}{\hbar}\int_{-\infty}^{t} \mathcal{E}\left(x,t'\right)\ dt' \\
&\approx \frac{a_0\, e}{\hbar}\left|\mathcal{E}\right|\Delta t \\
&= 4\cdot 10^{-6} rad. \qquad (7.29)
\end{aligned}$$

where a_0 is the Bohr radius.

0π **dynamics** In the condition of small *area* we can faithfully approximate $\sin\theta\left(x\right)$ with its argument $\theta\left(x\right)$ and, from the *area theorem*, we get

$$\frac{d}{dx}\theta\left(x\right) \approx \alpha\,\theta\left(x\right). \qquad (7.30)$$

Note that the constant α is negative for atoms initially in the ground state. Eq.(7.30) then leads to an exponential decrease of the *area*, accomplished by the appearance of evident oscillation between positive and negative values in the shape of the envelope $\mathcal{E}$. Then, the more the light pulse propagates, the higher the decrease of the *area* until it approaches zero without further distortions. Indeed, once formed, a zero-area pulse is remarkably robust and propagates without further losses.

7.3 0π quantum memory

Although most studies concentrated on the effects of propagation on the shape of the optical pulse itself, it has also been pointed out that zero-area pulses can significantly enhance the transient excitation of the atoms [74], even though the final excitation left in the medium after the passage of the pulse is negligible. This transient excitation, however, can be mapped into a final, nonnegligible excitation of a different atomic level by means of a second ultrashort field acting on the excited state during the transient [74]. Such a small excitation probability per atom distributed throughout a large atomic ensemble may lead to the final absorption of a single photon and its mapping to a collective state, in a broadband version (due to the broadband nature of the two photon transition) of various single-photon memories with atomic ensembles that have been proposed and successfully implemented in the narrow-band regime [86, 83, 84].

All previous experimental studies of broadband pulse interaction with narrow-band atomic ensembles were carried out with weak classical light pulses (see, for example [84, 85, 86, 87]). However, the formation of zero-area single-photon (SP) pulses has been recently proposed as a possible way to engineer quantum states using time-dependent effects and for time-domain quantum information processing[75].

7.4 The experiment

Here we present the first experimental demonstration of zero-area pulse formation within the wave packet temporal mode of a single photon. We propagate ultrashort heralded photons with a broad bandwidth centered at 780 nm through a cell containing resonant hot rubidium vapour and find that, despite a negligibly small absorption, the transmitted SP wave packets acquire the strong temporal modulation characteristic of zero-area pulses. We use our recently developed techniques of ultrafast, mode-selective, time-domain, homodyne detection to measure the coherently modulated SP profiles and to verify that the quantum character of the input states is not degraded upon transformation of the mode.

The master light source for our experiment (see Fig.7.3) is a mode-locked Ti:sapphire laser, emitting a train of 100 fs, 780 nm pulses at a repetition rate of 80 MHz. Note that in this case we used a different laser with a much shorter pulse duration compared to the experiments described in the previous chapters. Most of the laser emission is frequency doubled to produce the pump pulses for generating single photons in a travelling wave packet mode from heralded spontaneous parametric down-conversion in a 300 μm thick crystal of type-I β-barium borate (BBO). Frequency-degenerate signal and idler photons are emitted along a cone; the detection of an idler photon in a fiber-coupled avalanche photodiode (APD) placed after narrow spectral and spatial filters [a 1 nm FWHM interference filter (F) and the APD single-mode fiber (SMF)] heralds the generation of pure broadband single photons resonant with the $5S_{1/2} - 5P_{3/2}$ D2 transition of Rb in the conjugated signal mode. Previous investigations [56] have shown that our setup is able to generate SP pulses in a quasi-transform-limited wave packet mode with a duration of about 100 fs.

A smaller portion (about 8 mW) of the laser emission serves as the local oscillator (LO) for heralded, homodyne detection (see Sec.2) after mixing with the signal on a 50% beam splitter (BS). When analysing heralded single photons, we measure a state which can be generally written as

$$\rho = \eta_{tot} \, |1\rangle\langle 1| + (1 - \eta_{tot}) \, |0\rangle\langle 0| \tag{7.31}$$

i.e., a mixture of vacuum and SP Fock states in the mode defined by the homodyne LO. The global efficiency η_{tot}, as already mentioned in Sec.3.52, depends upon several factors: limited state preparation efficiency, limited quantum efficiency of the homodyne photodiodes, optical losses, electronic noise, and dark counts in the APD. Above all, however, it depends on the mode matching η_{mm} between the heralded state and the LO, i.e., on how well the spatial and spectrotemporal profiles of the LO are overlapped to those of the state to be measured (see Eq.(2.11)). Spatial matching is simply obtained by means of lens combinations after pinhole spatial filtering. Spectrotemporal mode matching can be achieved by shaping the spectral amplitude and phase of the LO by means of a liquid-crystal pixelated spatial light modulator in a $4 - f$, zero-dispersion, configuration [56, 88]. This results in the generation of LO pulses with arbitrarily shaped spectrotemporal profiles. Using an optimized spatiotemporal LO mode, we routinely measure SP fractions up to $\eta \approx 62\%$ in our setup for the freely propagating conditions.

7.4.1 Unmodulated local oscillator

Classical pulse cross correlation In order to preliminarily test the system and optimize the homodyne detection of modulated SP wave packets, we first make use of the intense stimulated emission that takes place in the output signal mode of the parametric crystal when seeded by intense synchronized 780 nm pulses in the input idler mode (see Fig.7.3) Emission of this intense classical radiation is known to take place into a mode that closely matches that of the heralded photons [27]. A temperature-stabilized 8 cm long cell containing natural abundance Rb is placed in the common path of the classical and SP wave packets.

Figure 7.4 shows the visibility of the interference fringes measured at one exit of the homodyne beam splitter between such classical pulses and unmodulated LO pulses with the same intensity. According to Eq.(3.55)

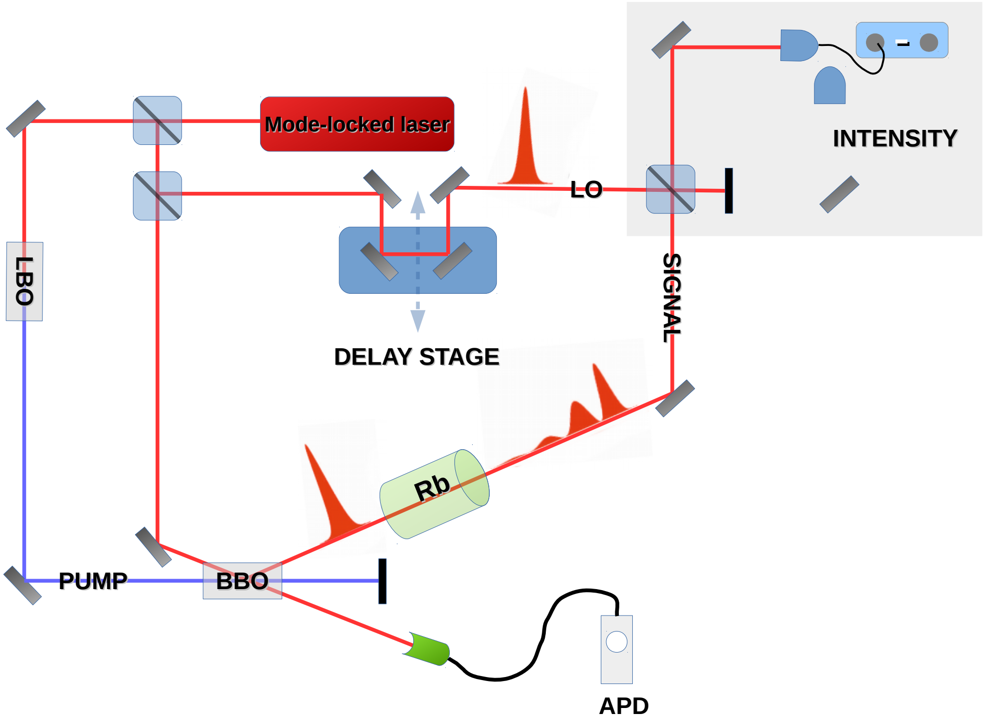

Figure 7.3: Experimental scheme used to measure the linear cross-correlation of Fig.7.4, between an unmodulated LO pulse and classical pulses passing through the resonant Rb cell. A seed coherent pulse is used to provide reference classical pulses in the same spatiotemporal mode of the single photons. Two mirrors have been mounted on a motorized linear translation stage to adjust the delay τ between the two optical paths. LBO is a lithium triborate crystal for second harmonic generation. All other symbols are defined in the text.

such a visibility is given by

$$V(\beta,\alpha,\tau)=\mathcal{R}\left\{\int dt\,\beta^*(t)\,\alpha(t+\tau)\right\} \tag{7.32}$$

with $\beta(t)$ representing the mode of the classical pulse and $\tilde{\alpha}(t+\tau)$ that of the local oscillator as a function of the relative delay. The measurement has been repeated for different values of the cell temperature. Starting from a single peak at zero delay, this linear cross-correlation curve develops growing lobes at higher temperatures that clearly testify to the formation of classical zero-area pulses.

Single-photon homodyne detection The seed idler pulses are then blocked to perform homodyne measurements of the modulated SP wave packets (see Fig.7.5). When the Rb cell is first inserted in the path of the heralded single photons at room temperature, the only effect is a slight decrease in the total efficiency η_{tot} due to residual losses in the antireflection coated cell windows. However, increasing the temperature of the cell has the effect of rapidly degrading the measured global efficiency if the LO mode is left unchanged. In these situations, we expect the SP temporal mode to start being heavily modulated by atomic dispersion, so that the homodyne detector sees larger and larger fractions of vacuum in the original LO mode as the temperature (and the atomic density) increases (see Eq.(7.31)). Indeed we can see from Eq.(2.11) (and Eq.(3.52)) that the detection efficiency η_{mm} (and then the total efficiency η_{tot} too) is quadratically degradated by the mismatch of the local oscillator to the heralded signal mode.

The first series of measurements consists of acquiring phase-averaged quadrature distributions and extracting the global SP efficiency η_{tot} of Eq.(7.31) as a function of the delay τ between the modulated SP pulse and the unmodulated (and phase-randomized) LO (see Fig.7.5). This results in a sort of cross-correlation measurement, similar to the classical one described above, but now performed with the exceptional sensitivity typical of homodyne detection. Actually, this kind of time-dependent measurement can be viewed in the more general framework of intensity-field correlations [89, 90, 91], which are known to open enormous possibilities for the analysis of the quantum properties of the field and may provide detailed information about the coherent atomic excitation dynamics.
Figure 7.6 shows several plots of $\eta_{tot}(\tau)$ for different temperatures of the Rb

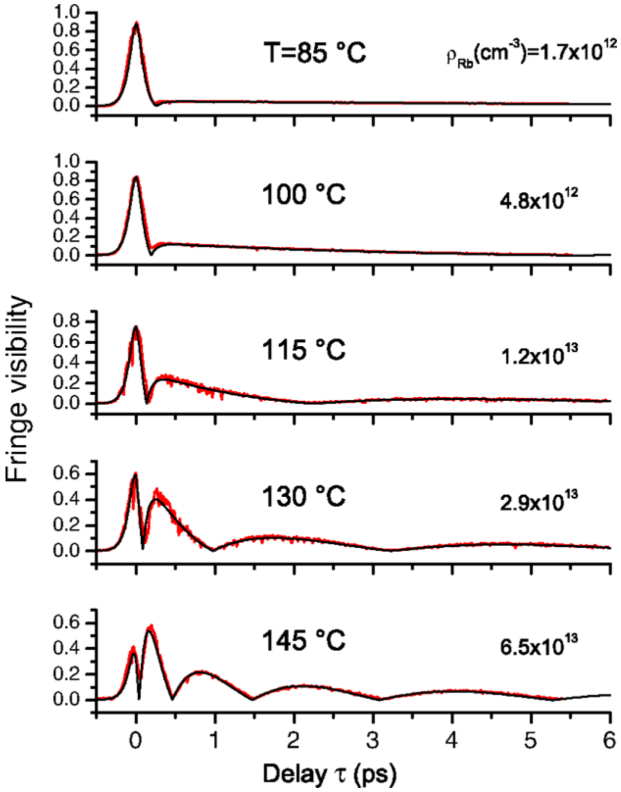

Figure 7.4: Experimental visibility of the interference fringes as a function of the delay (linear cross-correlation) between an unmodulated LO pulse of ≈ 100fs FWHM duration and classical pulses passing through the resonant Rb cell. At higher temperatures, corresponding to higher estimated Rb densities, the pulses are seen to acquire a typical zero-area shape extending over several picoseconds. Solid black curves are field amplitudes calculated according to Eq.(7.1), with optical depths $\gamma l = 70, 180, 440, 1000, 2200$ (from top to bottom), and using for T the Doppler inhomogeneous lifetimes (between 280 and 260 ps) at the measured temperatures.

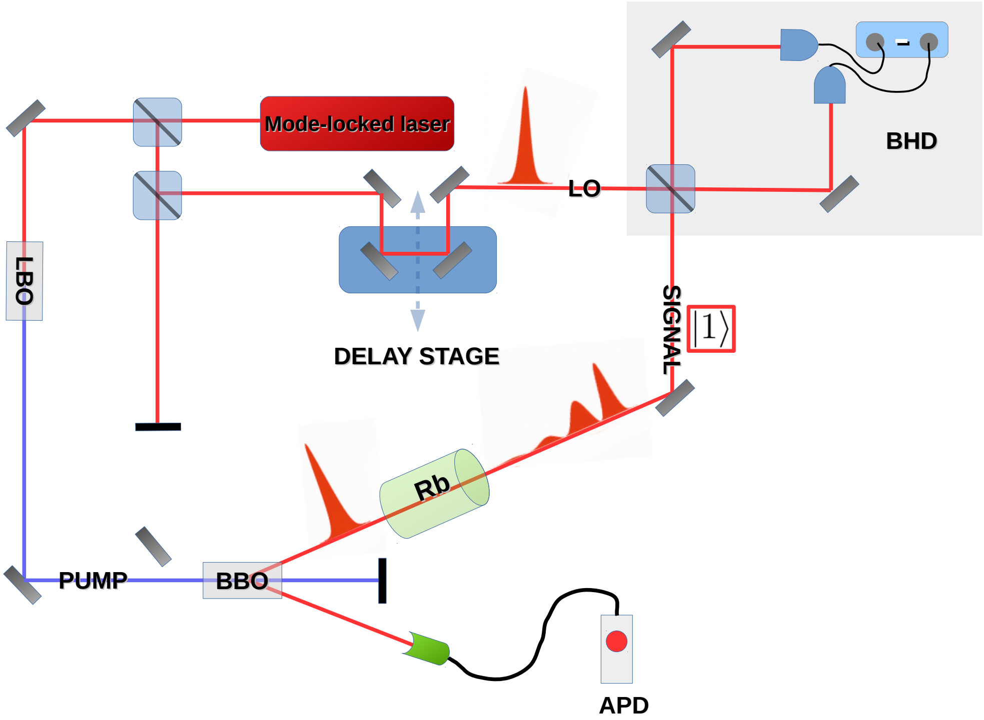

Figure 7.5: Experimental setup. Heralded spontaneously downconverted single-photon pulses interact with a resonant Rb vapour and are analyzed by a balanced homodyne detector (BHD). The seed coherent beam is now blocked.

cell. At low temperatures, a single peak of high efficiency is observed, because the LO mode reproduces well the almost unperturbed SP mode. At higher densities, the efficiency curves are seen to acquire strong modulations at increasing delays while the maximum efficiency in the main lobe drops. In these cases, the short LO is no longer well overlapped to the heavily modulated SP, and only a fraction of the latter is detected in the LO mode at any delay.

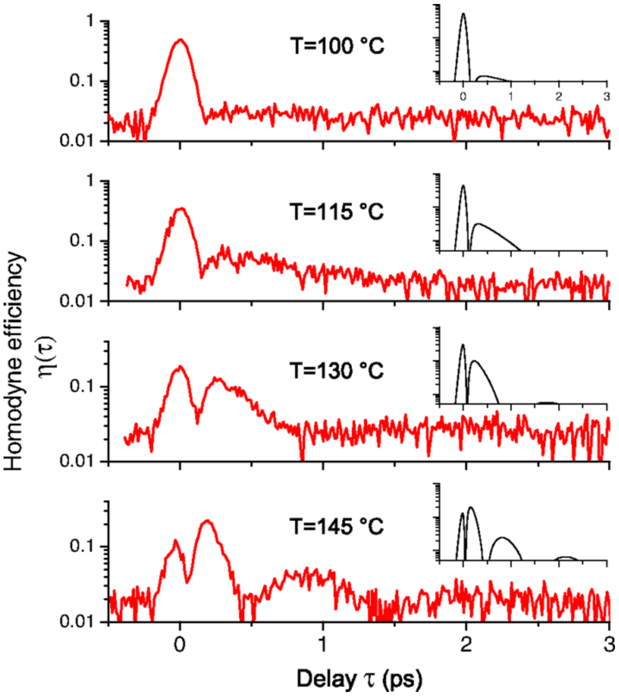

Figure 7.6: Measured homodyne efficiency curves (in logarithmic scale) as a function of the delay between the unmodulated LO pulses and heralded single photons that interacted with the Rb atoms in the cell. The temporal mode of the single photons is heavily distorted at sufficiently high cell temperatures. Theoretical intensity curves calculated with the same parameters of Fig.7.4 are shown in the insets.

The red experimental data points of Fig.7.7 correspond to the maximum efficiencies of these curves, and clearly illustrate the rapid loss of the SP component from the LO mode as the optical depth increases with temperature. The nonmonotonic behaviour of the data at higher temperatures is easily explained by the fact that, in these conditions, the SP mode gets so distorted that the main lobe actually contains a smaller SP fraction than the first secondary lobe (see last curve of Fig.7.6).

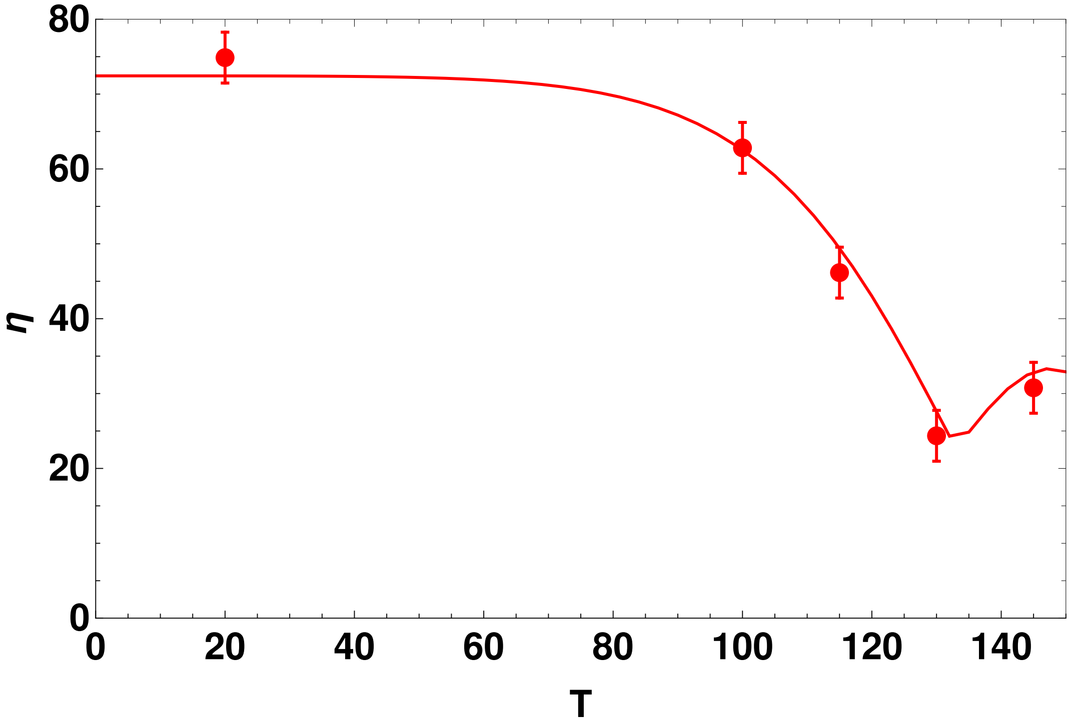

Figure 7.7: Experimental data and theoretical curve for the maximum homodyne efficiency in the detection of distorted single-photon wave packets with unmodulated LO.

Dropping peak efficiencies might suggest that the original, relatively pure, single photons have been irremediably lost and converted to classical mixtures with vacuum after passing through hot resonant atomic vapours with optical depths in excess of 2000. However, the absorption by the narrow (of the order of GHz) atomic resonance is not to be blamed for this, due to the much larger SP bandwidth (of the order of THz). In fact, the generated single photons are only lost from the homodyne detection mode defined by the unmodulated LO. The red solid curve represents the peak efficiency η_{tot}

calculated by simulating the mode matching (Eq.(2.11)) of a gaussian shaped local oscillator with a single photon pulse reshaped according to Eq.(7.1). Note that in all these plots the variations of the η_{tot} value are only due to variations in the mode-matching contribution η_{mm}, so apart from a normalization factor, the symbols η_{tot} and η_{mm} represent the same quantity.

7.4.2 Modulated local oscillator

Classical pulses cross-correlation In order to recover high homodyne efficiency and verify the generation of highly nonclassical zero-area SP wave packets, one has to measure them in the right mode. This is done by shaping the spectrotemporal profile of the reference LO by means of the pulse shaper (see Fig.7.8) properly programmed to mimic the effect of Eq.(7.1). A preliminary tuning of the LO shape is performed, for each cell temperature, by maximizing the fringe visibility at zero delay between the shaped LO and the classical zero-area pulses.

Single-photon homodyne detection These shaper settings then serve as the starting point for LO mode optimization in the homodyne setup to detect the shaped single photons (Fig.7.9). The different measurement scenarios are pictorially illustrated in Fig.7.10, with the different levels of matching between the (shaded) LO shape and the modulated single-photon wave packet.

The blue data points in Fig.7.10 correspond to the peak efficiencies obtained with properly shaped LO modes. A matched LO is clearly seen to detect the modulated single photons with a much higher global efficiency. The known homodyne detection efficiencies (the quantum efficiency of the photodiodes $\eta_{ph} = 98\%$ and electronic noise $\eta_{el} = 86\%$) and the residual optical losses $\eta_{op} = 93\%$, see Eq.(2.14), are then taken into account for maximum-likelihood (see Appendix B) reconstruction of the density matrix of the states in the mode defined by the LO, using a Fock-state basis up to $n = 2$. Clearly negative Wigner functions are obtained [see Fig.7.10(a)] for all the SP states measured with the properly shaped LO.

7.4.3 Pulse shaping

The mode-matching efficiency η_{mm} has been defined in Eq.(2.11) as the overlap between the normalized mode of the local oscillator $\tilde{\alpha}(\omega)$ and that of the

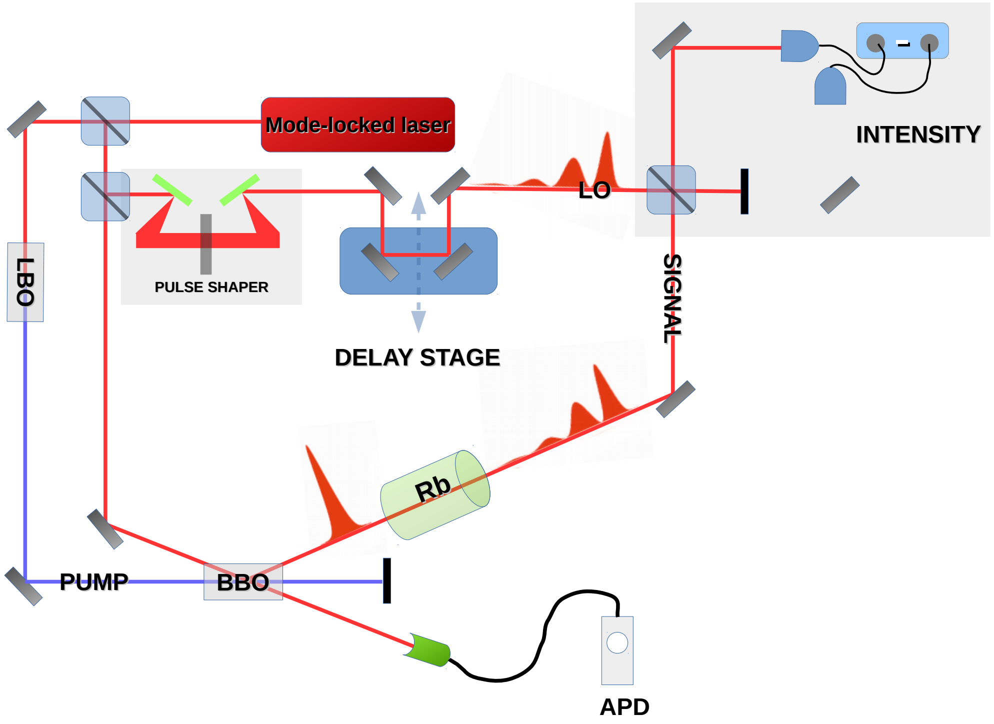

Figure 7.8: Experimental scheme used to tune the pulse shaper parameters, by means of a maximization of the classical pulse interference fringe visibility. Basically, it is the same setup of Fig.7.3 with the pulse shaper inserted along the local oscillator path.

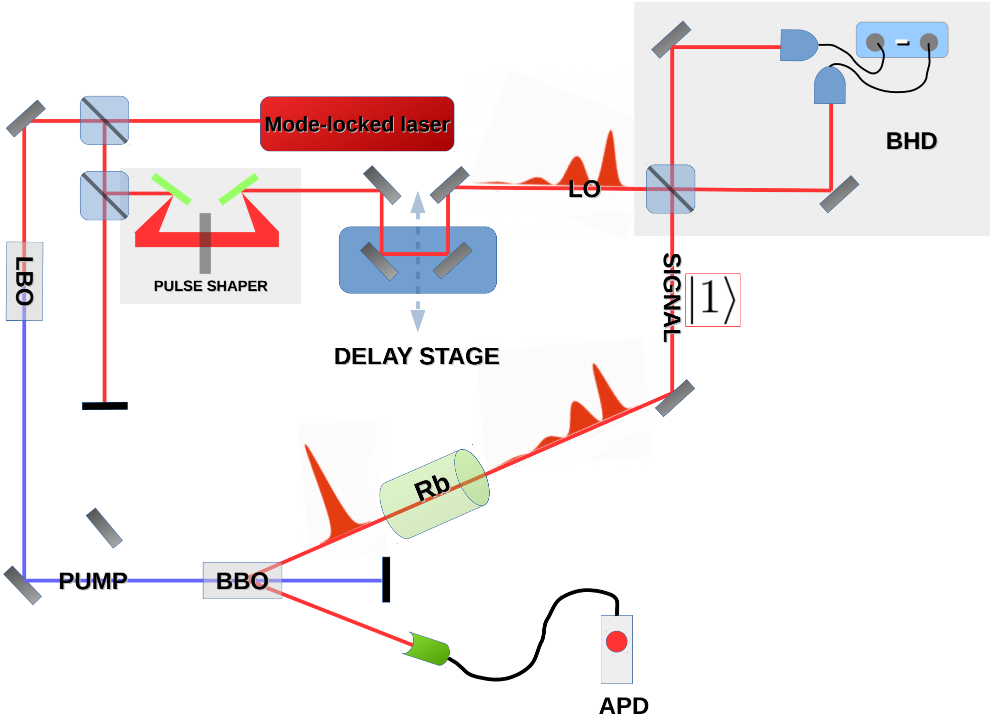

Figure 7.9: Experimental scheme used to prove the single photon 0π interaction. The local oscillator is shaped by using the same parameter found by the maximization of the classical visibility (scheme of Fig.7.8).

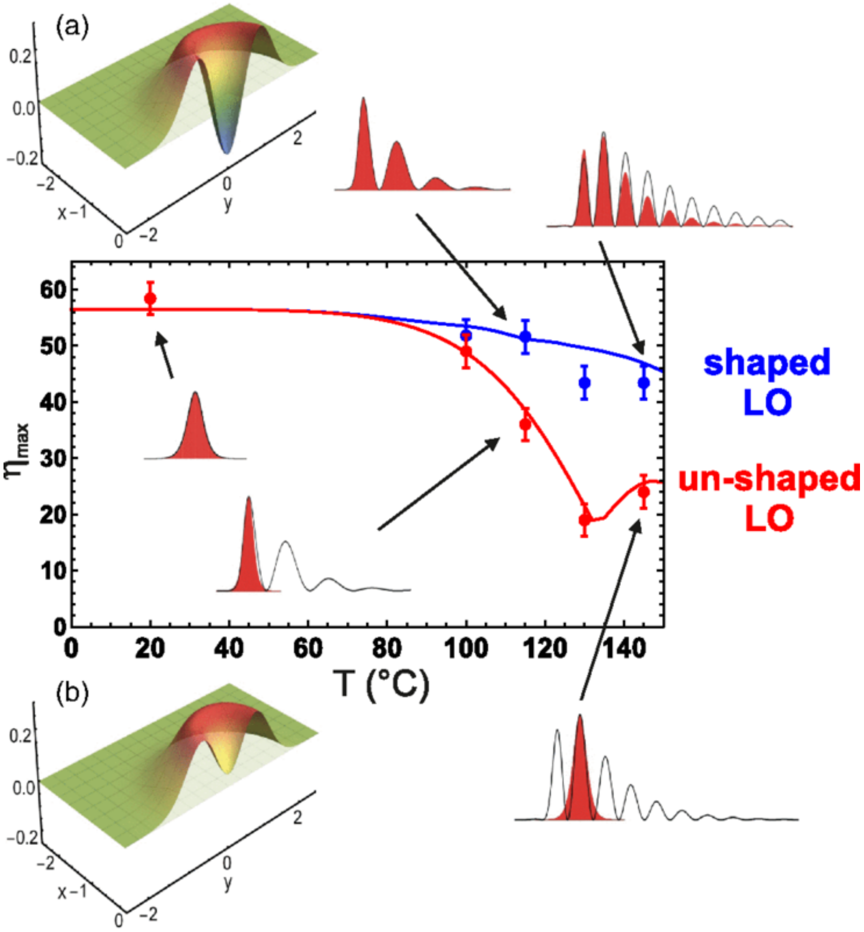

Figure 7.10: Experimental data and theoretical calculations for the maximum homodyne efficiency in the detection of distorted single-photon wave packets. Red points, experimental data for detection with unmodulated LO; blue points, experimental data with optimally shaped LO; red and blue solid curves, expected maximum homodyne efficiency in the two cases (including the effect of limited spectral resolution in the LO shaper). Red points and red curve are the same already shown in Fig.7.7. (a) and (b) show the reconstructed Wigner functions of the states, corrected for a detection efficiency of 78.5% ($= \eta_{op}\, \eta_{el}\, \eta_{ph}$, see Eq.(2.14)), as measured in the LO mode for the two cases at 115°C, with and without LO shaping, respectively.

target state, in this case a single photon, $\beta(\omega)$. Since homodyne detection requires a good mode matching, a faithful single photon quadrature distribution can be measured only in case that the two profiles $\tilde{\alpha}(\omega)$ and $\beta(\omega)$ are sufficiently similar. This condition forces to reshape the local oscillator temporal profile in the same way experienced by the single photon through the atomic vapour. To do this, we made use of a liquid-crystal-based pulse shaper, in which the refractive index of different spectral components can be modulated by means of the application of an external voltage. By properly controlling this voltage, the liquid-crystal mask can absorb and induce a dispersion over the spectrum $\tilde{\alpha}(\omega)$ of the local oscillator. In our experiment the mask has been programmed according to Eq.(7.1), in order to produce an effect similar to that produced by the hot atomic ensemble affecting the single-photon profile.

7.4.4 Atoms vs Pulse Shaper

The residual decreasing trend of the measured SP fraction for increasing temperature is mostly due to the limited spectral resolution of the LO pulse shaping system. Indeed, the current combination of gratings, lenses, and liquid-crystal modulators leads to a minimum spectral resolution $\Delta\lambda$ of about 0.6 nm, which bounds the range of temporal modulations that it can achieve to $\approx 1/\Delta\nu = \lambda^2/c\Delta\lambda = 10^{-12}$ s, that is a few picoseconds. When the high atomic optical depth causes the single photons to significantly spread over longer delays, the shaped LO mode β cannot perfectly overlap any more and the resulting homodyne efficiency decreases. By taking the effect of limited spectral resolution of our shaping system into account while calculating the maximum expected homodyne efficiency, we obtain the solid blue curve of Fig.7.10, which reproduces quite well the observed decrease with temperature. The parameters T and γ of Eq.(7.1) used to simulate the effect of the pulse shaper at different temperatures of the curve have been calculated respectively as the Doppler width (T) and by fitting the optical density values (γ) used to maximize the efficiency at the temperatures of the experiment $100°, 130°, 145°, 115°$C. The possible distortion of the SP wave front due to turbulence close to the hot cell surfaces is probably responsible for the additional degradation observed in the experimental data points at the highest temperatures.

7.4.5 Conclusion

In conclusion, we have demonstrated the reshaping of the spectrotemporal mode of ultrashort single-photon pulses while propagating through dense resonant atomic vapours. While the single-quantum character of the broadband light states is preserved due to negligible absorption by the narrow atomic transition, the temporal shape of the photon wave packet is deeply modified, assuming a characteristic zero-area modulated profile, never observed before for nonclassical light pulses.

The phenomenon of zero-area classical pulse formation is generally connected to successive interfering cycles of absorptions and stimulated emissions of the pulsed incident radiation by the resonant atomic ensemble [74]. Its observation at the single-photon level implies an intriguing change of perspective and has interesting links to the phenomenon of single-photon superradiance [92] and to new possibilities for the storage of quantum information. Our experiment is just the first step in a new direction that, by allowing one to directly follow the time evolution of the quantum light state, may deepen our understanding of the light-atom interaction at unexplored time scales.

Ringraziamenti

In conclusione di questa tesi, culmine degli sforzi di tre anni, vorrei ringraziare alcune persone il cui contributo è stato fondamentale nello svolgimento di questo lavoro. Sicuramente ad Alessandro e Marco, costantemente presenti sia dal punto di vista professionale che umano, va la mia sincera riconoscenza. Un pensiero va inoltre ad Antonio, Daniele, Giovanni, Milrian, Nicola e Valeria, con alcuni dei quali ho stretto nel tempo uno schietto rapporto molto poco professionale.

Appendix A

Homodyne operator

In this appendix I present explicit calculations relative to the balanced homodyne detection. All the symbols are referred to the notation already introduced and used in Chapter 2 and Section 3.2.6.

Homodyne operator (see eq.2.2)

$$\begin{aligned}
\hat{\mathcal{H}} &= \langle \alpha_{LO_2} | \hat{I}_{1'} - \hat{I}_{2'} | \alpha_{LO_2} \rangle \\
&= \int_T dt \langle \alpha_{LO_2} | \left[\hat{I}_{1'}(t) - \hat{I}_{2'}(t) \right] | \alpha_{LO_2} \rangle \\
&= \int_T dt \, \langle \alpha_{LO_2} | \left[\hat{a}^\dagger_{1'}(t) \hat{a}_{1'}(t) - \hat{a}^\dagger_{2'}(t) \hat{a}_{2'}(t) \right] | \alpha_{LO_2} \rangle \\
&= i \int dt \langle \alpha_{LO_2} | \left[\hat{a}^\dagger_{1}(t) \hat{a}_{2}(t) - \hat{a}^\dagger_{2}(t) \hat{a}_{1}(t) \right] | \alpha_{LO_2} \rangle \\
&= i \int dt \left[\hat{a}^\dagger_{1}(t) \alpha_{2}(t) - \hat{a}_{1}(t) \alpha^*_{2}(t) \right] \\
&= \int dt \left[\hat{a}^\dagger_{1}(t) \alpha_{2}(t) e^{i\pi/2} + \hat{a}_{1}(t) \alpha^*_{2}(t) e^{-i\pi/2} \right] \\
&= \hat{a}^\dagger_\alpha + \hat{a}_\alpha \\
&= 2 \, \hat{X}_\alpha \, (0) \\
&= 2 \sqrt{n_{LO}} \, \hat{X}_{\tilde{\alpha}} \, (0) \qquad \text{(A.1)}
\end{aligned}$$

Where the phase factor $e^{i\pi/2}$ has been absorbed into the mode α.

Losses (see eq.2.6)

$$\begin{aligned}
\hat{\mathcal{H}}(\theta,\alpha,\eta) &= \langle \alpha_{LO_2}, 0_{2'}, 0_{2''}|\hat{I}_{4'} - \hat{I}_{4''}|\alpha_{LO_2}, 0_{2'}, 0_{2''}\rangle \\
&= \int_T dt \langle \alpha_{LO_2}, 0_{2'}, 0_{2''}| \left[\hat{I}_{4'}(t) - \hat{I}_{4''}(t)\right] |\alpha_{LO_2}, 0_{2'}, 0_{2''}\rangle \\
&= \int_T dt\ \langle \alpha_{LO_2}, 0_{2'}, 0_{2''}| \left[\hat{a}^{\dagger}_{4'}(t)\hat{a}_{4'}(t) - \hat{a}^{\dagger}_{4''}(t)\hat{a}_{4''}(t)\right] |\alpha_{LO_2}, 0_{2'}, 0_{2''}\rangle \\
&= \int_T dt\ \langle \alpha_{LO_2}, 0_{2'}, 0_{2''}| \cdot \\
&\cdot \ \left(\sqrt{\eta_{ph}}\hat{a}^{\dagger}_{4}(t) - i\sqrt{1-\eta_{ph}}\hat{a}^{\dagger}_{2'}(t)\right)\left(\sqrt{\eta_{ph}}\hat{a}_{4}(t) + i\sqrt{1-\eta_{ph}}\hat{a}_{2'}(t)\right) - \\
&- \ \left(\sqrt{\eta_{ph}}\hat{a}^{\dagger}_{3}(t) - i\sqrt{1-\eta_{ph}}\hat{a}^{\dagger}_{2''}(t)\right)\left(\sqrt{\eta_{ph}}\hat{a}_{3}(t) + i\sqrt{1-\eta_{ph}}\hat{a}_{2''}(t)\right) \cdot \\
&\cdot \ |\alpha_{LO_2}, 0_{2'}, 0_{2''}\rangle \\
&= \eta_{ph} \int_T dt\ \langle \alpha_{LO_2}, 0_{2'}, 0_{2''}|\ \hat{a}^{\dagger}_{4}(t)\hat{a}_{4}(t) - \hat{a}^{\dagger}_{3}(t)\hat{a}_{3}(t)|\alpha_{LO_2}, 0_{2'}, 0_{2''}\rangle \\
&= \eta_{ph} \cdot \hat{\mathcal{H}}(\theta,\alpha) \qquad \text{(A.2)}
\end{aligned}$$

Mode matching (see eq.2.8)

$$
\begin{aligned}
\left(\Delta\hat{\mathcal{H}}(\eta)\right)^2 &= \langle\Psi_1,\alpha_{LO_2},0_{2'},0_{2''}|\left[\hat{I}_{4'}-\hat{I}_{4''}\right]^2|\Psi_1,\alpha_{LO_2},0_{2'},0_{2''}\rangle - \\
&- \langle\Psi_1,\alpha_{LO_2},0_{2'},0_{2''}|\hat{I}_{4'}-\hat{I}_{4''}|\Psi_1,\alpha_{LO_2},0_{2'},0_{2''}\rangle^2 \\
&= \iint_T dt_1\,dt_2\,\langle\,\hat{a}^\dagger_{4'}(t_1)\hat{a}_{4'}(t_1)\hat{a}^\dagger_{4'}(t_2)\hat{a}_{4'}(t_2) - \\
&- \hat{a}^\dagger_{4'}(t_1)\hat{a}^\dagger_{4'}(t_1)\hat{a}^\dagger_{4''}(t_2)\hat{a}^\dagger_{4''}(t_2) - \hat{a}^\dagger_{4''}(t_1)\hat{a}^\dagger_{4''}(t_1)\hat{a}^\dagger_{4'}(t_2)\hat{a}^\dagger_{4'}(t_2) + \\
&+ \hat{a}^\dagger_{4''}(t_1)\hat{a}^\dagger_{4''}(t_1)\hat{a}^\dagger_{4''}(t_2)\hat{a}^\dagger_{4''}(t_2)\,\rangle - \\
&- \eta_{ph}^2\int_T dt\,\langle\,\hat{a}^\dagger_{1'}(t)\hat{a}_{1'}(t)-\hat{a}^\dagger_{1''}(t)\hat{a}_{1''}(t)\rangle^2 \\
&= \eta_{ph}^2\iint_T dt_1\,dt_2\langle\hat{a}^\dagger_{1'}(t_1)\hat{a}_{1'}(t_1)\left[\hat{a}^\dagger_{1'}(t_2)\hat{a}^\dagger_{1'}(t_2)-\hat{a}^\dagger_{1''}(t_2)\hat{a}^\dagger_{1''}(t_2)\right] \\
&- \hat{a}^\dagger_{1''}(t_1)\hat{a}_{1''}(t_1)\left[\hat{a}^\dagger_{1'}(t_2)\hat{a}^\dagger_{1'}(t_2)-\hat{a}^\dagger_{1''}(t_2)\hat{a}^\dagger_{1''}(t_2)\right]\rangle + \\
&+ \eta_{ph}(1-\eta_{ph})\iint_T dt_1\,dt_2\,\cdot \\
&\cdot \langle\hat{a}^\dagger_{1'}(t_1)\hat{a}_{2'}(t_1)\hat{a}^\dagger_{2'}(t_2)\hat{a}_{1'}(t_2)+\hat{a}^\dagger_{1''}(t_1)\hat{a}_{2''}(t_1)\hat{a}^\dagger_{2''}(t_2)\hat{a}_{1''}(t_2)\,\rangle - \\
&- \eta_{ph}^2\int_T dt\,\langle\,\hat{a}^\dagger_{1'}(t)\hat{a}_{1'}(t)-\hat{a}^\dagger_{1''}(t)\hat{a}_{1''}(t)\rangle^2 \\
&= \eta_{ph}^2\,\langle\left[\int_T dt\,\hat{a}^\dagger_{1'}(t)\hat{a}_{1'}(t)-\hat{a}^\dagger_{1''}(t)\hat{a}_{1''}(t)\right]^2\rangle - \\
&- \eta_{ph}^2\,\langle\,\int_T dt\,\hat{a}^\dagger_{1'}(t)\hat{a}_{1'}(t)-\hat{a}^\dagger_{1''}(t)\hat{a}_{1''}(t)\,\rangle^2 \\
&+ \eta_{ph}(1-\eta_{ph})\iint_T dt_1\,dt_2\,\delta(t_1-t_2)\,\langle\,\left[\hat{a}^\dagger_{1'}(t_1)\hat{a}_{1'}(t_2)+\hat{a}^\dagger_{1''}(t_1)\hat{a}_{1''}(t_2)\right]\rangle \\
&= \eta_{ph}^2\left\{\langle\left[\int_T dt\,\alpha(t)\hat{a}^\dagger_1(t)+\alpha^*(t)\hat{a}_1(t)\right]^2\rangle - \langle\int_T dt\,\alpha(t)\hat{a}^\dagger_1(t)+\alpha^*(t)\hat{a}_1(t)\,\rangle^2\right\} \\
&+ \eta_{ph}(1-\eta_{ph})\int_T dt\,\langle\left[\hat{a}^\dagger_1(t)\hat{a}_1(t)+\hat{a}^\dagger_2(t)\hat{a}_2(t)\right]\rangle \\
&= \eta_{ph}^2\left\{\langle\left[\hat{a}^\dagger_\alpha+\hat{a}_\alpha\right]^2\rangle - \langle\,\left[\hat{a}^\dagger_\alpha+\hat{a}_\alpha\right]\,\rangle^2\right\} \\
&+ \eta_{ph}(1-\eta_{ph})\int_T dt\,\langle\left[\hat{a}^\dagger_1(t)\hat{a}_1(t)+|\alpha(t)|^2\right]\rangle \\
&= 4\eta_{ph}^2\,\left(\Delta\hat{X}_\alpha(\theta)\right)^2+\eta_{ph}(1-\eta_{ph})\left(\int_T dt\,\langle\,\hat{n}_1(t)\rangle+n_{LO}\right),
\end{aligned}
\tag{A.3}
$$

Single photon efficiency (see eq.2.9)

$$\begin{aligned}
&= \eta_{ph}^2 \left\{ \langle 1_\beta | \left[\hat{a}_\alpha^\dagger + \hat{a}_\alpha \right]^2 |1_\beta\rangle - \langle 1_\beta | \left[\hat{a}_\alpha^\dagger + \hat{a}_\alpha \right] |1_\beta\rangle^2 \right\} \\
&+ \eta_{ph}(1-\eta_{ph}) \left(\int_T dt \, \langle 1_\beta | \, \hat{n}_1(t) \, |1_\beta\rangle + n_{LO} \right) \\
&= \eta_{ph}^2 \langle 1_\beta | \left[\hat{a}_\alpha^\dagger \hat{a}_\alpha + \hat{a}_\alpha \hat{a}_\alpha^\dagger \right] |1_\beta\rangle + \eta_{ph}(1-\eta_{ph}) \; (1+n_{LO}) \\
&= \eta_{ph}^2 \langle 1_\beta | \left[2 \, \hat{a}_\alpha^\dagger \hat{a}_\alpha + n_{LO} \right] |1_\beta\rangle + \eta(1-\eta) \; (1+n_{LO}) \\
&= 2\eta_{ph}^2 \int dt \, dt_1 \, dt_2 \, dt' \; \beta^*(t)\beta(t')\alpha(t_1)\alpha^*(t_2) \; \langle 1_t | \hat{a}^\dagger(t_1)\hat{a}(t_2) | 1_{t'} \rangle + \\
&+ \eta_{ph}^2 \, n_{LO} + \eta_{ph}(1-\eta_{ph}) \; (1+n_{LO}) \\
&= 2\eta_{ph}^2 \int dt \, dt_1 \, dt_2 \, dt' \; \beta^*(t)\beta(t')\alpha(t_1)\alpha^*(t_2) \; \delta(t-t_1) \, \delta(t_2-t') + \\
&+ \eta_{ph}^2 \, n_{LO} + \eta_{ph}(1-\eta_{ph}) \; (1+n_{LO}) \\
&= 2\eta_{ph}^2 \left| \int dt \, \beta^*(t) \, \alpha(t) \right|^2 + \eta_{ph}^2 \, n_{LO} + \eta_{ph}(1-\eta_{ph}) \; (1+n_{LO})
\end{aligned} \tag{A.4}$$

Visibility and mode-matching efficiency (see eq.3.53)

$$\begin{aligned}
V(\gamma,\alpha) &= \frac{\int dt \, \langle M | \hat{a}_{1'}^\dagger(t) \hat{a}_{1'}(t) \, |M\rangle - \langle m | \int dt \, \hat{a}_{1'}^\dagger(t) \hat{a}_{1'}(t) \, |m\rangle}{\int dt \, \langle M | \hat{a}_{1'}^\dagger(t) \hat{a}_{1'}(t) \, |M\rangle + \langle m | \int dt \, \hat{a}_{1'}^\dagger(t) \hat{a}_{1'}(t) \, |m\rangle} \\
&= \frac{i \left[\int dt \, \gamma^*(t)\alpha(t) - \gamma(t)\alpha^*(t) - \gamma^*(t) e^{-i\pi} \alpha(t) + \gamma(t) e^{i\pi} \alpha^*(t) \right]}{2 \left[\int dt \, |\gamma(t)|^2 + \int dt \, |\alpha(t)|^2 \right]} \\
&= \frac{i \left[\int dt \, \gamma^*(t)\alpha(t) - \gamma(t)\alpha^*(t) \right]}{\left[\int dt \, |\gamma(t)|^2 + \int dt \, |\alpha(t)|^2 \right]} \\
&= \frac{\left[\int dt \, \gamma^*(t)\alpha(t) e^{i\pi/2} + \gamma(t)\alpha^*(t) e^{-i\pi/2} \right]}{\left[\int dt \, |\gamma(t)|^2 + \int dt \, |\alpha(t)|^2 \right]} \\
&= \mathcal{R} \left\{ \frac{2 \int dt \, \gamma^*(t)\alpha(t)}{\left[\int dt \, |\gamma(t)|^2 + \int dt \, |\alpha(t)|^2 \right]} \right\}
\end{aligned} \tag{A.5}$$

Appendix B

Quantum state characterization

In any state and mode engineering experiment the final stage is always represented by a complete characterization of the manipulated state. Indeed we previously observed that important physical informations can be embedded in any systems by means of appropriate operations, so in the final stage it will be necessary extract them to get the proper conclusions. An effective method to accomplish it should permit to characterize the system as fully as possible and prevent in principle any possible ignorance. Such a complete information deduction is what is commonly called *state tomography*.

Whatever is its experimental implementation, all *state tomography* processes share two common stages. The first one consists in the acquisition of a series of measurements of observables properly selected to characterize completely the system. This selection must be carefully made because not all the possible measurements provide a complete picture of the system. For instance, the position probability distribution $P(x)$ alone is not sufficient to represent the state $|\Psi(x)|e^{i\phi(x)}$, since lacking in any phase information. A set of observables sufficient to characterize completely the system is instead called *quorum*. It is clear that in selecting the *quorum*, a fundamental role will be played by the continuous or discrete variable nature of the target state description. In this work the *quorum* will be always given by series of quadrature measurements $\hat{X}\left(\theta\right)$, each one performed with *balanced homodyne detection* for a set of values of the phase θ.

Once the *quorum* is achieved, it is necessary to somehow invert the relation

$$x = Tr\left\{\rho\hat{X}\left(\theta\right)\right\}, \tag{B.1}$$

to get as much information as possible about the density matrix ρ from the observed values x. The solution methods proposed and used during these years, often called *reconstruction algorithms*, have been based on different approaches to the problem. The first one is called *inverse Radon transformation* [65], and is based on the idea of inverting the quadrature probability distribution

$$Pr\left(x\left(\theta\right),\theta\right)=\int_{-\infty}^{+\infty}W(x,y)\,\delta\left(\,x\left(\theta\right)-x\cos\theta-y\sin\theta\,\right)\;dx, \tag{B.2}$$

marginal distribution of the Wigner function $W(x,y)$ with a mathematical tool based on the *Radon transformation* formalism to retrieve just the Wigner function

$$W(x,y)=\frac{2}{\pi}\int_{-\infty}^{+\infty}\langle x+k|\rho|x-k\rangle\;e^{i4yk}\;dk. \tag{B.3}$$

Actually it is necessary to introduce some ad hoc hypothesis to restrict the number of degrees of freedom and permit the application of this algorithm [64]. Moreover, the procedure works well only when the uncertainties in the observed quadrature distributions are negligible, that is in the limit of a very large number of data and very precise measurements. Otherwise, the errors can lead to inaccurate, even unphysical, features in the reconstructed state, like negative values on the diagonal elements of the density matrix ρ. However, in this work, a statistical inference method based on the maximization of the *likelihood function* has been followed.

B.0.1 Quantum state tomography

In this section we show the method used to reconstruct the density matrix ρ from the acquired quadrature measurements.

From electric field measurements to quantum state reconstruction: max likelihood algorithm A very popular principle of statistical inference largely used in physics is the socalled *likelihood maximization* algorithm. In mathematical statistics the *likelihood function* $\mathcal{L}$ represents the presumed probability of observing a given set of values $\{y_i\}$ as a consequence of a measurement on a system described by the density matrix ρ. The maximization

of $\mathcal{L}$ over the independent degrees of freedom $\rho_{m,n}$, that is over the density matrix elements, ensures a density matrix that predicts just the data set experimentally observed as the most probably measured.
In 2002 Z. Hradil et al. [66] demonstrated with variational methods that the maximum value of the likelihood can be found by solving the non linear system

$$\hat{R}(\rho, \boldsymbol{y})\rho = \rho, \tag{B.4}$$

with

$$\hat{R}(\rho, \boldsymbol{y}) = \sum_{i'} f_{i'} \frac{|y_i'\rangle\langle y_i'|}{\langle y_i'|\rho|y_i'\rangle} \tag{B.5}$$

and f_i given by the frequency of the observed value y_i. Basically the system (B.4) can be iteratively solved according to the equation

$$\hat{R}(\rho^{(n)}, \boldsymbol{y})\rho^{(n)} = \rho^{(n+1)}, \tag{B.6}$$

with the initial condition

$$\rho^{(0)} = \mathcal{N}\left\{I\right\}. \tag{B.7}$$

Unfortunately eq.(B.6) can lead in some special cases to non positive density matrices, then in 2004 Hradil et al. [67],[68] proposed a slightly different and unphysical-results-free equation like

$$\hat{R}(\rho^{(n)}, \boldsymbol{y})\rho^{(n)}\hat{R}(\rho^{(n)}, \boldsymbol{y}) = \rho^{(n+1)}. \tag{B.8}$$

Currently this improved version is the most used algorithm to experimentally reconstruct the density matrix from measurements.
In this thesis the data set $\{y_i\}$ is always represented by different series of quadrature measurements each one performed with the homodyne detector for a fixed value of the phase θ_j defined by the local oscillator, so

$$\begin{aligned} \{y_i\} &= \{x_i\left(\theta_j\right), \theta_j\} && \text{(B.9)} \\ |y_i\rangle\langle y_i| &= |x_i\left(\theta_j\right), \theta_j\rangle\langle x_i\left(\theta_j\right), \theta_j|. && \text{(B.10)} \end{aligned}$$

max likelihood algorithm implementation To implement the abstract algorithm of eq.(B.8) it is necessary to project it on a properly chosen basis and give a specific form to the operator $\hat{R}\left(\rho^{(n)}, \boldsymbol{y}\right)$ and to the density matrix ρ. In this thesis we have always chosen the Fock representation, and then

$$\begin{aligned}
\rho^{(n+1)}_{m,n} &= \langle m|\hat{R}(\rho^{(n)}, \boldsymbol{y})\rho^{(n)}\hat{R}(\rho^{(n)}, \boldsymbol{y})|n\rangle \\
&= \sum_{k,l}\langle m|\hat{R}(\rho^{(n)}, \boldsymbol{y})|k\rangle\rho^{(n)}_{k,l}\ \langle l|\hat{R}(\rho^{(n)}, \boldsymbol{y})|n\rangle \\
&= \sum_{k,l}\hat{R}_{m,k}(\rho^{(n)}, \boldsymbol{y})\rho^{(n)}_{k,l}\ \hat{R}_{l,n}(\rho^{(n)}, \boldsymbol{y}) \qquad \text{(B.11)}
\end{aligned}$$

with $\hat{R}_{m,k}(\rho^{(n)}, \boldsymbol{y})$, matrix element at the nth iteration, given by

$$\begin{aligned}
\hat{R}_{m,k}(\rho^{(n)}, \boldsymbol{y}) &= \langle m|\hat{R}(\rho^{(n)}, \boldsymbol{y})|k\rangle \\
&= \sum_{i,j} f_{i,j}\frac{\langle m|x_i\left(\theta_j\right), \theta_j\rangle\langle x_i\left(\theta_j\right), \theta_j|k\rangle}{\langle x_i\left(\theta_j\right), \theta_j|\rho^{(n)}|x_i\left(\theta_j\right), \theta_j\rangle} \\
&= \sum_{i,j} f_{i,j}\frac{\langle m|x_i\left(\theta_j\right), \theta_j\rangle\langle x_i\left(\theta_j\right), \theta_j|k\rangle}{Pr^{(n)}\left(x_i\left(\theta_j\right), \theta_j\right)}, \qquad \text{(B.12)}
\end{aligned}$$

and the nth iteration probability

$$\begin{aligned}
Pr^{(n)}\left(x_i\left(\theta_j\right), \theta_j\right) &= \langle x_i\left(\theta_j\right), \theta_j|\rho|x_i\left(\theta_j\right), \theta_j\rangle \\
&= \sum_{t,s}\langle x_i\left(\theta_j\right), \theta_j|t\rangle\rho^{(n)}_{t,s}\langle s|x_i\left(\theta_j\right), \theta_j\rangle. \qquad \text{(B.13)}
\end{aligned}$$

We can observe that the probability $Pr^{(n)}\left(x_i\left(\theta_j\right), \theta_j\right)$ doesn't depend on m and k so its value is the same for all the elements $\hat{R}_{m,k}(\rho^{(n)}, \boldsymbol{y})$ and can then be calculated only once for each iteration.
The projection of the quadrature eigenstates on the number states $\langle n|x_i\left(\theta_j\right), \theta_j\rangle$ recurs many times in the calculation and is equal to

$$\begin{aligned}
\langle n|x\left(\theta\right), \theta\rangle &= \langle 0|\frac{\hat{a}^n}{\sqrt{n!}}\hat{U}^{\dagger}_{\theta}|x\left(0\right), 0\rangle \\
&= e^{in\theta}\left(\frac{2}{\pi}\right)^{\frac{1}{4}}\frac{H_n\left[\sqrt{2}x\right]}{\sqrt{2^n}n!}e^{-x^2} \qquad \text{(B.14)}
\end{aligned}$$

with $H_n[x]$ denoting the Hermite polynomials.

It is important to observe that in collecting the quadrature data set, the continuous photocurrents values must be converted into the digital numbers $\{x_i(\theta_j), \theta_j\}$. To minimize such a unavoidable conversion error, a narrow binning is used such that basically a quadrature value never repeats and thus the frequencies $f_{i,j}$ can assume only the values 0 or 1.

Actually the maximum likelihood implementation involves a necessary hypothesis still not mentioned. Indeed, the computation of the numerical series in eqs.(B.11), (B.12), (B.13) requires the truncation to a finite number of terms. This means that a proper assumption to limit the Fock space must be introduced. Hradil et al. in [69] overcame this problem by suggesting an objective method based on the eigenvalues of a proper operator $\hat{G}$, allowing the truncation of the Fock space without the necessity of further hypothesis. Anyway, in all the experiments described in this thesis, the Fock space has been limited *a priori* by exploiting the preliminary approximate knowledge of the investigated states and limiting the Fock space to the expected non null density matrix elements.

Losses A good advantage of the max lik technique is the possibility to incorporate directly into the reconstruction procedure the effects of the detection inefficiencies. We have already introduced the beam splitter model for the losses in photodiodes (see appendix A), so now it is only necessary to reconsider the ingredients of the algorithm as transformed by an η transmissivity beam splitter. In eqs.(B.11), (B.12), (B.13) we must then introduce the transformations [65], [68]

$$\rho \rightarrow \rho_\eta, \tag{B.15}$$

$$|x(\theta), \theta\rangle\langle x(\theta), \theta| \rightarrow |x(\theta), \theta, \eta\rangle\langle x(\theta), \theta, \eta| \tag{B.16}$$

with

$$\langle m|\rho_\eta|n\rangle = \sum_{k\geq 0} B_{m+k,m}(\eta)\ B_{n+k,n}(\eta)\ \langle m+k|\,\rho\,|n+k\rangle \tag{B.17}$$

$$\begin{aligned} |x_i(\theta_j),\theta_j,\eta\rangle\langle x_i(\theta_j),\theta_j,\eta| &= \sum_{m,n,k} B_{m+k,m}(\eta)\ B_{n+k,n}(\eta)\cdot \\ &\cdot\ \langle n|x_i(\theta_j),\theta_j\rangle\langle x_i(\theta_j),\theta_j|m\rangle\cdot \\ &\cdot\ |n+k\rangle\langle m+k| \end{aligned} \tag{B.18}$$

where $B_{n+k,n} = \sqrt{\binom{n+k}{k}\eta^n\eta^k}$ are the Bernoulli coefficients representing the effect of the loss beam splitter. Note that into the reconstruction stage only a correction for non-perfect detection efficiency η_{det} is allowed. This adjustment enables the reconstruction of what has been really experimentally generated without considering the deterioration due to a non-perfect observation. Thus, a correction for the generation efficiency η_{gen} is senseless.

B.0.2 Quantum state fidelity

Once the density matrix ρ_1 describing the measured system has been reconstructed, it is often useful to compare this experimental result with the ρ_2 expected from theoretical predictions. To quantify their likeness we can introduce a fidelity for mixed states as [70]

$$\mathcal{F}(\rho_1,\rho_2) = \left[Tr\left\{\sqrt{\sqrt{\rho_1}\cdot\rho_2\cdot\sqrt{\rho_1}}\right\}\right]^2. \tag{B.19}$$

Appendix C

Birefringence

Both the photon subtraction and addition operations considered in this work, have been implemented by exploiting the well known phenomenon of birefringence, so it can be useful to spend a few words on it. Indeed we have seen how birefringence enables the use of half-wave-plates to implement $\hat{a}$ and fulfil phase matching conditions necessary for the parametric down conversion nonlinear interaction at the basis of the experimental $\hat{a}^\dagger$ realization.
A material is said birefringent when it shows different optical properties respect to differently polarized light, in particular when the refractive index is depending on the directions of polarization and propagation of the light beam, as a consequence of a natural or induced anisotropy. We will focus on a particular type of birefringent crystal, said uniaxial, in which the refractive index takes different values if taken along the direction defined by a particular crystal axis or in its perpendicular plane. This particular axis is referred to as the extraordinary axis[1]. An electric field experiences a refractive index $n_e(\beta)$, said extraordinary (e), if lying in the plane defined by this direction and the direction of the wave propagation $\boldsymbol{k}$, while if oscillating in the orthogonal plane it feels a refractive index n_o, called ordinary (o). The extraordinary refractive index $n_e(\beta)$ depends on the angle β defined by the wave vector $\boldsymbol{k}$ and the extraordinary direction according to this equation:

$$\frac{1}{n_e^2(\beta)} = \frac{\sin^2(\beta)}{\bar{n}_e^2} + \frac{\cos^2(\beta)}{n_o^2}. \tag{C.1}$$

where $\bar{n}_e^2$ is the refractive index experienced by a purely extraordinary

---

[1] The extraordinary axis is sometimes called also optical axis.

polarization.
This has strong consequences for the beam propagation, and the e and o polarization components of a randomly polarized beam spatially separate when travelling inside the crystal. Indeed the electric displacement field $\boldsymbol{D}_e$ and the electric field $\boldsymbol{E}$ of the e polarization are no more parallel due to the anisotropy of the material and the wavector $\boldsymbol{k}_e$, orthogonal to $\boldsymbol{D}_e$, is deviated respect to the ordinary beam direction of propagation $\boldsymbol{k}_o$[2]. This phenomenon, called *spatial walkoff*, prevents to use beams waists too small within the crystal to avoid complete complete geometrical separations of the outgoing beams.

---

[2] Consider the linear approximation

$$\boldsymbol{P}_e = \chi^{(1)} \boldsymbol{E}_e \tag{C.2}$$

where χ is a 3×3 matrix

$$\chi = \begin{pmatrix} \chi_{11} & \chi_{12} & \chi_{13} \\ \chi_{21} & \chi_{22} & \chi_{23} \\ \chi_{31} & \chi_{32} & \chi_{33} \end{pmatrix}. \tag{C.3}$$

The electric displacement field $\boldsymbol{D}_e$ can be written as

$$\begin{aligned} \boldsymbol{D}_e &= \epsilon_0 \boldsymbol{E}_e + \boldsymbol{P}_e \\ &= \epsilon_0 \boldsymbol{E}_e + \epsilon_0 \chi \boldsymbol{E}_e \\ &= \epsilon_0 (1 + \chi) \boldsymbol{E}_e. \end{aligned} \tag{C.4}$$

Then for the extraordinary ray, in an anisotropic material, $\boldsymbol{D}_e$ is no more parallel to $\boldsymbol{E}_e$. For the ordinary component the suscettivity is diagonal and $\boldsymbol{D}_o$ is still parallel to $\boldsymbol{E}_o$.

Bibliography

[1] R. Blatt, G. J. Milburn and A. Lvovksy , J. Phys. B: At. Mol. Opt. Phys. 46, 100201 (2013) .

[2] V. Parigi, A. Zavatta, M. S. Kim and M. Bellini, Science 317, 1890 (2007).

[3] A. Zavatta, V. Parigi, M. S. Kim and M. Bellini, New Journal of Physics 10, 123006 (2008).

[4] Y. Kurochkin, A. S. Prasad, and A. I. Lvovsky, Phys. Rev. Lett. 112, 070402 (2014).

[5] E. Lombardi, F. Sciarrino, S. Popescu, and F. De Martini, Phys. Rev. Lett. 88, 070402 (2002).

[6] U. L. Andersen, J. S. Neergaard-Nielsen, P. van Loock and A. Furusawa, Nature Physics 11(9), 713-719 (2015).

[7] A. Zavatta, S. Viciani and M. Bellini, Science 306, 660 (2004).

[8] E. Knill, R. Laflamme and G. J. Milburn, Nature 409, 46-52 (2001).

[9] J. L. OBrien, G. J. Pryde, A. G. White, T. C. Ralph and D. Branning, Nature 426, 264-267 (2003).

[10] A. I. Lvovsky, H. Hansen, T. Aichele, O. Benson, J. Mlynek and S. Schiller, Phys. Rev. Lett. 87, 050402 (2001).

[11] M. R. Vanner, M. Aspelmayer, M. S. Kim, Phys. Rev. Lett. 110, 010504 (2013).

[12] V. Buek, M. Hillery, and R. F. Werner, Phys. Rev. A 60, R2626(R) (1999).

[13] F. De Martini, V. Buek F. Sciarrino and C. Sias, Nature 419, 815-818 (2002).

[14] T. C. Ralph, N. K. Langford, T. B. Bell, and A. G. White, Phys. Rev. A 65, 062324 (2002).

[15] M. Jezek, M. Micuda, I. Straka, M. Mikova, M. Dusek, and J. Fiurasek, Phys. Rev. A 89, 042316 (2014).

[16] E. P. Wigner, Group Theory and its applications to the quantum mechanics of the atomic spectra, Academic Press, New York (1959).

[17] E. Bimbard, N. Jain, A. MacRae and A. I. Lvovsky, Nature Photonics 4, 243 - 247 (2010).

[18] A. Zavatta, S. Viciani, and M. Bellini, Phys. Rev. A 72, 023820 (2005).

[19] N. Gisin, Nature 419, 797-798 (2002).

[20] G. S. Agarwal and K. Tara, Phys. Rev. A 43, 492 (1991).

[21] A. Zavatta, M. Bellini, P.L. Ramazza, F. Marin, F.T. Arecchi, J. Opt. Sci. Am. B 19, 1189-1194 (2002).

[22] L. Allen and J. H. Eberly, Optical Resonance and two-level atoms, John Wiley & Sons, Inc. (1975).

[23] A. I. Lvovsky and S. A. Babichev, Phys. Rev. A 66, 011801 (2002).

[24] C. K. Hong and L. Mandel, Phys. Rev. Lett. 56, 58 (1986).

[25] J. J. Sakurai, Modern quantum mechanics, Addison-Wesley, New York, 1994.

[26] Z. Y. Ou, Quantum Semiclass. Opt. 9 (1997).

[27] T. Aichele, A. I. Lvovsky and S. Schiller, Eur. Phys. J. D 18, 237-245 (2002).

[28] Z. Y. Ou, L. J. Wang, and L. Mandel, Phys. Rev. A 40, 1428 (1989).

[29] P. J. Mosley, J. S. Lundeen, B. J. Smith and I. A. Walmsley, New Journal of Physics 10, 9 (2008)

[30] P. J. Mosley, J. S. Lundeen, B. J. Smith, P. Wasylczyk, A. B. URen, C. Silberhorn and I. A. Walmsley, Phys. Rev. Lett. 100, 133601 (2008)

[31] K. Wakui, H. Takahashi, A. Furusawa, M. Sasaki, Optics Express 15, 6, 3568 (2007).

[32] S. M. H. Rafsanjani, M. Mirhosseini, O. S. Magana-Loaiza, B. T. Gard, R. Birrittella, B. E. Koltenbah, C. G. Parazzoli, B. A. Capron, C. C. Gerry, J. P. Dowling and R. W. Boyd, https://arxiv.org/abs/1605.05424v1 (2016).

[33] A. Ourjoumtsev, R. Tualle-Brouri, J. Laurat, P. Grangier, Science 312, 83-86 (2006).

[34] M. D. Vidrighin, O. Dahlsten, M. Barbieri, M. S. Kim, V. Vedral and I. A. Walmsley, Phys. Rev. Lett. 116, 050401 (2016).

[35] S. R. Huisman, N. Jain, S. A. Babichev, F. Vewinger, N. Zhang, S. H. Youn and A. I. Lvovsky, Optics Letter Vol. 34, 27392741 (2009).

[36] M. Cooper, L. J. Wright, C. Soller and Brian J. Smith, Optics Express 21, 5309-5317 (2013).

[37] A. Zavatta, V. Parigi and M. Bellini, Physical Review A 78, 033809 (2008).

[38] R. Krischek, W. Wieczorek, A. Ozawa, N. Kiesel, P. Michelberger, T. Udem and H. Weinfurter, Nature Photonics 4, 170-173 (2010).

[39] J.A. Wheeler and W.H. Zurek, eds., Princeton university Press, New Jersey 1983.

[40] A. J. Leggett and Anupam Garg, Phys. Rev. Lett. 54, 857 (1985).

[41] A. Zavatta, V. Parigi, M. S. Kim, H. Jeong and M. Bellini, Physical Review Letters 103, 140406 (2009).

[42] M. S. Kim, H. Jeong, A. Zavatta, V. Parigi and M. Bellini, Physical Review Letters 101, 260401 (2008).

[43] W. H. Zurek, Physics Today October 1991, 44:36-44 (1991).

[44] M. Yukawa, K. Miyata, T. Mizuta, H. Yonezawa, P. Marek, R. Filip and Akira Furusawa, Optics Express 21, 5529-5535 (2013).

[45] R. Loudon, Oxford University Press, USA (2000).

[46] A. I. Lvovsky, B. C. Sanders and W. tittel, Nature Photonics 3, 706-714 (2009).

[47] T. B. Pittman, B. C. Jacobs and J. D. Franson, Phys. Rev. A 66, 042303 (2002).

[48] P. M. Leung and T. C. Ralph, Phys. Rev. A 74, 022311 (2006).

[49] Sh. Petrosyan and Yu. Malakyan, Physical Review A 88, 063817 (2013).

[50] S.L. McCallg and E. L. Hahnf, Physical Review Letters 18, 908 (1967).

[51] G. L. Lamb Jr., Review of Modern Physics 43, 99 (1971).

[52] Brian McNeil, Nature Photonics 9, 207 (2015).

[53] F. T. Arecchi and R. Bonifacio, IEEE Journal of Quantum Electronics, QE-1, 169 (1965).

[54] M. D. Crisp, Physical Review A 1, 1604 (1970).

[55] P. Mandel and M. Tlidi, Introduction to soliton theory, Lecture notes prepared for the Spring school Solitons in Optical Cavities, May 8-13, 2006 held in Cargese(Corsica), France, `http://socaff.inln.cnrs.fr/IMG/pdf/introduction_to_soliton_theory.pdf`.

[56] C. Polycarpou, K. N. Cassemiro, G. Venturi, A. Zavatta and M. Bellini, Physical Review Letters. 109, 053602 (2012).

[57] Don Monroe, Physics 5, 86 (2012).

[58] research highlights, Nature Photonics 6 (2012).

[59] A. A. Berni, T. Gehring, B. M. Nielsen, V. Hndchen, M. G. A. Paris and U. L. Andersen, Nature Photonics 9, 577 (2015).

[60] J. Roslund, R. Medeiros de Araujo, S. Jiang, C. Fabre and N. Treps, Nature Photonics 8, 109 (2014).

[61] R. Medeiros de Araujo, J. Roslund, Y. Cai, G. Ferrini, C. Fabre, and N. Treps, Physical Review A 89, 053828 (2014).

[62] C. Gerry, P. Knight, Introductory Quantum Optics, Cambridge University Press.

[63] R. Loudon, The Quantum Theory of Light, Oxford University Press.

[64] A. I. Lvovsky and M. G. Raymer, Reviews of Modern Physics 81, 299 (2009).

[65] U. Leonhardt, Measuring the quantum state of light, Cambridge University Press.

[66] Z. Hradil, R. Myska, J. Summhammer, H. Rauch, Physics Letters A 261, 20-24 (1999).

[67] Z. Hradil, J.Rehacek, J. Fiurasek, M. Jezek, Maximum-Likelihood Methods in Quantum Mechanics, Lect. Notes Phys. 649, 59112, Springer-Verlag Berlin Heidelberg (2004).

[68] A. I. Lvovsky, Journal of Optics B: Quantum Semiclass. Opt. 6, 556559 (2004).

[69] Z. Hradil, D. Mogilevtsev and J. Rehacek, Physical Review Letters 96, 230401 (2006).

[70] R. Jozsa, Journal of Modern Optics, 41, 2315-2323 (1994).

[71] G. S. He, Nonlinear optics and photonics, Oxford University Press.

[72] M. S. Kim, H. Jeong, A. Zavatta, V. Parigi, and M. Bellini, Physical Review Letters 101, 260401 (2008).

[73] M. F. Pusey, J. Barrett and T. Rudolph, Nature Physics 8, 475478 (2012).

[74] N. Dudovich, D. Oron, and Y. Silberberg, Physical Review Letters 88, 123004 (2002).

[75] Sh. Petrosyan and Yu. Malakyan, Physical Review A 88, 063817 (2013).

[76] X.-H. Bao, Y. Qian, J. Yang, H. Zhang, Z.-B. Chen, T. Yang and J.-W. Pan, Physical Review Letters 101, 190501 (2008).

[77] M. Scholz, L. Koch and O. Benson, Physical Review Letters 102, 063603 (2009).

[78] F. Wolfgramm, Y.A. de Icaza Astiz, F.A. Beduini, A. Cer and M.W. Mitchell, Physical Review Letters 106, 053602 (2011).

[79] H. Zhang et al., Nature Photonics 5, 628 (2011).

[80] J.K. Thompson, J. Simon, H. Loh, and V. Vuleti, Science 313, 74 (2006).

[81] M. Lettner, M. Mcke, S. Riedl, C. Vo, C. Hahn, S. Baur, J. Bochmann, S. Ritter, S. Drr and G. Rempe, Physical Review Letters 106, 210503 (2011).

[82] T. Chanelire, D.N. Matsukevich, S.D. Jenkins, S.-Y. Lan, T.A.B. Kennedy and A. Kuzmich, Nature (London) 438, 833 (2005).

[83] K.S. Choi, H. Deng, J. Laurat and H.J. Kimble, Nature (London) 452, 67 (2008).

[84] M.D. Eisaman, A. Andr, F. Massou, M. Fleischhauer, A.S. Zibrov and M.D. Lukin, Nature (London) 438, 837 (2005).

[85] A. MacRae, T. Brannan, R. Achal, and A.I. Lvovsky, Physical Review Letters 109, 033601 (2012).

[86] T. Chanelire, D.N. Matsukevich, S.D. Jenkins, S.-Y. Lan, T.A.B. Kennedy and A. Kuzmich, Nature (London) 438, 833 (2005).

[83] K.S. Choi, H. Deng, J. Laurat and H.J. Kimble, Nature (London) 452, 67 (2008).

[84] J.E. Rothenberg, D. Grischkowsky and A.C. Balant, Physical Review Letters 53, 552 (1984).

[85] M. Matusovsky, B. Vaynberg and M. Rosenbluh, J. Opt. Soc. Am. B 13, 1994 (1996).

[86] U. Kallmann, S. Brattke, and W. Hartmann, Physical Review A 59, 814 (1999).

[87] D. Felinto, L.H. Acioli and S.S. Vianna, Optics. Letters. 25, 917 (2000).

[88] A.M. Weiner, Optics Communications 284, 3669 (2011).

[89] H.J. Carmichael, G.T. Foster, L.A. Orozco, J.E. Reiner and P.R. Rice, Progress in Optics, edited by E. Wolf (Elsevier, Amsterdam, 2004), Vol. 46, pp. 355403.

[90] H.J. Carmichael, H.M. Castro-Beltran, G.T. Foster, and L.A. Orozco, , Physical Review Letters 85, 1855 (2000).

[91] G.T. Foster, L.A. Orozco, H.M. Castro-Beltran, and H.J. Carmichael, Physical Review Letters 85, 3149 (2000).

[92] M.O. Scully, E.S. Fry, C.H. Raymond Ooi, and K. Wdkiewic, Physical Review Letters 96, 010501 (2006).

[93] T. Peyronel, et al., Nature 488, 57-60 (2012).

[94] V. Venkatamaran, K. Saha, and A. L. Gaeta, Nature Photonics 7, 138-141 (2013).

[95] T. C. Ralph, I. Sollner, S. Mahmoodian, A. G. White, and P. Lodahl, Physical Review Letters 114, 173603 (2015).

[96] B. Yurke and D. Stoler, Physical Review Letters 57, 13 (1986).

[97] G.J. Milburn, Physical Review Letters 62, 2124 (1989).

[98] D. Vitali, M. Fortunato, and P. Tombesi, Physical Review Letters 85, 445 (2000).

[99] M.G.A. Paris, M.B. Plenio, S. Bose, D. Jonathan, and G.M. DAriano, Physical Letters A 273, 153 (2000).